5-2018

Optical Diagnostic Techniques as an Approach to Characterizing Forced and Freestream Disturbances

Adam Joel Harris
University of Tennessee

To the Graduate Council:

I am submitting herewith a thesis written by Adam Joel Harris entitled "Optical Diagnostic Techniques as an Approach to Characterizing Forced and Freestream Disturbances." I have examined the final electronic copy of this thesis for form and content and recommend that it be accepted in partial fulfillment of the requirements for the degree of Master of Science, with a major in Aerospace Engineering.

John D. Schmisseur, Major Professor

We have read this thesis and recommend its acceptance:

James G. Coder, Trevor M. Moeller, Zhili Zhang

Accepted for the Council:
Dixie L. Thompson

Vice Provost and Dean of the Graduate School

(Original signatures are on file with official student records.)

Optical Diagnostic Techniques as an Approach to Characterizing Forced and Freestream Disturbances

A Thesis Presented for the
Master of Science
Degree
The University of Tennessee, Knoxville

Adam Joel Harris
May 2018

ACKNOWLEDGEMENTS

I would first like to first acknowledge my sponsors at the Air Force Office of Scientific Research (AFOSR) for funding this research under award number FA9550-17-1-0085, without which, this work would not have been possible. I would also like to thank my advisor, Dr. John Schmisseur for guiding me through this process, and providing support in a myriad of ways throughout graduate school, you have been a great mentor. I thank Dr. Phil Kreth and Dr. Chris Combs for teaching me the skills in the lab that I needed to accomplish this, your guidance and patience are invaluable. I'd also like to thank my committee members, Dr. Trevor Moeller, Dr. James Coder, and Dr. Zhili Zhang for their contributions. Lastly, I'd like to thank my brother, Scott Harris for always believing in me, and supporting me over the years.

ABSTRACT

Two optical techniques are examined for their feasibility to measure laser-induced disturbances and freestream disturbances in supersonic flow. The two techniques examined are laser differential interferometry and time-resolved Schlieren. They provide unique capabilities for measuring these disturbances, and may provide much insight when used simultaneously. Laser differential interferometry can measure broadband noise in a wind tunnel in the < 100kHz range. Focusing laser differential interferometry may be a more appropriate technique to measure laser-induced disturbances, as it can spatially filter regions of little interest. Laser differential interferometry is path-integrated, and measurements can be obscured by dynamic content present in the regions of little interest along the measurement volume; however, it was used to make mean measurements of laser-induced disturbances.

Schlieren can make qualitative observations of freestream disturbance levels for a global field of view. Schlieren allows observation of many characteristics of a laser-induced disturbance such as the growth rate and internal spatial frequencies in quiescent air. It was determined that the growth rate of laser-induced disturbances is highly non-linear, of the form $D(t) = a(t)^b$ where t is time in seconds and D is diameter in meters. Mean values of a = 0.0271 and b = 0.171 are observed. Spatial frequencies of the thermal disturbance are typically found to vary between 7 and 15 cm^{-1}. Turbulent structures are found to evolve within the first 500 us, and diffusion causes the disturbance to continue to expand for the next 10 ms where the disturbances would typically become too diffuse to observe.

Internal spatial frequencies are found to be proportional to the diameter of the disturbance by normalizing spectra by the instantaneous diameter. This shows that after the evolution of turbulent structures, diffusion of the forced disturbance becomes the dominant mechanism in the absence of a driving force. The disturbance behaves very similarly in a Mach 2 flow as it does in quiescent air, though the mean diameter is observed to be larger by a ratio of 1.71. This is likely due to the lower density environment.

TABLE OF CONTENTS

LIST OF TABLES

LIST OF FIGURES

CHAPTER ONE
INTRODUCTION

Ground testing facilities such as wind tunnels provide an environment to thoroughly study flow phenomena through diagnostics that could not be used in a flight environment. While wind tunnels can create environments that are similar to flight conditions, they cannot create a test environment that identically mimics flight conditions. This is due to the presence of boundary layers along wind tunnel walls that generate noise environments that elevate the levels of freestream fluctuations.[1] These freestream fluctuations present in a ground testing facility result in an environment that inherently differs from flight conditions.

The presence of these fluctuations, often called disturbances, have been identified since Kovasnay first investigated wind tunnel flow quality in the 1950's.[2] Such disturbances can be broadly grouped into three main categories: vortical, or velocity fluctuations, entropic, or temperature fluctuations, and acoustic, or pressure fluctuations, as shown in Figure 1. These three modes of fluctuations are often considered to be independent of each other, and the overall disturbance levels in a facility can be thought of as a linear combination of these three modes. Velocity and temperature fluctuations tend to originate from the conditions in, or upstream of the stilling chamber and propagate throughout the tunnel along streamlines. Pressure fluctuations, however, can originate from many sources even within the test section itself. One particular type of pressure

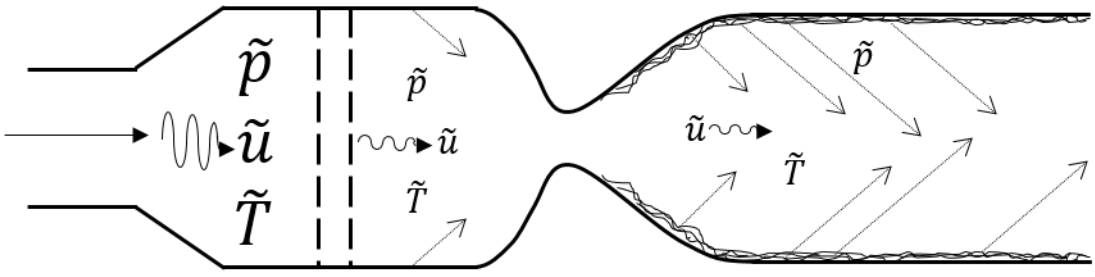

Figure 1-Schematic of sources and types of freestream disturbances $\tilde{p}$ = pressure fluctuations, $\tilde{u}$ = velocity fluctuations, $\tilde{T}$ = temperature fluctuations. Adapted from Pate et al. 1980.

disturbance, acoustic radiation, emanates from turbulent structures in the boundary layer of a supersonic flow, and exceed the magnitude of other disturbances by orders of magnitude.[3] These disturbances have the potential to affect the results of experiments conducted in a given facility. It is thereby important to have a holistic understanding of the disturbance levels present in test facilities.

1.1 Motivation

As described above, disturbances in a ground testing facility fall into one of three broad categories: velocity, temperature, and pressure, or acoustic disturbances.[2] These disturbances exist and propagate independently of each other, where the overall disturbance level can be thought of as a linear combination of the three independent modes. It has been observed in previous studies that the magnitude of these modes of fluctuations can vary in relation to each other.[4] Furthermore, acoustic disturbances tend to dominate other modes of fluctuations in flows with a Mach number greater than 2.5,[3] making such a characterization of these disturbances of particular importance to hypersonic research interests.

In a flow field where the freestream disturbance level is dominated by an acoustic disturbance field, the characteristics of flow over a test model can be drastically altered. Such disturbances can affect boundary layer transition, or even cause early transition to occur.[5-7] This poses a significant problem to researchers interested in studying boundary layer transition or boundary layer interactions, as the noise field present in the facility may have an adverse effect on the state of the boundary layer. Furthermore, this may hinder the comparison of flight data to test data, as these acoustic disturbances are present in a flight environment at lower magnitudes than those in a wind tunnel.[3] As such, there is significant value in developing a holistic characterization of the acoustic disturbances present in a given facility, especially if one intends to study phenomena such as boundary layer transition, instability mechanisms, shockwave-boundary layer inter actions, or receptivity.

In recent years, a large emphasis has been placed on the development and construction of quiet wind tunnels. Quiet facilities are typically defined as facilities where the root-mean-square pitot pressure is less than 0.1% of the mean pressure.[8] As such, these

facilities are characterized as having drastically reduced levels of freestream pressure fluctuations; however, the flow may not be completely disturbance-free. Quiet wind tunnels are tremendously complex and expensive to construct, maintain, and operate.[9] In addition, so-called "noisy" conventional wind tunnels greatly outnumber their quiet counterparts.[9] In this manner, quiet wind tunnels should not be viewed as a solution to the acoustic disturbance problem, but rather a more quality test environment that still requires a thorough characterization of the disturbance levels.

Previous literature that exists on acoustic disturbance characterization has typically relied on intrusive, low bandwidth instruments such as hotwires, unsteady pressure transducers, or microphones, all of which may not necessarily respond to the high frequency content associated with acoustic disturbances.[10] In hypersonic flows, such acoustic fluctuations may have content well beyond this range, though without significant data on the topic, a realistic estimation of the high frequency content can be difficult to establish. As researchers continue to study high Mach number flows, the value of such characterization becomes increasingly important. In addition, computational fluid dynamics (CFD) simulations of high Mach number flows need a larger database of acoustic radiation characterization to validate models that now predict such phenomena.[11,12]

With recent advancements in optical diagnostic techniques, non-intrusive optical measurements with acquisition rates in excess of 1 MHz have been demonstrated, which is well beyond the capabilities of conventional, intrusive instrument systems.[13-15] Based on this technological development, an examination of the feasibility of non-intrusive diagnostics to make highly-resolved measurements of acoustic disturbances is warranted. This study examines the virtues of using optical diagnostics to extend the existing database on acoustic disturbances into higher frequency ranges that have been beyond the range of available measurement systems to date.

In the process of developing optical methods of characterizing acoustic radiation independently of the other disturbances, a milestone objective has been established in order to validate and verify this optical capability, as characterizing acoustic radiation is a particularly challenging task. Prior to studying naturally occurring acoustic radiation, a precursor study intended to characterize laser-induced perturbations has been carried out.

Such a characterization is of great value to the community, as many fields such as receptivity, combustion, and Laser-Induced Breakdown Spectroscopy (LIBS) make use of a laser-induced perturbation. Previous characterizations of laser-induced disturbances rely on mean measurements and intrusive techniques that limit an understanding of the internal structure and evolution of the turbulent length scales of such a disturbance.[16] Herein, an optical method of characterizing this disturbance is also warranted, as many of the problems that prohibit acoustic disturbance characterization also prohibit laser-induced disturbance characterization. In this sense, an optical characterization of laser-induced perturbations makes a logical milestone objective in the overall goal of developing a robust optical method of studying acoustic radiation, as the forced perturbation will behave similarly in many ways to a turbulent structure in the boundary layer, but at a larger amplitude.

1.2 Objectives

Recent advancements in optical diagnostic techniques have presented a unique opportunity to examine such techniques' feasibility for making acoustic radiation measurements, and measurements of a forced perturbation, as literature suggests that such techniques can measure frequency content as high as 1 MHz[13-15] at a fraction of the cost in previous years. This would extend the existing database on acoustic radiation into higher frequency ranges that have been previously unexplored up to this point, while also providing the additional benefit of performing a characterization that does not require the use of intrusive instrumentation systems. Furthermore, a characterization of forced perturbations would reveal the characteristic length scales associated with the disturbance, as well as the characteristics of the evolution of turbulence, as previous methods have been prohibitively restricted by mean measurement techniques, and intrusive diagnostics.

This study develops and characterizes two diagnostics systems that have been identified as candidates for such measurements. Following which, the instrumentation systems are used to attempt to measure acoustic radiation and a forced perturbation and compare the results to other similar measurements made with intrusive instrumentation systems. The techniques that are examined are laser differential interferometry (LDI), and

time-resolved Schlieren. Furthermore, this study aims to answer the following questions in detail:

1. Can LDI and time-resolved Schlieren be used an effective tool for studying acoustic radiation in ground test facilities?
2. What are the limitations associated with these instrument systems?
3. What are the characteristic length scales and spatial frequencies of the turbulence associated with a forced perturbation, and how do they evolve with time?

CHAPTER TWO
LITERATURE REVIEW

This study explores optical methods of characterizing two types of disturbances commonly encountered in fluid dynamics. First, laser-induced breakdown is increasingly used as a controlled perturbation in experiments. Second, acoustic radiation, which is a disturbance that has been shown to contaminate the testing environment in a wind tunnel. This section provides a brief summary of the prior research that has been published on these two types of disturbances, as well as the instrumentation techniques that are used to characterize them.

2.1 Acoustic Radiation

Ground testing facilities are typically affected by the presence of elevated freestream disturbance levels due to the very nature and construction of the facilities themselves. Walls that duct the flow in the nozzle and test section have turbulent boundary layers with turbulent structures that shear as they interact with flow near the wall. This radiates acoustic disturbances into the freestream of the flow. These disturbances are fluctuations in the flow that result in elevated turbulence levels, and may influence testing conditions by driving early transition on a test model boundary layer. Such freestream disturbances can be broadly characterized into three main modes; temperature fluctuations, velocity fluctuations, and pressure fluctuations, also called acoustic fluctuations. Temperature fluctuations and velocity fluctuations have been observed to originate upstream of the nozzle, and propagate along streamlines throughout the test section of the wind tunnel.[4] Through the proper use of screens and stilling chambers, it has been shown that the magnitude of these disturbances can be minimized.[2]

Morkovin[4] showed that acoustic fluctuations fundamentally differ from velocity and temperature fluctuations in this aspect as acoustic radiation, one particular mode of acoustic fluctuation, has been shown to originate in the turbulent boundary layers present on the walls of a ground testing facility.[10] This implies that stilling chambers and screens my not be an effective tool in reducing the magnitudes of acoustic disturbances to acceptable levels, as the disturbances may originate from within the test section itself.

Figure 2 shows acoustic rays present in the Mach 2 tunnel at the University of Tennessee Space institute as an example of what this phenomena looks like in situ.[17]

A qualitative understanding of acoustic radiation and its source has existed for some time, and is described well in the literature.[10] In the shear layer of a supersonic boundary layer, eddies convect downstream and form a pattern that can act as a virtual wall with respect to the higher velocity fluid near the edge of the boundary layer. As flow shears over this virtual wall, it generates noise that radiates into the freestream of the supersonic flow (hence the name acoustic *radiation*).[18] While an individual occurrence of this phenomena may be trivial, this process continues to occur so long as there is a turbulent boundary layer. This results in what is often referred to as an acoustic radiation "field" in the freestream, comprised of a distribution of individual acoustic rays.

Previous studies have characterized acoustic radiation using techniques such as pitot probes, hotwires, or microphones, which are intrusive, and are typically associated

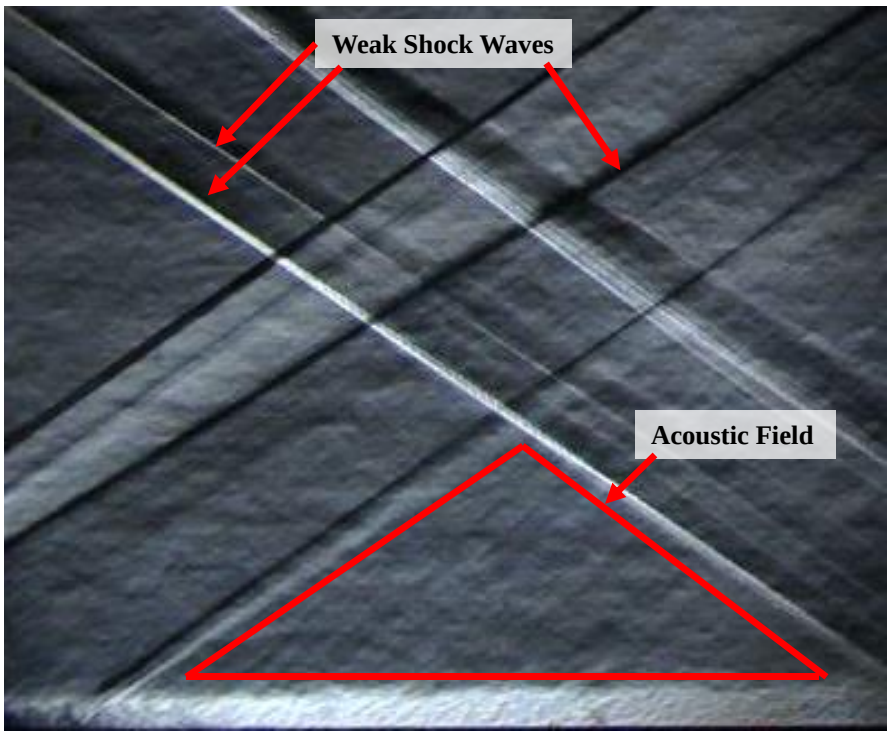

Figure 2- A Schlieren image taken in the Mach 2 wind tunnel at UTSI disambiguating weak shock waves from an acoustic field.

with relatively low bandwidths. Despite these challenges, much has been learned about acoustic radiation. A number of researchers have previously demonstrated that the magnitude of fluctuations in flow properties associated with acoustic radiation is a function of Mach number,[19] boundary layer scale,[20] test section scale,[21] and Reynolds number.[22] It has also been observed that the bandwidth of acoustic fluctuation frequencies has been shown to increase with Reynolds number.[22]

In a study by Kistler and Chen,[23] a correlation between wind tunnel wall-pressure fluctuations and freestream-pressure fluctuations was established. Later, Ffowcs Williams[24] established a theoretical model that predicts freestream pressure fluctuations, $\tilde{p}$, as a function of wall pressure fluctuations, $\tilde{p}_w$, and Mach number, M, expressed as,

$$\frac{\tilde{p}}{\tau_w} = \frac{\tilde{p}_w}{\tau_w}\left\{\frac{5\varepsilon}{24\pi^2}\int_1^{M\infty}\frac{(M^2-1)^{1/2}dM}{M^m\{1+0.2M^2\}^2}\right\}^{1/2} \quad (1)$$

where τ_w is the shear stress at the wall, and ε, π, and m are constants. This model was found to agree with measurements performed by Laufer[21] and Kistler.[23] Furthermore, the magnitude of disturbances associated with the acoustic radiation field was found to be spatially uniform in magnitude.[20] The acoustic radiation was not dependent on the distance from the boundary layer, and it radiated equally from each wall of the test section[21] (i.e., the radiation from one wall was equal to one fourth of the magnitude of radiation from four walls). Furthermore, it has been discussed in previous literature that acoustic radiation will tend to dominate other modes of freestream disturbances at high Mach numbers[3] (typically at $M > 2.5$). Acoustic radiation has also been shown to influence boundary layer transition, causing a premature transition when compared to a flight environment.[5-7] This poses a significant challenge to researchers attempting to study boundary layer transition in a supersonic or hypersonic environment, as this disturbance will be present at non-trivial amplitudes and will influence the test.

2.2 Laser-Induced Perturbations

Laser-induced perturbations are a technique increasingly used in fluid dynamics; however, a critical understanding of the characteristics of such forced perturbations is still a topic of research.[16,25,26] Laser-induced perturbations, as the name implies, makes use of

a high energy, pulsed laser to create a disturbance in a fluid by focusing the laser such that it creates a local region of plasma. This local region of plasma returns to gaseous state on the nanosecond timescale, leaving a region of hot gas.[27] This hot gas is characterized by elevated temperatures, hence, it is often referred to as a "hot-spot." Due to the typical ellipsoid volume that the plasma is assumed to take, the thermal disturbance evolves into a toroidal shape.[25,26] This rapid expansion also results in a spherical pressure wave that propagates outward in all directions until it asymptotically approaches an acoustic wave.

Forced disturbances have been used in a variety of applications, especially in the field of boundary layer receptivity, instability and transition analysis.[28-31] Other applications include studying the characteristics of a forward facing cavity in a supersonic flow.[32,33] The more common applications are in the use of laser-induced breakdown spectroscopy (LIBS),[34-36] and various applications in combustion experiments and reacting flows experiments.[37,38]

While a forced perturbation is useful in aiding the study of other fluid dynamic scenarios, holistic models of these disturbances themselves are lacking in detail. Previous analysis of these forced perturbations have relied on mean measurements through use of techniques such as hotwire anemometry,[16] or unsteady pressure transducers, which only present a statistical average of the characteristics of these disturbances. Some work has made use of Schlieren[25,26,39-41] to study these forced perturbations to characterize how these disturbances evolve over time, but can be limited by experimental constraints, and such images are often difficult or otherwise hazardous to acquire. Such challenges have prohibited a more complete characterization of laser-induced disturbances in previous works.

The deficit of knowledge on the internal structure of these perturbations poses a problem to the community that aims to model such forced perturbations with computational fluid dynamics (CFD) tools. It has been noted in previous literature that validation data necessary for accurate simulations of these forced perturbations is lacking. Such validation data would dramatically improve the understanding of these disturbances and would allow more accurate modelling of these disturbances.[42]

2.3 Instrumentation Techniques

Several instrumentation techniques are used throughout this work, some of which are well established techniques, while others are not considered mainstream at the time of writing. This section discusses the underlying theory behind the different instrumentation systems as well as how these techniques have been used in previous studies.

2.3.1 Schlieren

Schlieren is a common flow visualization technique that relies on the principle of the Gladstone-Dale relation,[43] expressed as,

$$n = 1 + K\rho \tag{2}$$

where n is the index of refraction, K is the Gladstone-Dale constant, and ρ is density. Schlieren allows the imaging of density gradients in a fluid medium, providing qualitative, and more recently quantitative measurements of compressible fluid dynamics.[44] Collimated light is passed through the test medium, where it encounters density gradients. This causes the light to refract and deviate from its original optical path. After the collimated light passes through the test gas, it is focused down to a point, where a spatial filter is applied. This spatial filter can be adjusted so that light bent away from its original path is blocked, whereas light that was not is allowed to pass through onto the detector. This results in an image where the intensity of each pixel corresponds to the density gradient present.

2.3.2 Laser Differential Interferometry (LDI)

All interferometric techniques work on the basic principle of the Gladstone-Dale relation shown in Eq. (2). In general terms, the Gladstone-Dale relation shows that the index of refraction for a given medium is proportional to the density of the medium, and likewise, any fluctuation in the density of the medium will result in a fluctuation in its index of refraction. In this manner, any shift in density of the test gas will result in a shift in optical path length of a light wave passing through it.[45] For two light waves passing through differing density media, this will cause a relative phase angle shift, which will cause the two waves to interfere. This interference can be measured with a proper selection of optics

and a photodiode. The basic principles of laser differential interferometry (LDI) were best described by G. Smeets,[46,47] who is often credited with developing the technique.

An important precept of using LDI is that of phase ambiguity. If the interference of the two beams is allowed to exceed a half wavelength, then the actual phase angle shift between the two beams becomes ambiguous, as $\pi \times n$ radians of phase angle shift could occur for any measurement the system produces. For this reason, it is necessary to restrict the domain of interference, and previous literature has commonly restricted it to ±π/10 radians, as shown in Figure 3. This restricts the interference to the linear portion of the interference curve, resulting in a quantifiable relationship between the density gradient and the voltage measured on the photodetector, expressed as,

$$\frac{\Delta\rho}{\rho_L} = \frac{\lambda_0}{2\pi K L \rho_L} \sin\left(\frac{V}{V_0} - 1\right) \tag{3}$$

where the difference in density between beams is shown as $\Delta\rho$, ρ_L is the local density, λ_0 is the laser wavelength, K is the Gladstone-Dale constant, L is the distance between beams, V is the voltage on the photodiode, and V_0 is the voltage measured on the photodiode with complete constructive interference.

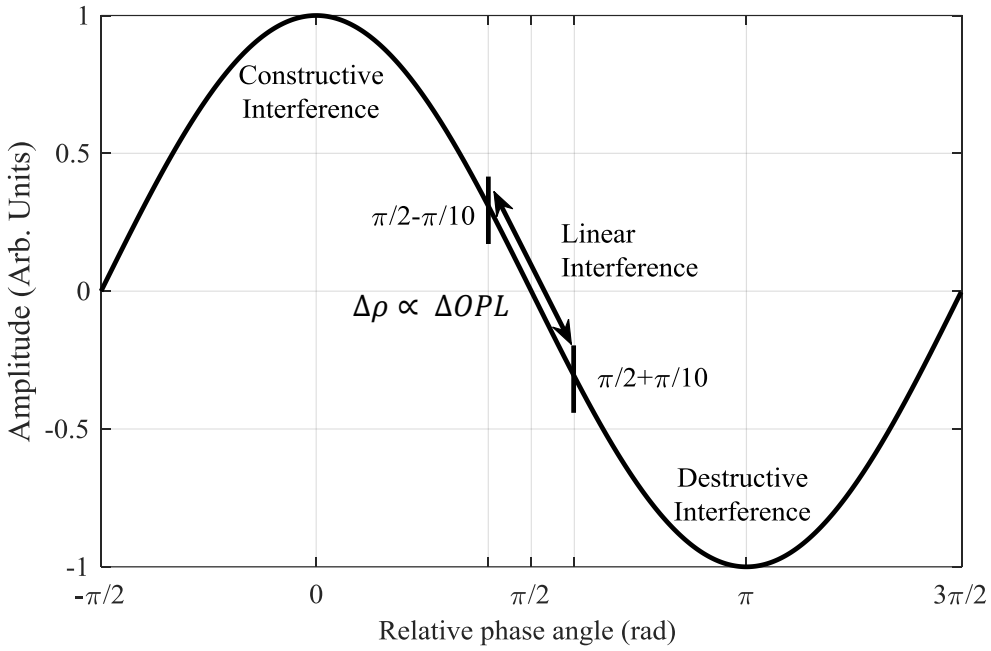

Figure 3- A plot of the interference resulting from two waves of equal magnitude.

A schematic of a typical LDI system is shown in Figure 4. A continuous wave laser (this work uses a He-Ne 632.8-nm laser) is first polarized at 45°, typically by means of a polarization filter or quarter wave plate. The laser is then passed through a focusing lens and beam-splitting prism that are placed one focal length apart. This work makes use of a Wollaston prism as it splits the beams along some finite angle, ε, and polarizes them mutually orthogonal to each other simultaneously. If the incoming laser light is properly polarized at 45°, this ensures that the bifurcated beams are polarized at 0° and 90°, respectively, and contain equal amounts of power. It is essential that the beams are at equal power, as this ensures that complete destructive interference will occur at a relative phase angle of π radians. Polarizing the beams to be mutually orthogonal also allows the beams retain their uniqueness while sharing a common beam path. The bifurcated beams are then passed through another collimating lens placed one focal length away from the Wollaston prism. This ensures that the beams are constant diameter and constant beam separation throughout the test region.

With these conditions satisfied, two parallel beams traverse the test gas, and when undisturbed, theoretically have the same optical path length and a relative phase angle shift of $\pi/2$ radians. As the beams encounter density gradients, one beam's optical path length will be shifted relative to the other, resulting in the interference described previously. It is important to note that a density gradient encountered anywhere along the beam pair's

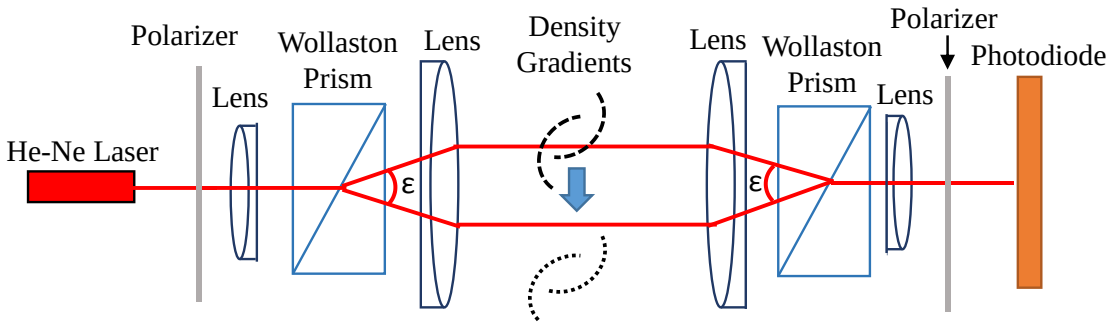

Figure 4- Schematic of a typical LDI system.

optical path length will contribute to the overall measurement that the system produces, making LDI a path-integrated technique. When the beams traverse the entirety of the test volume, they are then recombined using a symmetric set of optics to the set previously described. The recombined beam is then passed through another polarization filter placed at 45°. When filtered in such a manner any interference of the two beams will manifest itself as a change in intensity at a polarization of 45°. This change in intensity can be measured by a photodiode with sufficient bandwidth.

In theory, a system constructed in this manner has a temporal bandwidth that is dictated by the electronics used, and a spatial bandwidth that is dictated by the selection and quality of the optics. Previous works in the literature have reported bandwidths as high as 10 MHz,[15] and spatial resolutions as small as 120 μm.[13] This provides a distinct advantage over other intrusive instrument systems such as unsteady pressure transducers, hot-wires, and microphones, which are typically associated with relatively limited bandwidths and are intrusive in nature. Furthermore, by selecting appropriate optics, the system can be "tuned" by adjusting the beam spacing in order to maximize the signal-to-noise ratio at specific frequency ranges of interest, allowing a broad range of applications of LDI.

CHAPTER THREE
EXPERIMENTAL SETUP AND METHODOLOGY

This thesis presents work from multiple instrument systems in both a quiescent air environment as well as a supersonic wind tunnel. The following chapter describes the experimental setup used to produce the results presented in chapters 4, 5, and 6.

3.1 Mach 2 Wind Tunnel

The University of Tennessee Space Institute (UTSI) High Speed Wind Tunnel (HSWT), shown in Figure 5 is a Mach 2 blow-down type facility with a 0.203-m x 0.203-m (8-in x 8-in) test section, resulting in a 507 m/s freestream velocity[48]. The stagnation pressure used is 340 kPa, which results in a unit Reynolds number of approximately 31×10^6 per meter. Typical stagnation temperature is 285 K, and run times can vary from 10 s to 120 s at these conditions. The test section is comprised of three modular sections with interchangeable walls, floors and ceilings. BK7 glass windows provide optical access to the test section floor, boundary layer and freestream, enabling the use of Schlieren, LDI and other optical diagnostic techniques. This optical access facilitates the measurement of freestream disturbance levels and acoustic radiation present in the facility.

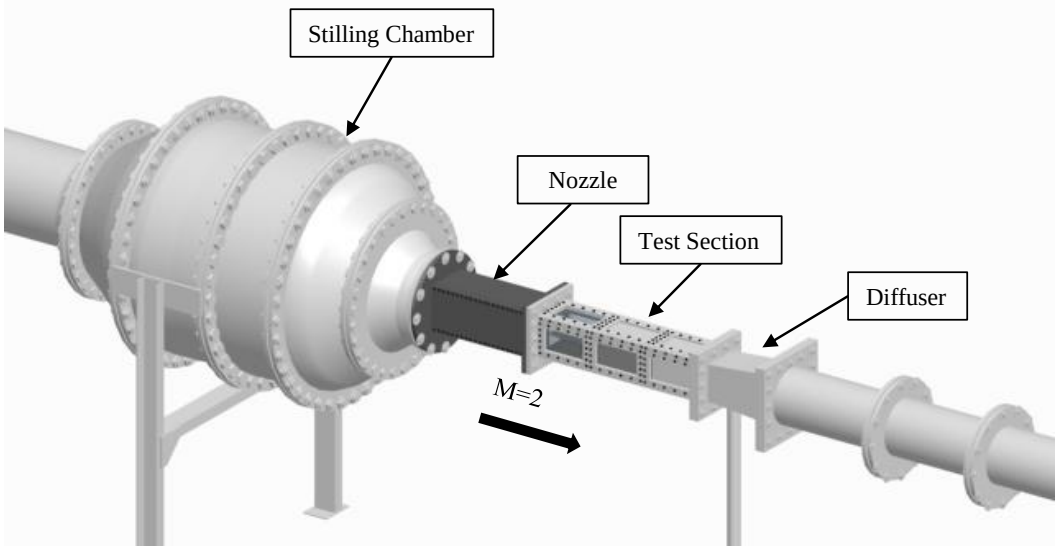

Figure 5- Schematic of the UTSI Mach 2 wind tunnel.

3.2 Laser Differential Interferometer

The laser differential interferometer used in this work was developed by the author at UTSI, based on other instruments reported in the literature.[13,14,28,45] The laser used is an Aerotek 632.8-nm continuous-wave Helium-Neon laser. The laser was measured to produce 30 mW of power, and the beam diameter was measured to be 1.2 mm. Three different configurations of optics are used throughout this work, the first is a configuration used to measure turbulence in a free jet, which will be referred to as the free jet LDI configuration, or Configuration 1. The next configuration is used to measure freestream disturbance levels in a Mach 2 wind tunnel, and will be referred to as Configuration 2. The third configuration is used to measure turbulent length scales associated with a laser-induced disturbance, and will be referred to as Configuration 3. Table 1 shows the parameters of the hardware used on the different LDI configurations.

The optics used in configuration one are shown in Figure 6 and Figure 7, and Figure 8 shows the LDI schematic for the three configurations according to the parameters listed

Table 1- Hardware and characteristics of the optics used for the three LDI configurations.

	Configuration 1	**Configuration 2**	**Configuration 3**
Polarizer	Thorlabs LPVISE100A	Thorlabs LPVISE100A	Thorlabs LPVISE100A
Lens, f_1	f = 75mm achromatic d = 25.4 mm	f = 75mm achromatic d = 25.4 mm	f = 75mm achromatic d = 25.4 mm
Wollaston Prism, ε	Thorlabs WPQ10 ε = 1°	United Crystals ε = 2′	Thorlabs WPQ10 ε = 1°
Field Lens, f_2	f = 100 mm achromatic d = 75 mm	Nikon f = 50 mm d = 35.7 mm	Nikon f = 50 mm d = 35.7 mm
Photodiode	Thorlabs DET36-A	Thorlabs DET36-A	Thorlabs DET36-A
Beam spacing, δ	1.8 mm	30 μm	900 μm

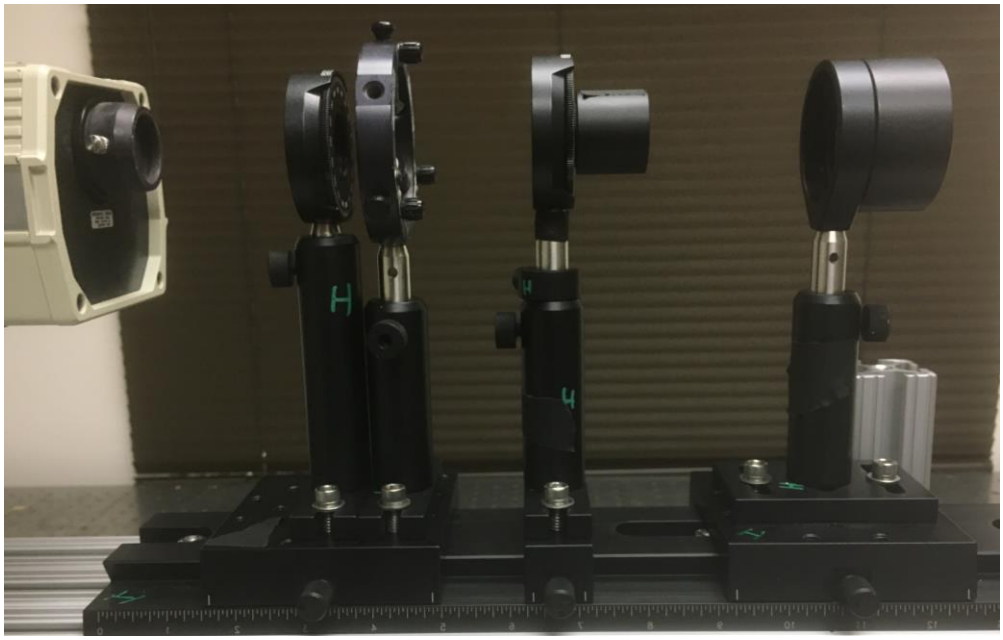

Figure 6- Image of the optics used to transmit the LDI beam pair.

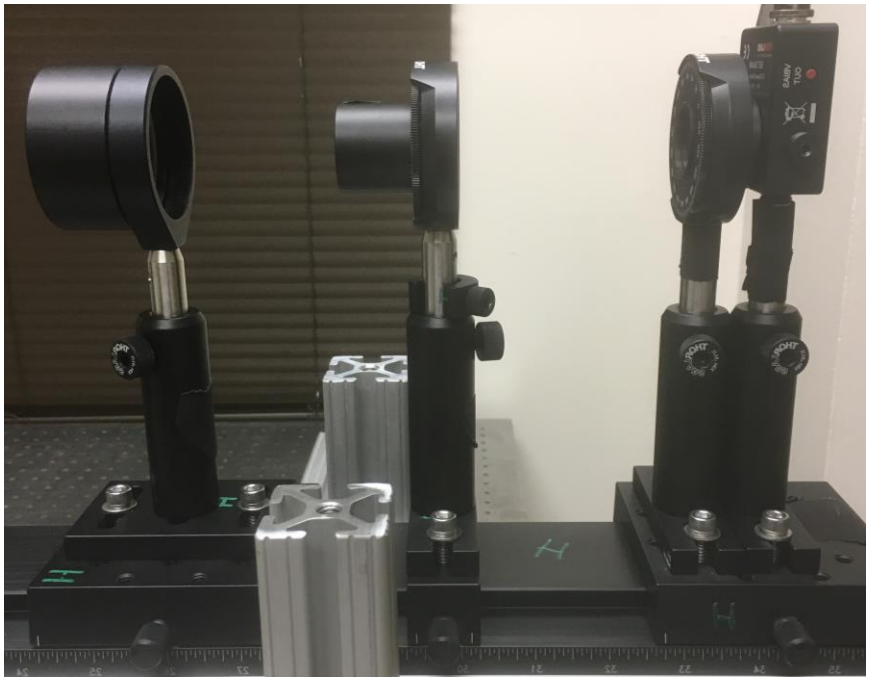

Figure 7- Image of the optics used to receive the LDI signal and convert it to a voltage for acquisition.

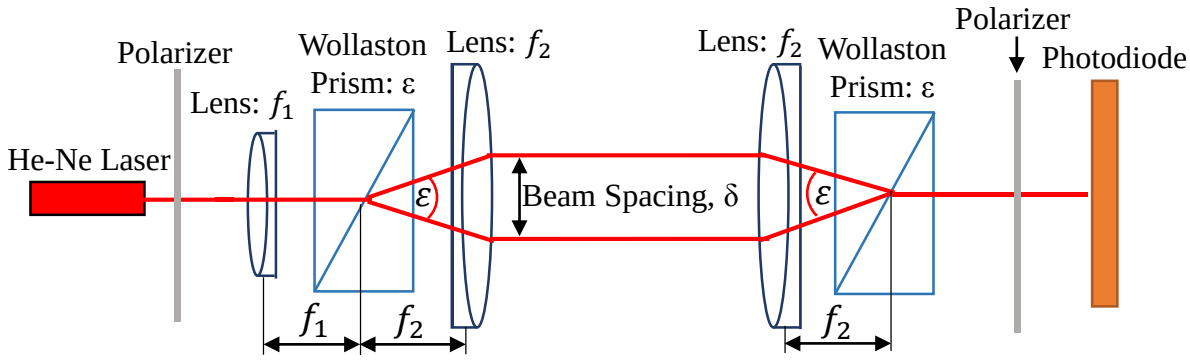

Figure 8- Schematic of the LDI configuration according to the parameters shown in Table 1.

in Table 1. The laser used in this work is vertically polarized, which will be considered 90°, as the direction of fluid dynamics that the system measures is perpendicular to this, at 0°. Moving from left to right along the image, the first optic that the light encounters is a Thorlabs LPVISE100A linear polarizing filter. This filter is set to 45°. Next, the beam is passed through a 76.2-mm (3-in) focal length lens, and then a Thorlabs WPQ10 Wollaston Prism, which is placed 1 focal length away from the lens. The Wollaston prism is rotated such that the incoming light is polarized at 45° relative to the fast axis of the prism, ensuring that the resulting beam pair are polarized at 0° and 90° respectively, with equal power. This model of Wollaston prism has a 1° divergence angle. Finally, the beam is passed through a Thorlabs AC508-100A 100-mm focal length achromatic lens that is also placed one focal length from the Wollaston prism. By placing these two lenses at their respective focal lengths from the Wollaston prism, the beams are collimated, remaining constant diameter, and at a constant spacing with respect to each other throughout the test volume. This is of significant importance, as the beams must remain parallel and constant in size to recombine and interfere properly. Given the focal length of the lenses used and the beam divergence angle of the prism used, the beams have a beam diameter of approximately 1.4 mm.

After the beam pair traverses the measurement volume, a set of optics is used to recombine and interfere the beams. First, the beam pair encounters another Thorlabs AC508-100A achromatic lens, and WPQ10 Wollaston prism identical to the lens and prism used previously. Once again, the lens is placed one focal length away from the Wollaston prism, at which point the beams will recombine and interfere. The second Wollaston prism is then adjusted so that the beams, when undisturbed, will interfere 50%. The beam is then passed through another Thorlabs LPVISE100-A linear polarizer, where any interference will be measured as a change in intensity, and finally onto a Thorlabs DET36-A photodetector. All electrical leads are terminated by a 1-kΩ resistor to maximize the signal-to-noise ratio, and minimize the discretization error.[14]

The second LDI configuration is almost identical to the first beam configuration; however instead of a ThorLabs WPQ10 Wollaston prism, with a beam divergence angle of 1°, a United Crystals Wollaston Prism is used with a beam divergence angle of 2′. Also, the 100-mm field lenses are replaced with Nikon f/1.4 50 mm lenses in order to produce a beam spacing of 30-μm. The optics are adjusted such that the Wollaston prism is still set at the focal length of the lenses, once again ensuring constant beam diameter and beam spacing. This configuration enables a much wider bandwidth of measurements, at the cost of signal strength. The third configuration only differs from the first configuration in that the 100 mm field lenses have been replaced with Nikon f/1.4 50-mm lenses, producing a beam spacing of 900 μm. This produces a beam spacing that allows the smallest expected turbulent scales to be resolved, while still producing a reasonable signal-to-noise ratio.

Data acquisition is accomplished through the use of a Teledyne LeCroy Waverider 10 10-GHz oscilloscope. A low-pass, 8^{th} order Butterworth filter is applied to the data in order to remove high frequency electronic noise from the signal. Data from the jet calibration were sampled at 500 kHz in 10-s blocks. power spectral densities were calculated using a Hann window with 50% overlap, and a block size of 25,000 points. Data collected for freestream disturbance level measurements were collected at 1 MHz, in 5-s blocks. Data collected from the laser-induced disturbance is collected at 100 MHz in 1.5-ms blocks.

3.3 Calibration Jet

In order to validate the response of the LDI, measurements were initially made within the well-known free jet flow field. Two jets were used, the first was a simplistic jet created by using steel tubing with an outer diameter of 6.4 mm, and an inner diameter of 4.3 mm, which was placed 25 mm downstream of a regulator so that constant pressures of 136 kPa (5 psig) and 170 kPa (10 psig) can be maintained and head loss would be negligible. The second jet is a converging nozzle with an outlet diameter of 12.7 mm, and a stilling chamber just downstream of a regulator, shown in Figure 9. An Omega™ 101-446 kPa (0-50 psig) pressure transducer measures the stagnation pressure of the jet. These jets are mounted on a Velmex BiSlide® 254-mm linear traverse such that the jet's position can be adjusted with an accuracy of 0.076 mm. A LabView™ virtual instrument is used to drive the jets, and the jets are moved across the LDI such that the profile of the jet can be measured while the LDI system remains stationary. The parameters of the jet are shown in Table 2, where the velocity and the Reynolds numbers are calculated using basic isentropic flow relations. Figure 10 shows a map of where points were sampled on the free jets, and are non-dimensionalized by their diameters. The 4.3-mm diameter jet was measured at the

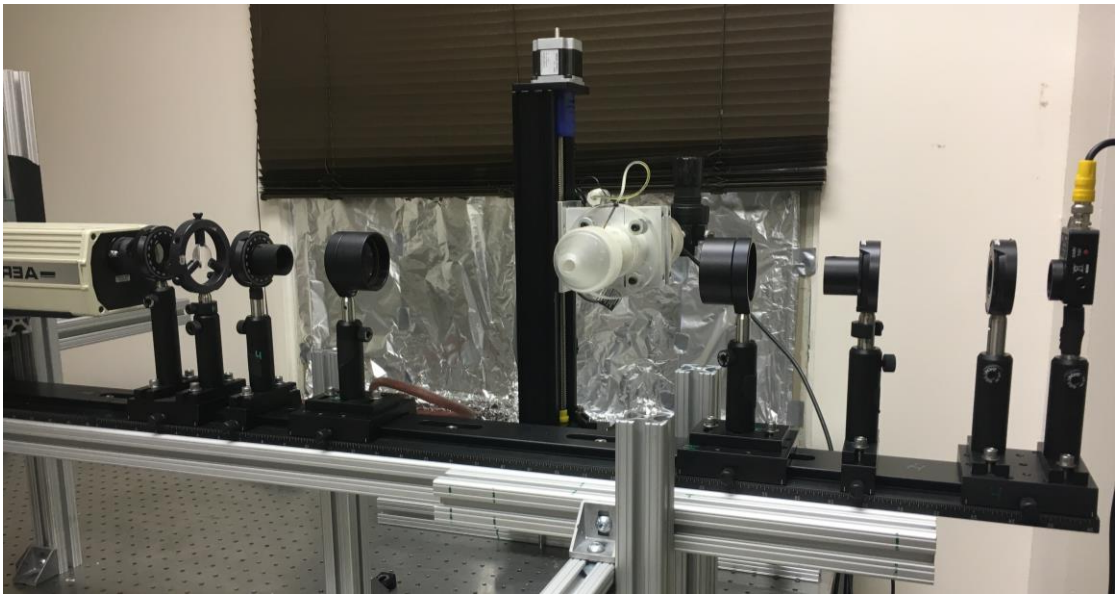

Figure 9- Image of the jet calibration experiment with the 12.7-mm jet in use.

Table 2-Key parameters for the jets used to validate the LDI system.

	Diameter (mm)	Pressure (kPa)	Velocity (m/s)	Reynolds number
Jet 1	4.3	136	284	107,200
Jet 2	4.3	170	217	76,900
Jet 3	12.7	103	50	46,800

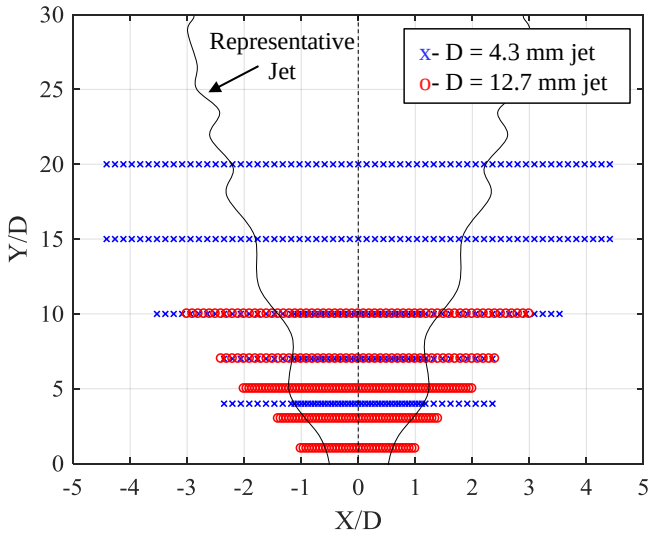

Figure 10- Physical location of the data points taken on the different diameter jets.

same locations for both the 136-kPa and 170-kPa cases. Due to physical spacing constraints in the lab, the 12.7-mm diameter jet could only be measured out to a Y/D = 10. LDI Configuration 1 is used to measure dynamic content in the jet.

3.4 Unsteady Pressure Transducers

Kulite^{TM} XCE-062-025 unsteady pressure transducers were used throughout this work The pressure transducers were placed along the centerline of the floor of the tunnel spaced 50.8 mm (2 in) apart. For results presented in different sections, the Kulites were sampled at 200 kHz and 1 MHz. When sampled at 200 kHz, an 80 kHz, low-pass, 8th order Butterworth filter is applied. The results are unfiltered at 1 MHz, as the system dynamics naturally filter out excessively high content. The Kulites were powered and amplified with a gain of 100 by a circuit that was developed at UTSI, and their signals were acquired simultaneously on an NI USB-6356 DAQ system.

3.5 Schlieren

The Schlieren system, represented in Figure 11 uses a pulsed LED light source that was built at UTSI. It can achieve pulses as low as 500 ns in duration, though 1250 ns is typical for the work presented here. A pair of 2.67-m focal length mirrors are used to collimate the light, and a knife edge is placed so as to serve as a horizontal spatial filter. A Photron FASTCAM Mini UX-100 is used to acquire the images at 50 kHz. When imaging the turbulence resulting from laser-induced breakdown, a 532-nm notch filter is placed in front of the camera, which corresponds to the frequency of the laser used to generate the laser-induced disturbance. This ensures that no laser light damages the sensor.

3.6 Laser-Induced Disturbance

Laser-induced disturbances have been used by a variety of researchers to force boundary layer transition, aid combustion, or study receptivity.[28,31,32,38] For this work, the laser generated disturbance is created using a pulsed, frequency-doubled Nd:YAG laser that produces 532-nm light. Typical pulse durations were measured to be 7 ns, and the

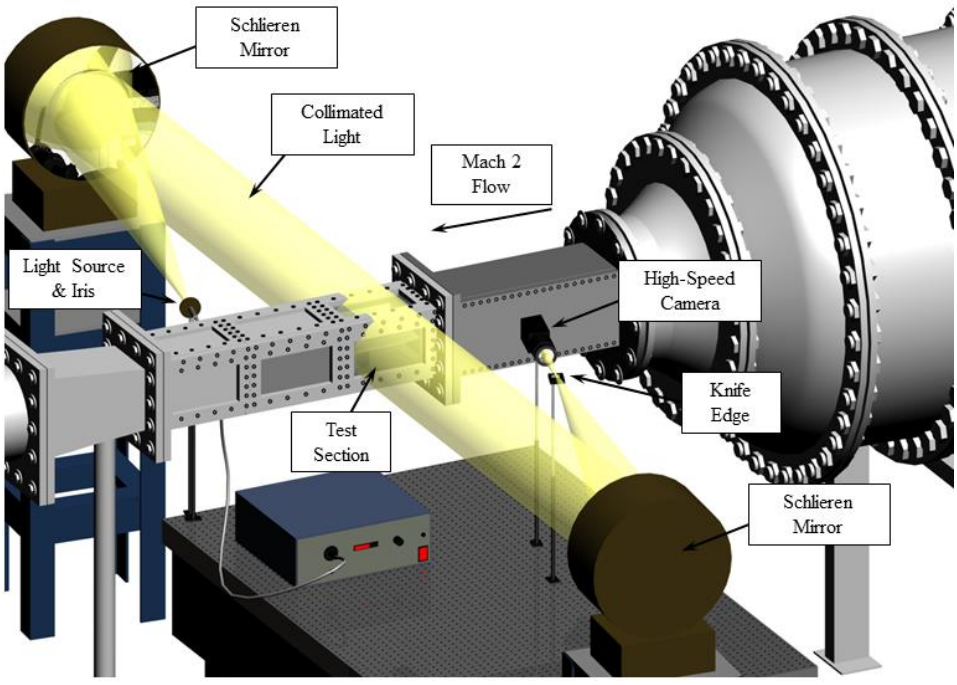

Figure 11- Schematic of the Schlieren setup used to in this work.

energy per pulse was ~120 mJ at a repetition rate of 10 Hz. The laser is routed into the wind tunnel through the use of a series of laser-line mirrors. The laser is then focused using a 250-mm focal length lens such that the laser-induced disturbance is injected at the centerline of the wind tunnel.

Throughout this work, two different experimental implementations of the laser-induced disturbance were used. The first was used to measure the acoustic radiation that results from the disturbance being injected into the boundary layer of the test section floor. This configuration is illustrated in Figure 12 and Figure 13. In this experiment, the laser-induced disturbance is injected 3 mm above the test section floor (the boundary layer thickness is approximately 11 mm) along the center plane of the test section at 120 mJ/pulse. Two high-speed pressure transducers are spaced 50.8 mm apart from each other, also along the center plane of the test section, several centimeters downstream of the laser-induced disturbance. LDI configuration two is used, and is placed 70 mm downstream of the Kulite pair, and 55 mm above the test section floor, and 52 mm above the position of the laser-induced disturbance. This spacing was selected to place the LDI measurement volume at an angle of approximately 36° relative to the position of the disturbance above downstream pressure transducer and the flow direction. This corresponds to the expected angle of acoustic radiation in a Mach 2 flow.[12] This experiment is also repeated, switching out the LDI for time-resolved Schlieren, which provides global flow visualization. Figure 14 shows a typical beam-routing configuration for all experiments that utilize the Nd:YAG laser. The second experimental configuration that uses the laser-induced disturbance is designed to measure the thermal disturbance itself, rather than the acoustic radiation that results.

The laser disturbance is injected approximately 100 mm above the test section floor along the centerline. LDI Configuration 3 is placed such that its measurement volume is at the same height above the test section floor and approximately 165 mm downstream of the location of the laser-induced disturbance. The response of the LDI to the laser-induced is observed in quiescent air and Mach 2 flow and is repeated again repeated with Schlieren, instead of the LDI system. Figure 15 shows a schematic of the experiment used to measure the thermal disturbance with the LDI system.

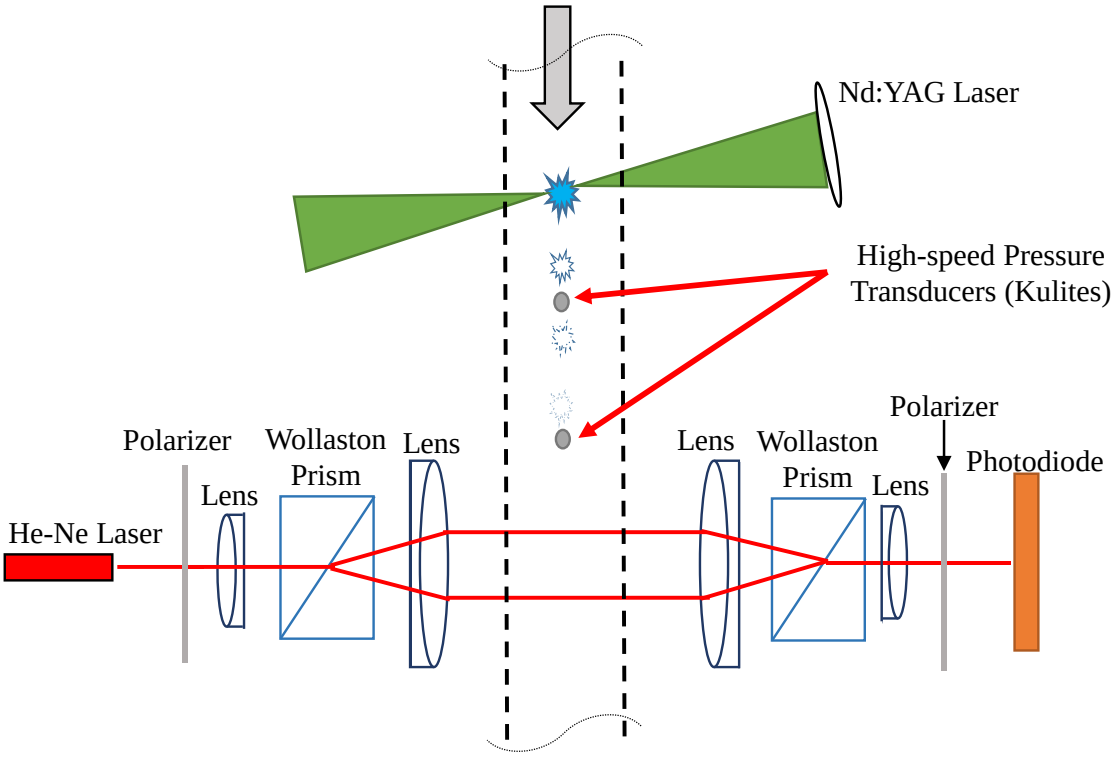

Figure 12- Schematic of the laser-induced perturbation experiment.

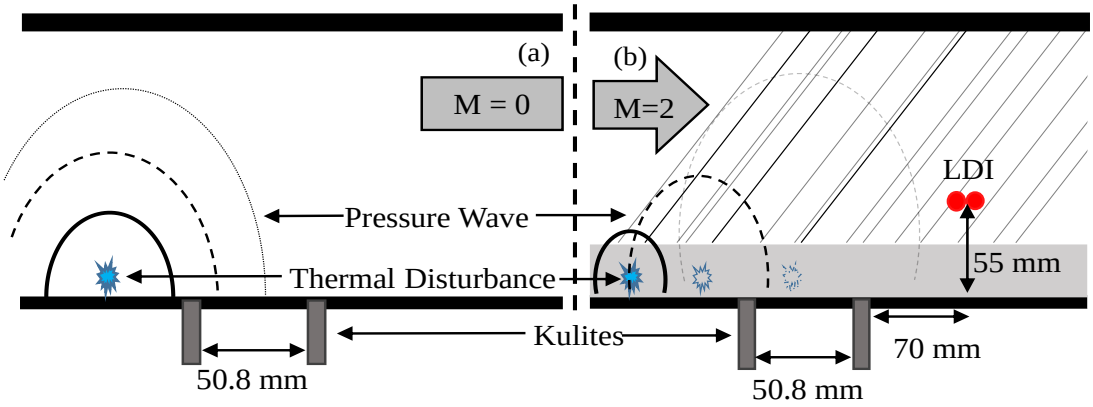

Figure 13- Side-view schematic of the forced perturbation and the resulting pressure wave propagating over the unsteady pressure transducers in (a) quiescent air and (b) Mach 2 flow.

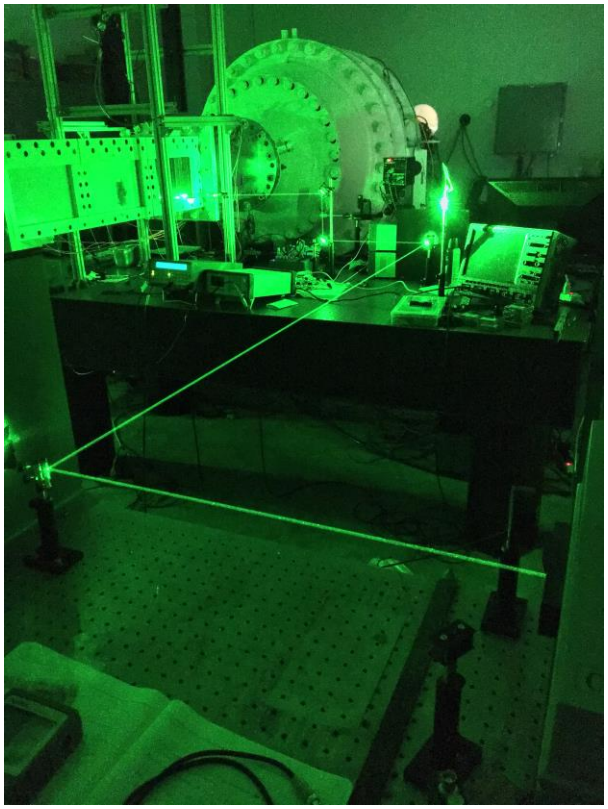

Figure 14- Image of the Nd:YAG laser path into the wind tunnel.

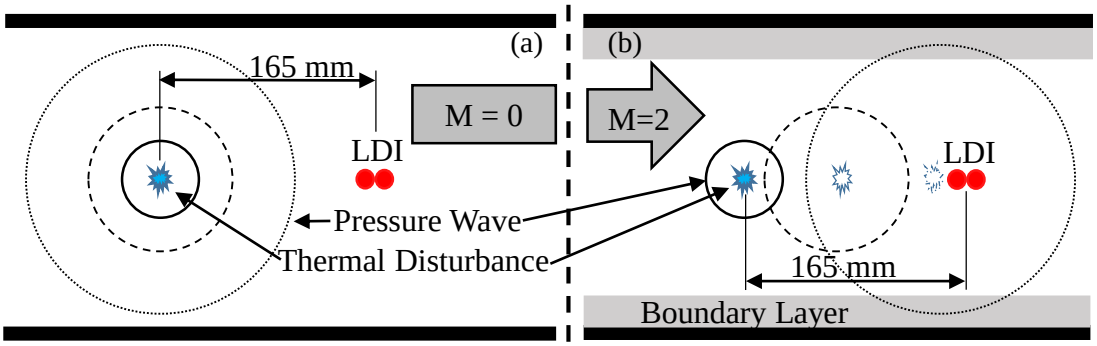

Figure 15- Schematic of the experiment used to make LDI measurements of the thermal disturbance in (a) quiescent air and (b) Mach 2 flow.

CHAPTER FOUR
CALIBRATION AND VALIDATION OF THE LDI SYSTEM

In order to validate the response of the LDI system, the system response was determined for a well-known flow field. Free jets are a well-documented phenomenon and have been used in previous work to validate the response of laser diagnostics.[14,49] The theory behind incompressible jet flow is well established, and certain characteristics of free jets make them well-suited for such an experiment.[50] Subsonic jets have been shown to be self-similar in the fully developed region such that certain normalization parameters can be defined, for which all profiles demonstrate the same characteristic shape. Results presented in this chapter were collected using a 4.3-mm diameter jet at pressures of 136 kPa and 170kPa, as well as a 12.7-mm diameter jet at 103 kPa. The jet was moved across LDI Configuration 1 by means of a linear slide, and data were sampled at each position, shown in Figure 10. Profiles of the turbulence in the jet are shown at varying axial locations, jet supply pressures and jet diameters. Spectra of the LDI response are presented and compared as a function of the axial and radial jet directions. Finally, the self-similarity of the jet profiles collected under different conditions is shown in order to present a holistic recreation of a canonical experiment.

4.1 Demonstration of Linearity

An important aspect of validating the response of an LDI system is to ensure that there is no phase ambiguity in the system, and that the signal is limited to the linear portion of the interference curve. Figure 16 shows the time histories of the 170-kPa jet at its centerline at several axial locations measured by the LDI, compared to the interference curve for the system. The mean voltage of the undisturbed LDI system is typically about 550 mV. The mean voltage resulting from complete constructive interference and complete destructive interference was 1,050 mV, and 50 mV respectively. These results are typical of all experiments, and were validated before testing by adjusting the Wollaston prism to determine the maximum and minimum voltages.

The centerline signals are expected to have the largest amplitude fluctuation compared to off-axis measurements, so these results are representative of the entirety of

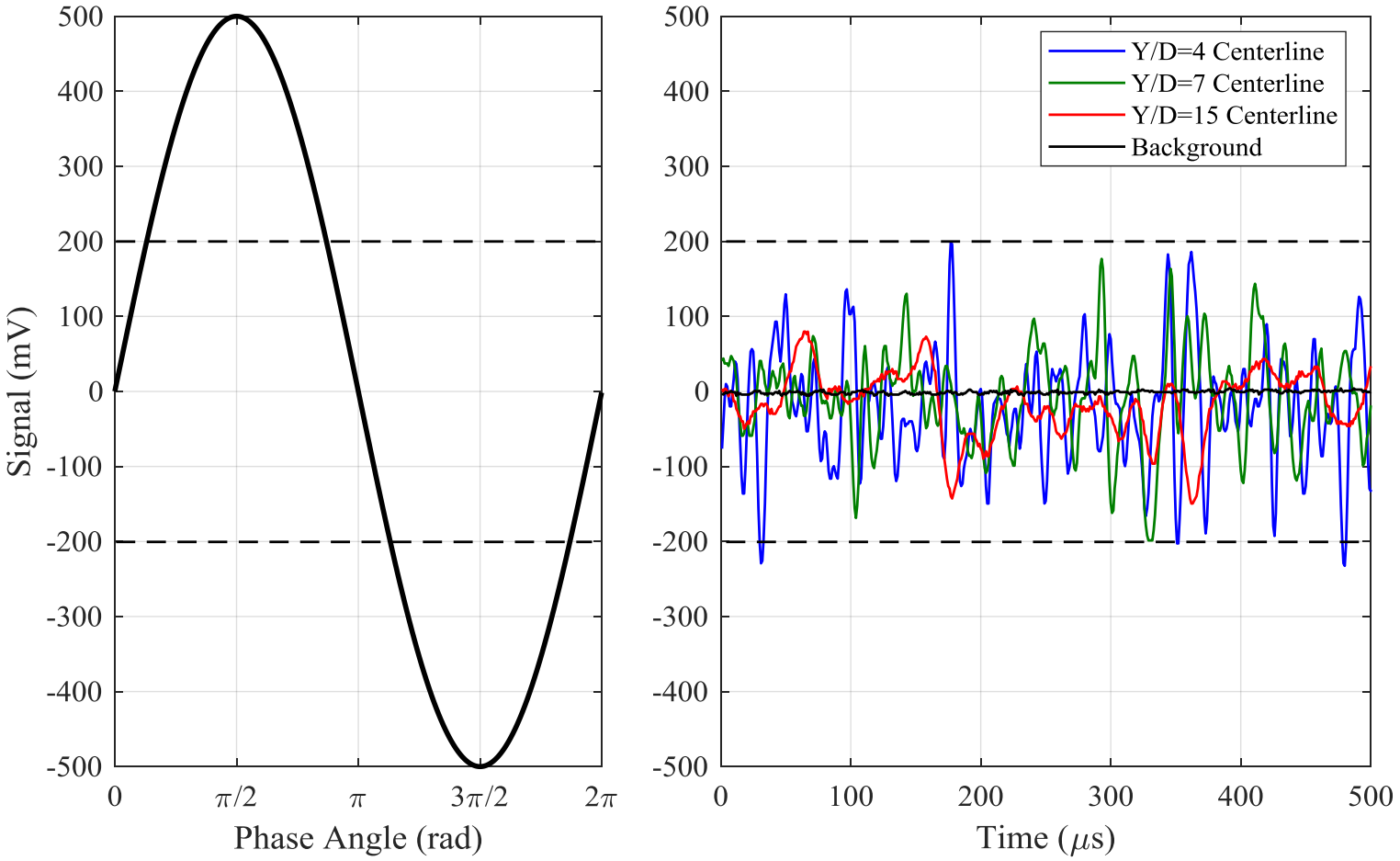

Figure 16- Time histories of the LDI response at the centerline of the jets at different axial locations compared to the interference curve to demonstrate linearity and no phase ambiguity.

the jet profile data shown. As indicated by Figure 16, the LDI signal is free of phase ambiguity, and restricted to the linear portion of the curve, ensuring a linear response of the LDI system. It is also interesting to note that the amplitude of fluctuations decreases as axial distance increases. Inspection of the background signal time history in comparison to the centerline time history shows that the signal-to-noise ratio, calculated by the variance of the signal divided by the variance of the background is sufficiently high, in excess of 20 at the centerline. These results show that the LDI system developed for this work does indeed respond to fluctuating density gradients in the flow linearly, and that the system adheres to typical operational parameters of interferometric techniques.

4.2 Effects of Jet Supply Pressure

The results of the profile taken with a 4.3-mm diameter jet at 170 kPa are shown in Figure 17. The LDI signal is expressed as a density gradient normalized by the local density using Eq. (3), and the variance of this signal is used to show the amplitude of fluctuations at any position in the jet. Uncertainties were calculated using the variance of the background signal measured just before taking data, and the positions are non-dimensionalized by the diameter of the jet itself, Y is the jet axial direction, and X is the jet transverse direction, and the variance measured from the LDI is shown at each position. The maximum value can be seen to decrease with increasing distance from the jet nozzle, showing the intensity of turbulence decreases, which agrees with theory. Profiles at Y/D = 4 and Y/D = 7 have a certain degree of asymmetry, where the maximum value tends to be off center. This may be attributed to experimental factors, such as the nozzle fabrication, misalignment or the presence of a potential core flow, as 170 kPa is approximately the pressure required to choke the flow. The full width at half maximum (FWHM) tends to increase with axial distance, indicating growth as the jet propagates outward. Once again, this agrees with theory.[50]

While the magnitude of density fluctuations at each position of the jet is informative, more information about the behavior of the jet can be derived from examining the spectra at each position. Figure 18 shows the power spectral densities of the photodiode signal at select radial locations at an axial distance of Y/D = 7, where the spectra have been

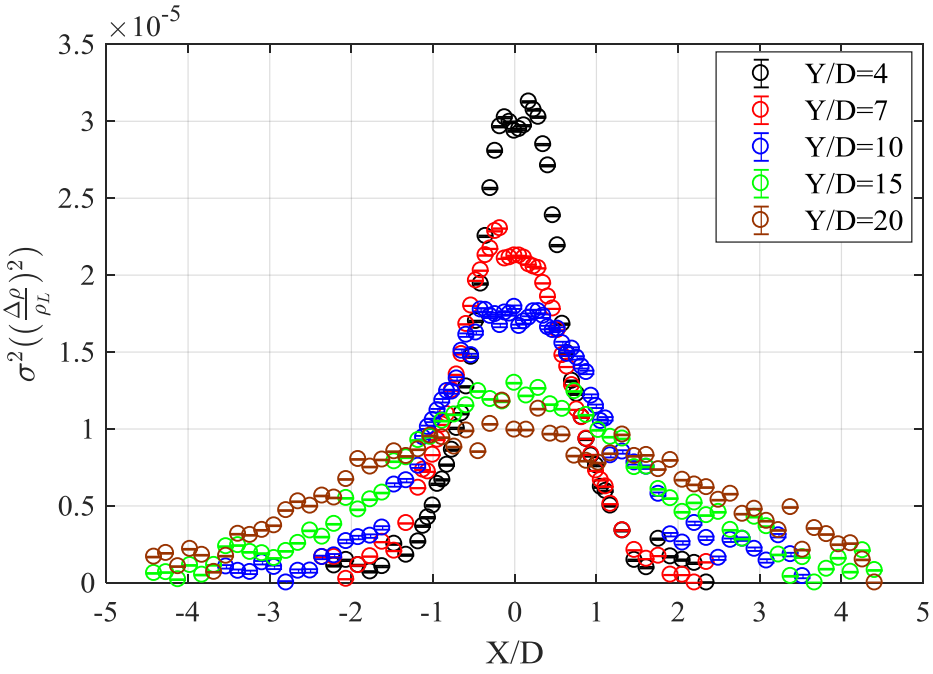

Figure 17- Jet profiles of a 170-kPa jet with a 4.3-mm diameter.

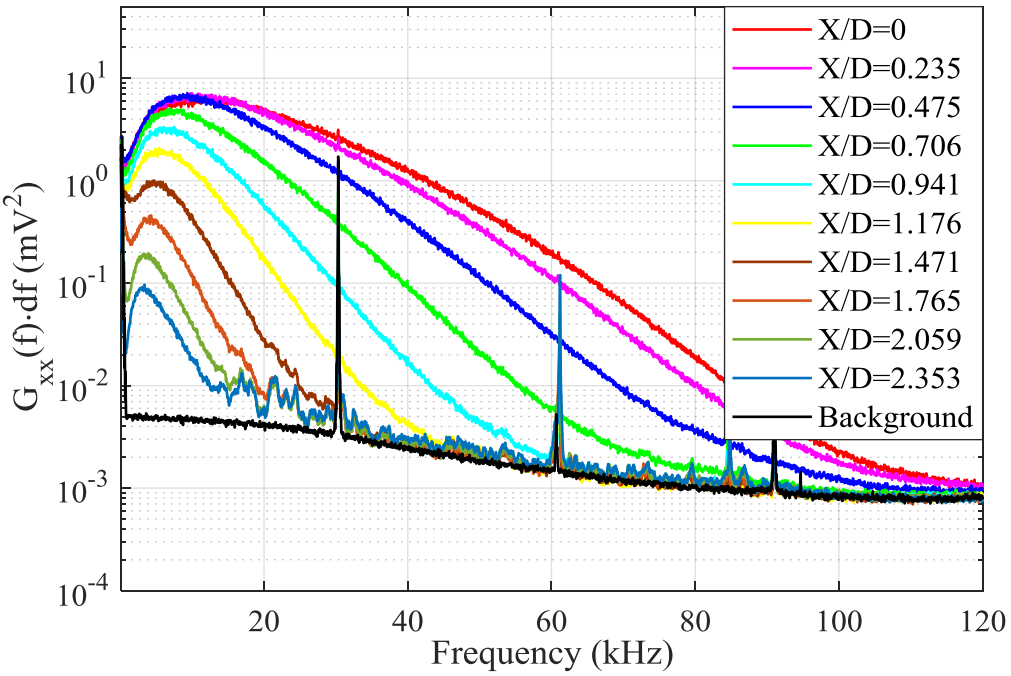

Figure 18- Spectra of turbulent content present at several radial locations for a 170-kPa jet at an axial distance of Y/D = 7.

normalized by the frequency resolution, df = 40 Hz. Several characteristics can be observed from the spectra that are not inherently obvious from the jet profile itself. As expected, the area under each curve tends to decrease, corresponding to the decrease of the variance. The slope with which the frequency content rolls off tends to become more negative as the radial distance increases. The bandwidth tends to decrease as the radial distance increases, indicating that there is less high frequency content associated with smaller turbulent structures as distance from the axis increases. A peak can be observed in each spectra (typically 10 kHz or below) that corresponds to the larger turbulent structures present in the jet. It can be seen that this peak frequency decreases as radial distance increases. In theory, as the radial distance increases, the convective velocity of the local fluid will decrease, as the jet fluid is shearing over the quiescent air. When considering this in the context of the LDI measurement, it can be seen that larger, structures are observed more as the measurement volume is moved off axis with respect to the jet. In general, this is consistent with documented theory.[50]

Examining the results of a 4.3-mm diameter jet at 136 kPa, shown in Figure 19 generally similar behavior can be observed. The overall magnitude of the jet profiles are lower by more than a factor of four: however, it can be seen that the magnitude of variance at the centerline of the jet tends to decrease as axial distance increases, and the full width at half maximum increases as the axial distance increases. This indicates that regardless of supply pressure, the same general trend can be observed. There is still a certain level of asymmetry in the Y/D = 4 profile, however the Y/D = 7 profile at 136 kPa does not demonstrate the same asymmetry as the Y/D = 7 profile at 170 kPa. This may be attributed to the lower pressure that would result in a smaller region of potential core flow.

The spectra of the 136-kPa jet at Y/D = 7 is shown in Figure 20 at the same radial locations as Figure 18. The general trend is the same as observed before, where the total area under the curve, corresponding to the variance tends to decrease as the radial distance increases. The slope of the spectra roll off tends to be much more negative than what is observed in the 170-kPa case. This is to be expected, as lower supply pressure will correspond to a lower Reynolds number, and thus an increase in the size of the smallest scales of turbulence. In addition, lower pressures will result in lower jet velocities, which

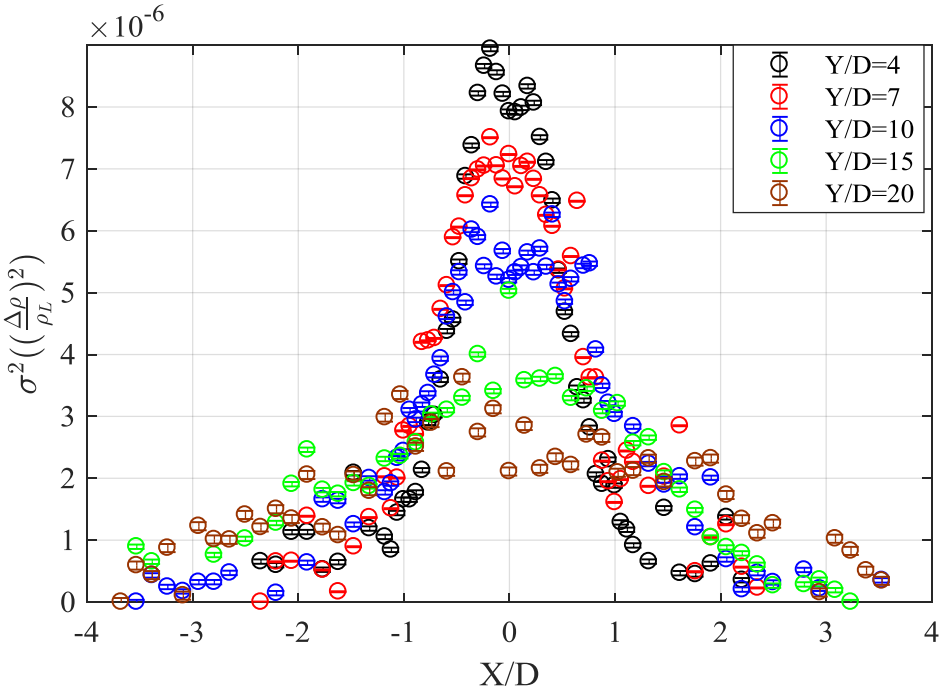

Figure 19-Jet profiles of a 136-kPa jet with a 4.3mm diameter.

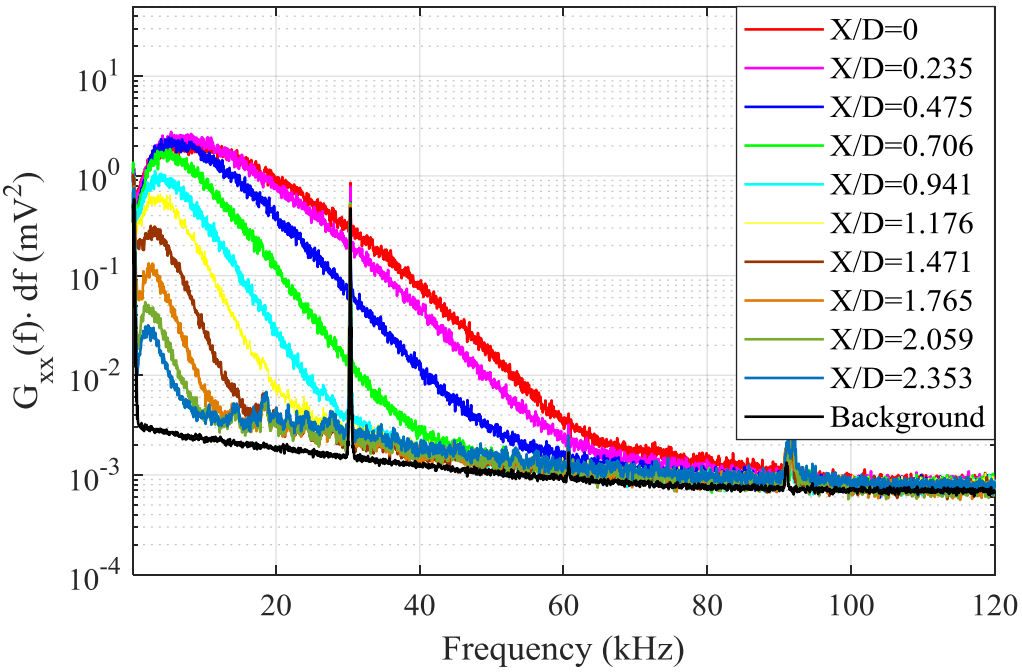

Figure 20- Spectra of turbulent content present at several radial locations for a 136-kPa jet at an axial distance of Y/D=7.

implies that turbulent structures of the same length scale are now at a lower velocity, and will have a proportionally lower frequency associated with it. Indeed, the bandwidth of every spectra shown is significantly reduced compared to the 170-kPa case. For example, the X/D = 0.941 bandwidth extends out to ~110 kHz at 170 kPa, whereas it only extends out to ~60 kHz in the 136-kPa case. Peaks in the spectral content are present in both the 136-kPa case and the 170-kPa case; however, both the magnitude and frequency at which these peaks occur in the 136-kPa case are lower than the 170-kPa case. It is interesting to note that the peak frequency is approximately equal in magnitude from the centerline out to X/D = 0.475, however, the frequency where this peak occurs decreases. As the radial distance continues to increase, both the magnitude and frequency of this peak decreases.

Spectra for the jet along the radial direction have been presented and discussed, and a comparison of how this differs from the spectra measured along the axial direction is warranted. Figure 21 shows the spectra of the response of the LDI at the centerline of the 136-kPa jet at axial locations of Y/D = 4, 7, and 10. The bandwidth of these spectra

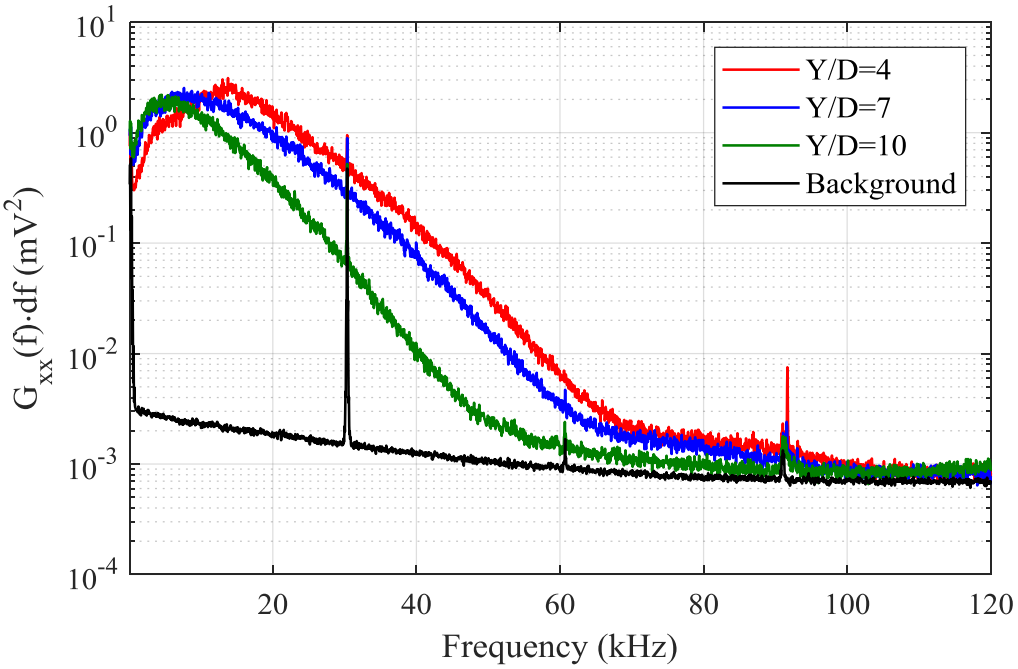

Figure 21- Spectra of the LDI response to the 136-kPa jet along the centerline at different axial locations.

decrease along the jet axial direction at a much slower rate that the bandwidth of the spectra along the radial direction. This is to be expected as the centerline of the jet contains the highest momentum flow, and spatial variations of turbulent content along the axial direction will be more exclusively associated with the dissipation of energy. Spatial variations of the turbulent content in the radial direction may be associated with boundary layer effects along the walls of the jet nozzle, turbulent mixing with the ambient air, and dissipative effects, thus leading to a more rapid decay in frequency content present along the radial direction.

It is interesting to note that the slope of the spectra for the axial locations of Y/D = 4 and Y/D = 7 cases are very similar, and that the slope of the axial location Y/D = 10 case is only marginally smaller than the two other cases. Furthermore, a decrease in the peak frequency can be seen as axial distance increases. This may be attributed to the growth of the free jet, as well as a reduction in the velocity of the largest scales of turbulent structures that pass over the LDI measurement volume. A slight decrease in the amplitude of this peak can also be observed as axial distance increases; however, this is trivial in comparison to the decrease in the peaks present when examining the spectra along the radial direction.

4.3 Effects of Jet Diameter

The final jet profiles that are presented were collected from a jet with a diameter of 12.7 mm. This jet has a stilling chamber and turbulence screens present. Due to the larger flow area, pressures of 136 kPa and 170 kPa could not be achieved with the current setup; however, a pressure transducer connected to the stilling chamber measured the stagnation pressure to be approximately 103 kPa throughout the experiment. Figure 22 shows the profiles of the 12.7-mm diameter jet collected at axial locations of Y/D = 1, 3, 5, 7, and 10. While similar in general trends, a few unique features can be observed. The region of potential core flow can still be seen in the Y/D = 1 and 3 cases, and the variance at the centerline is approximately equal for these two cases. When looking at the Y/D = 5 case it may be observed that the area under the curve is larger than in the Y/D = 3 case. This may be attributed to both the jet growth, and the path-integrated nature of LDI. The jet will cover a larger portion of the measurement volume, producing a higher amplitude signal.

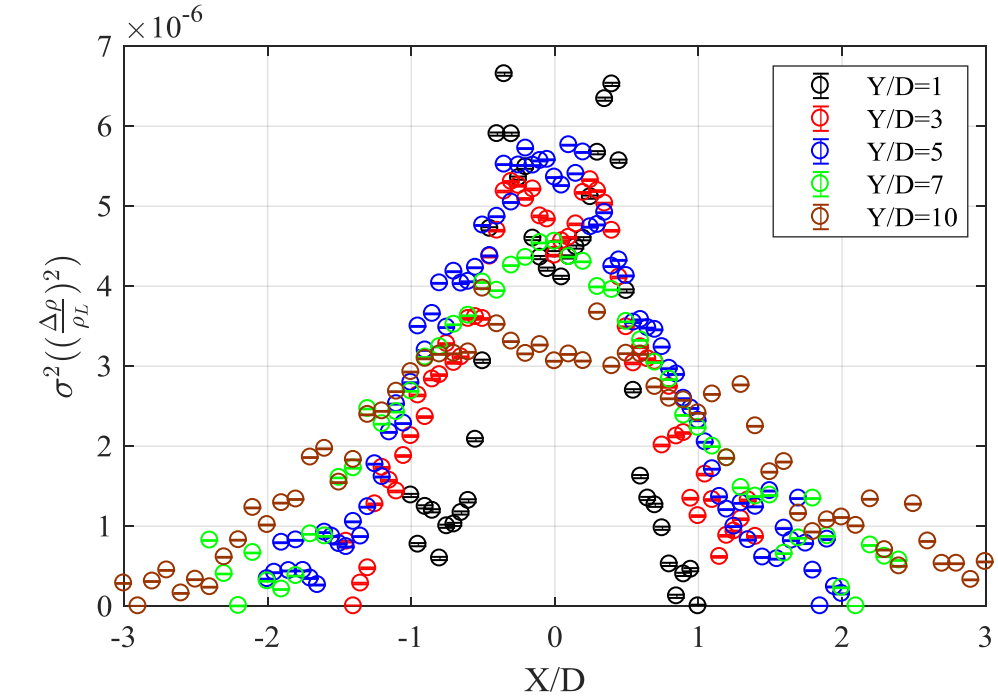

Figure 22- Jet profiles of a 12.7-mm jet at low pressures.

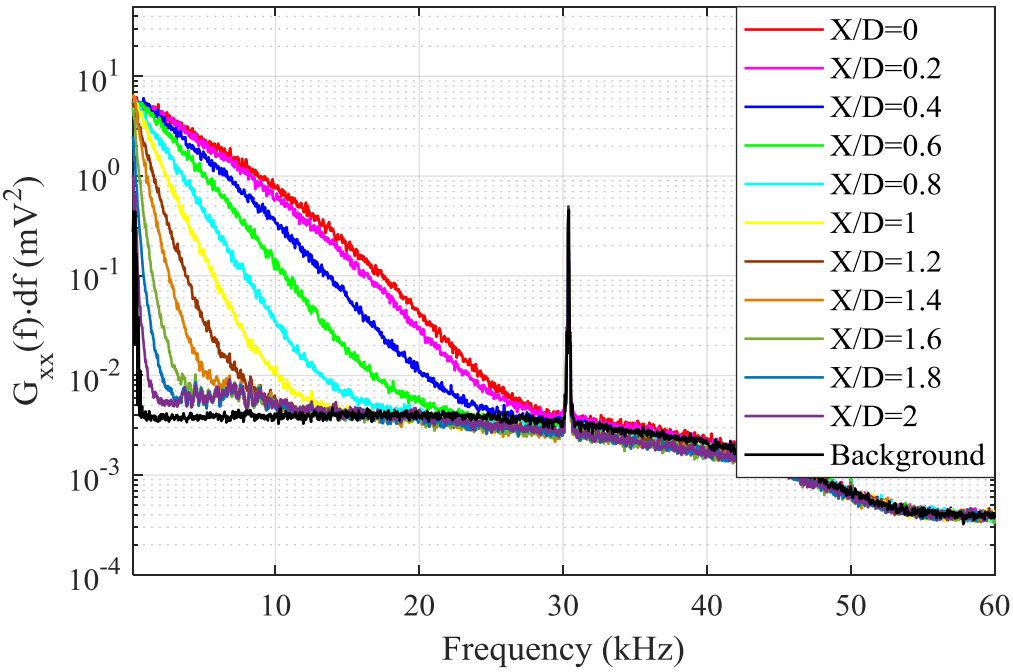

Figure 23- Spectra of the turbulent content present at an axial location of Y/D=7 at a variety of X locations.

This phenomena was also observed by Cerruzi et al.[49] Despite these differences, it can be seen that in general structure the LDI does indeed measure the jet as expected.

Looking further into the data, the power spectral densities of the jet along the radial direction can be examined. Figure 23 shows the spectra of the jet at several positions along the radial direction. Again, the general trend shown here is that the area under the curve tends to decrease as radial distance increases, and the bandwidth of turbulence decreases as well. It is interesting to note that the frequency peak present in the previous two jet profiles is no longer present, as the diameter of the jet has increased and the velocity of the jet has decreased, resulting in a lower expected maximum frequency in the turbulent jet. The overall bandwidth of this jet is significantly smaller than the higher pressure, 4.3-mm jets, with a centerline bandwidth of only 30 kHz, where the 4.3-mm diameter jets at 136 kPa and 170 kPa had centerline bandwidths that extended out to 60 kHz and 110 kHz respectively. This is to be expected as the Reynolds number of the 12.7-mm jet is much lower than the Reynolds number of the 4.3-mm jet, resulting in a change in the smallest scales of turbulence.

4.4 Self-Similarity and Growth Rate

So far, the results presented have discussed the ability of the LDI to respond to a variety of different jet parameters, including supply pressure, characteristic length, and as such, Reynolds number, and have demonstrated that the LDI presents results in-line with what generally accepted theory predicts. Another well-known property of jets is the self-similarity of their profiles. Self-similarity shows that jet profiles collected at different parameters, such as Reynolds number, or axial distance can be normalized with similarity scales such that all profiles collapse along a single curve. The parameter used to normalize the jet profile's Y-axis is typically the maximum velocity, however since the LDI measures dynamic content, the maximum variance is used instead. The X-axis is normalized by the full width at half maximum, with respect to the maximum variance. The results of such a normalization are shown in Figure 24, where select profiles from the three different jet cases are displayed. While there is some spread in the data, it can be shown that the profiles do indeed collapse along a single curve.

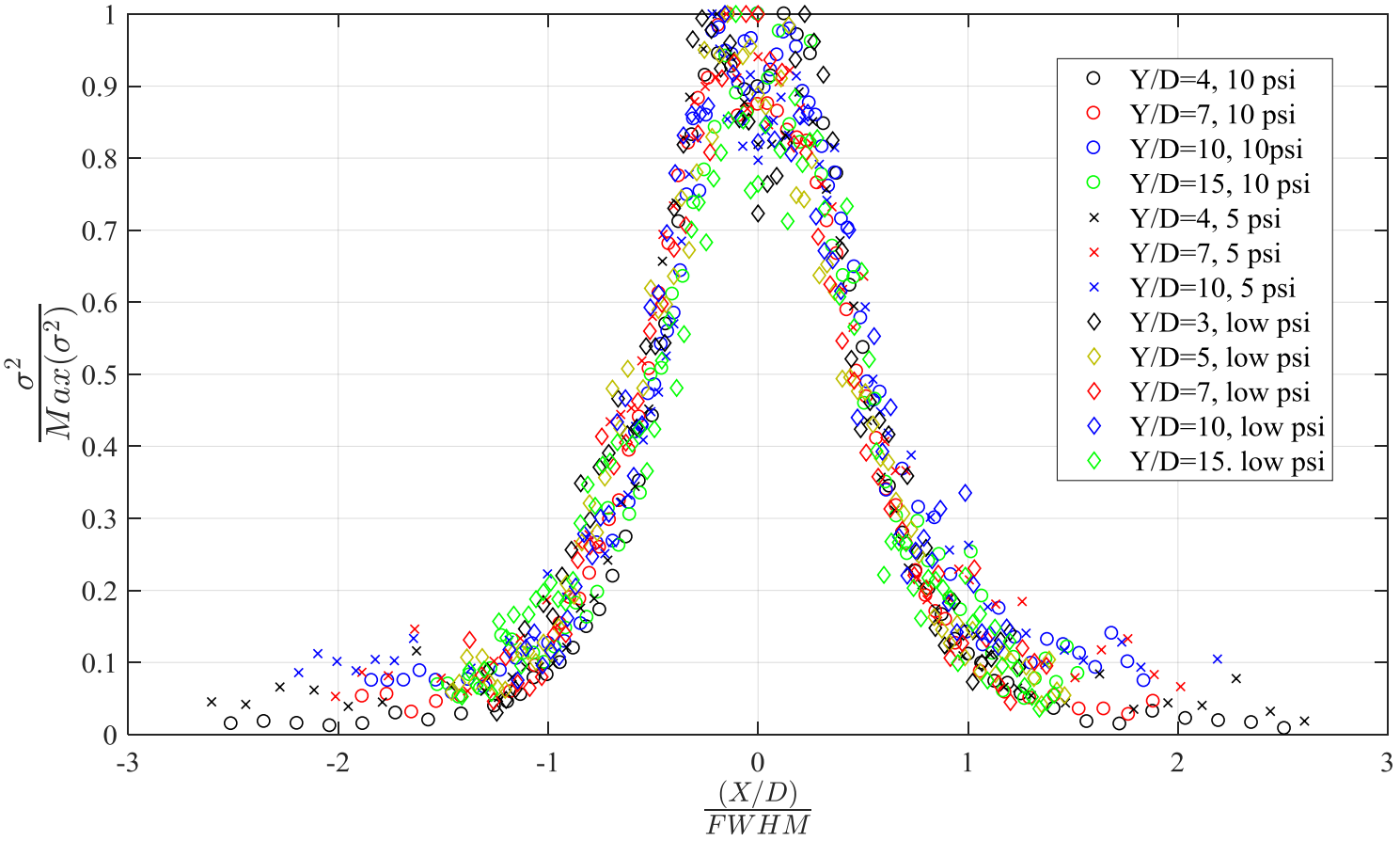

Figure 24- Self-similar results from the data previously shown non-dimensionalized by the FWHM and maximum variance values of each jet.

Another common parameter for jets is their spreading rate, S[50]. The spreading rate is typically defined as the change in half radius with respect to the axial direction. The spreading rate has been found to be largely independent of Reynolds number, at a value of approximately 0.096[51,52]. When the spreading rate of the 4.3-mm diameter jet at 170 kPa and 136 kPa is calculated, it is determined to be 0.0916 and 0.107, with an average value of 0.0967, agreeing with what is theoretically predicted and what has been measured before experimentally.

Overall, this calibration demonstrates that the LDI does indeed measure dynamic content associated with turbulent fluctuations in a fluid dynamic environment. Furthermore, it shows that the LDI can reproduce results from a canonical experiment in fluid dynamics, namely the free jet profile. This instills some confidence in the use of the LDI in other applications, having some understanding of how the system responds to a well-understood phenomena. The LDI presented here demonstrates a relatively high bandwidth, measuring results out to approximately 100 kHz, and literature has shown that, when properly configured, an LDI system is capable of responding to much higher content, well into the MHz range.[13]

CHAPTER FIVE
LDI TUNNEL AND PERTUBATION MEASUREMENTS

Laser differential interferometry provides a unique opportunity to measure the behavior of laser-induced disturbances. Where time resolved Schlieren can produce global qualitative measurements, LDI can provide point-like, quantitative measurements. This chapter discusses the use of LDI to measure a laser-induced disturbance and freestream disturbance levels and is separated into three main sections. The first two sections detail the use of an LDI system designed to measure acoustic rays emanating from turbulent structures in the boundary layer. The third section details the use of an alternative configuration of the LDI system designed to measure the laser-induced thermal disturbance region.

5.1 LDI Measurements Compared to High-Speed Pressure Transducers

To understand of how LDI responds to phenomena such as a pressure wave, it is first valuable to compare the response of the system to that of a standard instrument. To compare the response of an unsteady pressure transducer to the LDI, two Kulites were placed 50.8 mm apart along the centerline of the test section floor and a laser-induced disturbance is positioned a finite distance away from both sensors, 3 mm above the test section floor at the centerline. The LDI measurement volume is also placed 55 mm above the test section floor and 70 mm downstream of the two Kulites, shown in Figure 13. This creates an angle between the disturbance, the LDI measurement volume and the flow direction of approximately 36°, which corresponds to the expected angle of acoustic radiation in a Mach 2 flow.[12] This setup allows the pressure wave created by the laser-induced disturbance to travel outwards passing over the unsteady pressure transducers and then the LDI measurement volume in series. This setup is repeated for experiments in both quiescent air and Mach 2 flow conditions. The LDI is constructed according to configuration two as described above, in order to maximize frequency response when the experiment is carried out in Mach 2 flow.

The ensemble-averaged response of the two Kulites to the pressure wave in quiescent air is shown in Figure 25(a). By visual inspection, the response of these sensors resembles that of a second order system response to an impulse function. If the pressure wave is assumed to act as an impulse input to the sensor, then the damping ratio and natural frequency can be calculated under the assumption of a second order system model. The natural frequency and damping ratio of Kulite 1 can be calculated to be 234 kHz and 0.0784 respectively. Likewise, the characteristics of Kulite 2 can be calculated to be 320 kHz and 0.0873 respectively. These natural frequencies are in line with the < 240 kHz natural frequency that manufacturer reports for the model used in this work. The response of Kulite 2 can be seen to have a reduced amplitude when compared to Kulite 1, which can likely be attributed to the larger distance that the wave must travel to pass over the sensor resulting in a decrease in amplitude, in addition to the higher damping ratio calculated for Kulite 2.

A finite delay between the sensors' responses can be observed, and is associated with the physical distance between the sensors. Figure 25(b) shows a correlation coefficient

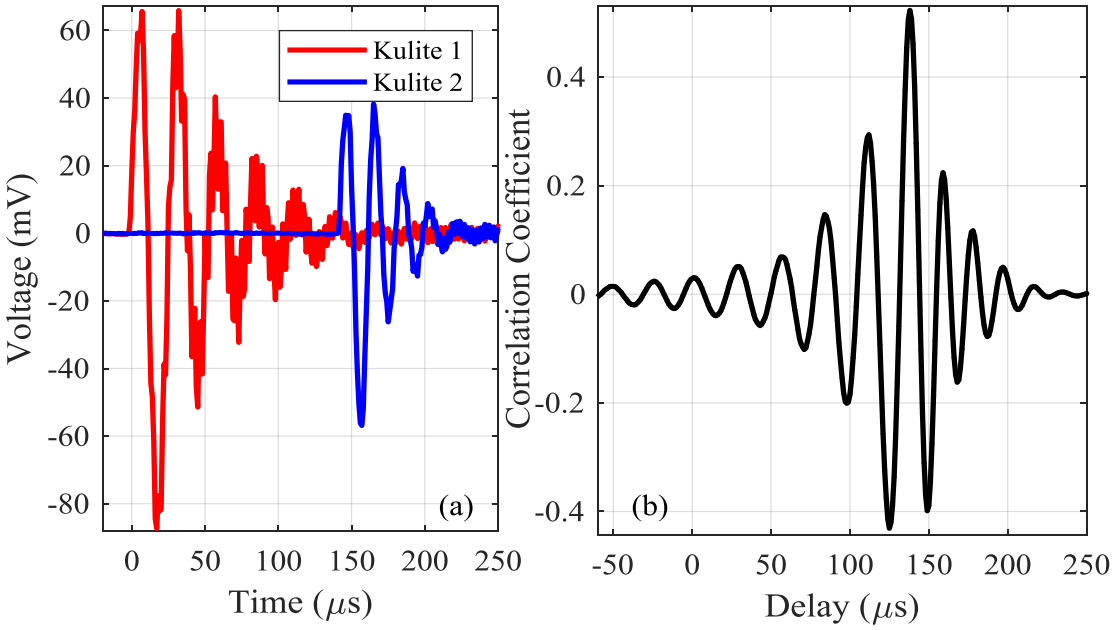

Figure 25 (a) Ensemble-averaged Kulite responses to the forced perturbation in quiescent air (b) Cross-correlation of the two Kulite's responses.

plot taken of the two signals. The dominant peak occurs at 138 μs. A quick validation of this result can be performed by measuring the wave propagation speed by using the time delay at maximum correlation and the physical spacing of the sensors. This results in a wave-speed of 368 m/s ± 20 m/s, where the uncertainty is determined by the resolution of the correlation. The Mach number of this wave can then be calculated by knowing the local speed of sound when the data was collected. The temperature was measured to be approximately 20° C which results in a local speed of sound of 343 m/s. This yields an approximate Mach number of 1.08 ± 0.06. In theory, this wave will approach a sound wave as time progresses; however, the sensors were in relatively close proximity to the origin of the pressure wave, and, the measured wave speed is approximately within the experimental uncertainty of the acoustic speed.

To compare the response of the LDI to that of the commonly used high-speed pressure transducer the LDI was placed near a high-speed pressure transducer and the laser-induced disturbance. Due to experimental concerns of noise, this set of data was band-pass filtered between 10 Hz and 100 kHz using an 8th order Butterworth filter. Figure 26 (a) shows the results of ensemble averaging 50 instances of the disturbance on the LDI and a

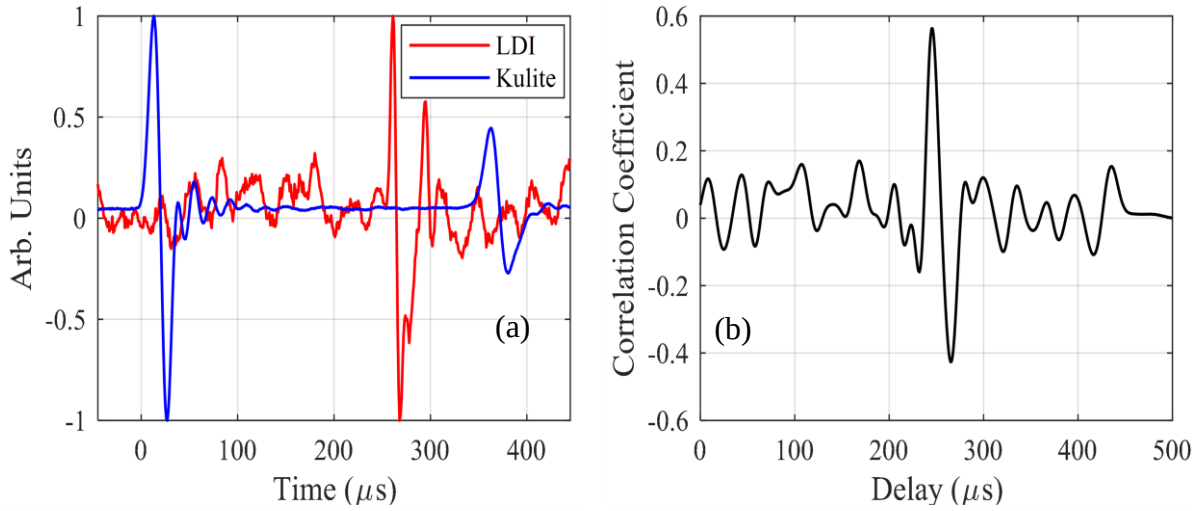

Figure 26- (a) LDI and unsteady pressure transducer response comparison (b) Cross correlation of the LDI and Kulite responses to the forced perturbation.

high-speed pressure transducer. The results have been normalized for the sake of comparison due to the differing range of the signals produced by the systems. A clear response of the disturbance can be observed on the LDI, though it is ambiguous if this conforms to a typical second order system response.

In order to verify that this response is related to the pressure wave phenomena, the wave propagation speed can again be calculated to compare to the measurement collected from the high-speed pressure transducers. Figure 26 (b) shows the cross correlation taken between the two signals as a correlation coefficient. Once again, the wave propagation speed can be calculated by taking the time delay at maximum correlation, 246 μs for this case, and the physical spacing between the sensors. This results in a wave propagation speed of 361 m/s ± 20 m/s, where the uncertainty is determined by the resolution of the correlation. When compared to the wave-speed measured using high-speed pressure transducers exclusively, this agrees well within experimental uncertainty, giving confidence that the LDI does indeed respond to the pressure wave.

Since a comparison of the LDI to an instrument system used simultaneously yields favorable results, a comparison to similar work in the literature is warranted. Figure 27

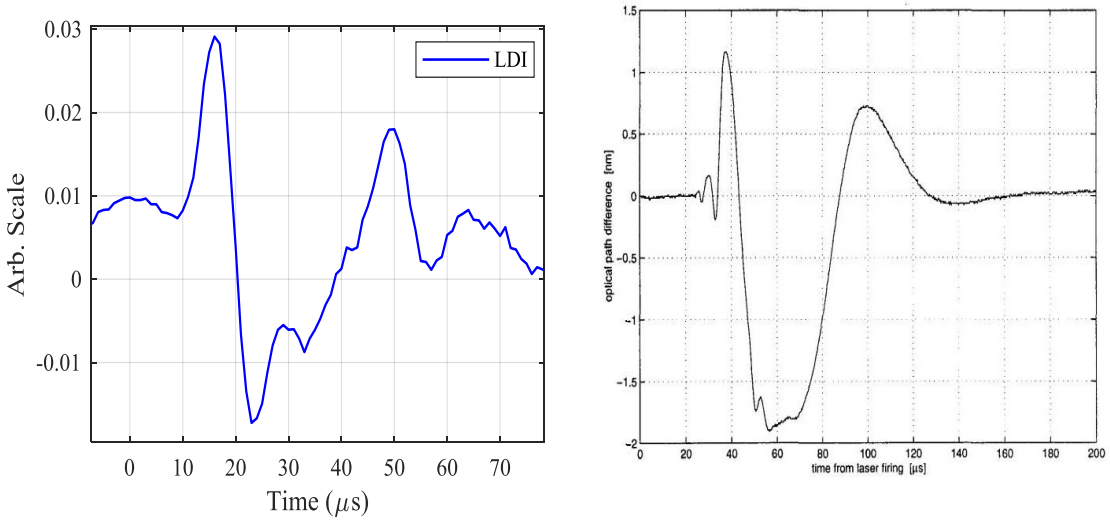

Figure 27- Comparison between the response of the present LDI (left) and similar work at Purdue by Salyer et al. (right).

shows a comparison between the current LDI system's response and that of a work done by Salyer et al.[28] In their experiment, and LDI system was set up downstream of a shockwave on a blunt-nosed body in a Mach 4 flow. A laser-induced disturbance is then positioned upstream and the thermal disturbance was propagated downstream over the LDI measurement volume. In a qualitative sense, it can be seen that these two instrument systems yielded comparable results to fluid dynamics phenomena. While the work done by Salyer et al. was performed in a Mach 4 flow, and the work shown here was performed in quiescent air, confidence can be established in the general characteristics of the systems presented.

5.2 LDI Measurements of Wind Tunnel Noise Levels

An attempt to measure the acoustic radiation that results from turbulent structures in the boundary layer of a supersonic flow was performed using the experimental configuration described in Figure 12 and Figure 13. It was hypothesized that when the laser-induced disturbance is positioned in the boundary layer of the wind tunnel wall, the resultant disturbance would generate acoustic radiation at a greater magnitude than that of radiation resulting from turbulence. For this reason, the LDI was placed in the freestream of the flow, as described in the above section. When examining the response of the LDI system to this phenomenon in the time domain, the response to the forced disturbance and free disturbances naturally occurring in the tunnel are not distinct. This may be due to the path-integrated nature of the instrument system, which will average content along its entire beam length, including the content associated with the boundary layers on the wind tunnel walls. In addition, it was determined that LDI Configuration 2, which was designed to maximize frequency bandwidth at the cost of signal amplitude, reduced the signal-to-noise ratio down to a point where drawing conclusions related to the forced disturbance were difficult. While the possibility of such results were anticipated, it was of value to carry out the experiment regardless of the response of the LDI to the forced disturbance, as freestream disturbances were clearly observed.

As stated above, while an examination of the time domain did not reveal the expected results in regards to acoustic radiation, a valuable analysis of tunnel noise is still

accessible through this experiment. Figure 28 shows the power spectral density of the LDI's response in the Mach 2 freestream compared to the signal of the LDI when completely undisturbed. Both spectra have been normalized by the variance of the background signal. a peak can be observed at 30 kHz present in both the Mach 2 measurement and the background signal. This can likely be attributed to electronic noise due to the narrow bandwidth and magnitude of the peak.

Before discussing the implications of the spectra on the fluid dynamics measured by the LDI, it is important to determine the impact of the vibrational environment generated by wind tunnel operation on the LDI measurement. In order to do this, the LDI system was used to make a measurement of Mach 2 flow, and then the system was physically moved such that the LDI beam path was outside of the tunnel flow field, but still in the immediate proximity of the wind tunnel. This was done by simply lowering the LDI optics such that the beam path passed under the wind tunnel rather than through it. The LDI was then sampled while the wind tunnel was operated, measuring the response to the vibrational environment. Figure 29 shows a comparison of the response of the LDI system when exposed to flow, and when exposed to quiescent air, where both signals are in the presence of the wind tunnel's vibrational environment. From this, it can be seen that content below 4 kHz is contaminated by vibrations, and will be ambiguous and any physical signals in this frequency range may not be distinguishable from background noise.

When examining the spectra between 4 kHz, and 100 kHz, the resulting spectra is relatively linear when plotted on a log-log scale with a slope approximately -5/3. It should be expected that the LDI will measure broadband turbulence in the tunnel since it is path-integrated over the entire length of the wind tunnel. In this sense, the slope is consistent with that of the turbulent spectra over the range of scales that an LDI system is theoretically capable of measuring.[14] An analysis of the data presented here gives confidence in the ability of LDI to optically measure the magnitude of freestream disturbances in a given facility; however, since the original objective was to measure the acoustic emission associated with a forced disturbance in the boundary layer, the small beam spacing limited the signal-to-noise ratio, and hence, the usefulness of the analysis.

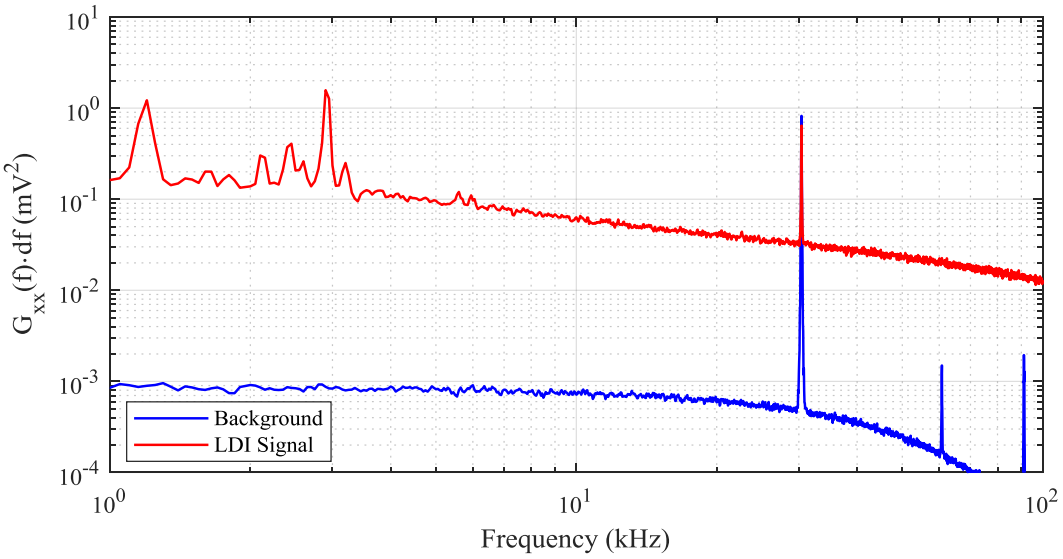

Figure 28- Power Spectral Density of the LDI system comparing the background noise levels and the frequency content present in Mach 2 flow.

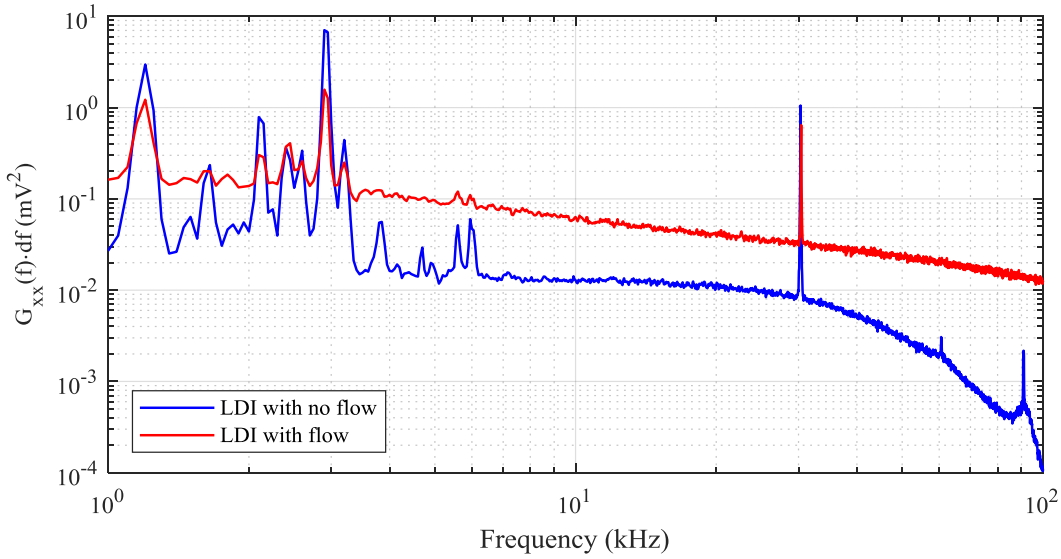

Figure 29- Power Spectral Density of the LDI system with and without flow crossing the optical path.

5.3 LDI Measurement of the Thermal Disturbance Region

The third LDI configuration, described in Table 1, is used in this section in order to maximize the response to the laser-induced disturbance. The objective was not to observe the acoustic radiation that resulted from the laser-induced disturbance when positioned into the boundary layer, but rather to observe the thermal disturbance region. In order to do this, the disturbance is injected into the freestream, 100 mm above the floor, at the same height where the LDI probe volume is located. A separation of 165 mm ± 1 mm between the LDI and the location of the laser-induced disturbance is used to allow the pressure wave to sufficiently propagate outwards, and not interfere with the measurement of the thermal disturbance itself.

An examination of the LDI's response to a pressure wave in quiescent air with the third configuration is warranted to compare to the quality of the second configuration. Figure 30 shows an ensemble history of 100 records of the pressure wave that result from the laser-induced disturbance. It can be seen that this configuration provides much cleaner

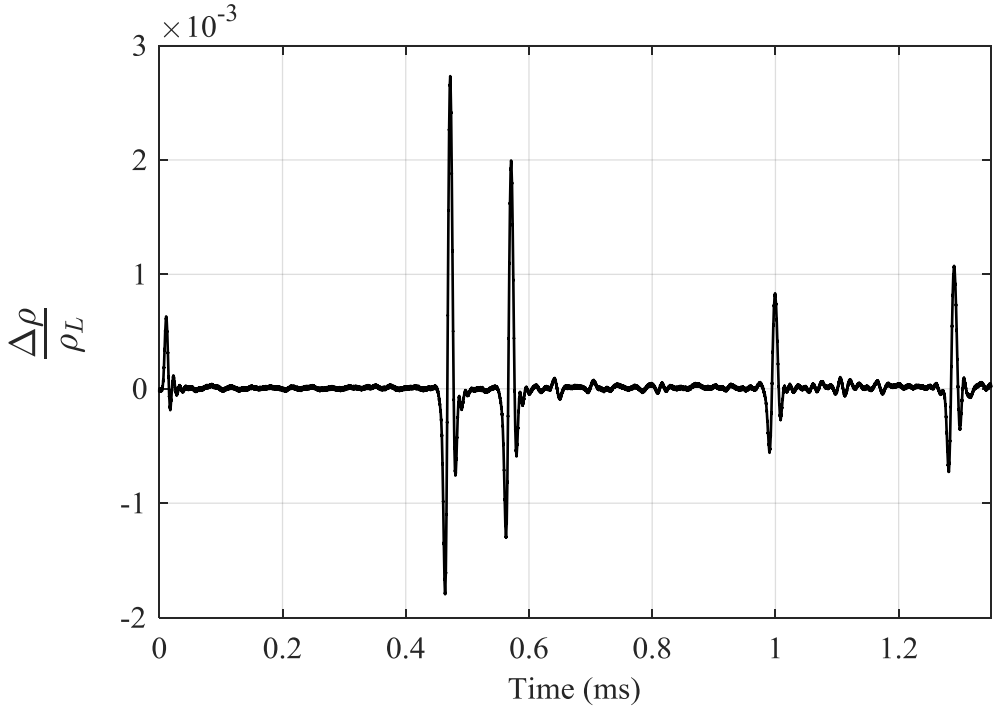

Figure 30- Ensemble-averaged time history of the LDI response to 100 pressure waves.

results with the signal-to-noise ratio exceeding 20. The peaks between 0.4 ms and 0.6 ms are the LDI's response to the initial pressure wave and the reflection off the sidewalls.The peaks at 1 ms and 1.3 ms correspond to subsequent reflections of the pressure wave off the wind tunnel walls. A small peak at 0 s corresponds to laser light scattering directly onto the photodiode of the LDI system. This demonstrates that this configuration is more appropriate to make measurements of the laser-induced disturbance in a quiescent air, and that an improved signal-to-noise ratio in quiescent air indicates a potentially improved response in Mach 2 flow as well.

Now that an understanding of the LDI system's response to the pressure wave in quiescent air has been established, an examination of the laser-induced disturbance in a Mach 2 flow is warranted with the LDI. Figure 31 shows a single response of the LDI to the Mach 2 flow with a laser-induced disturbance injected into it, compared to the signal produced from an undisturbed LDI. This shows that there is a sufficient signal-to-noise

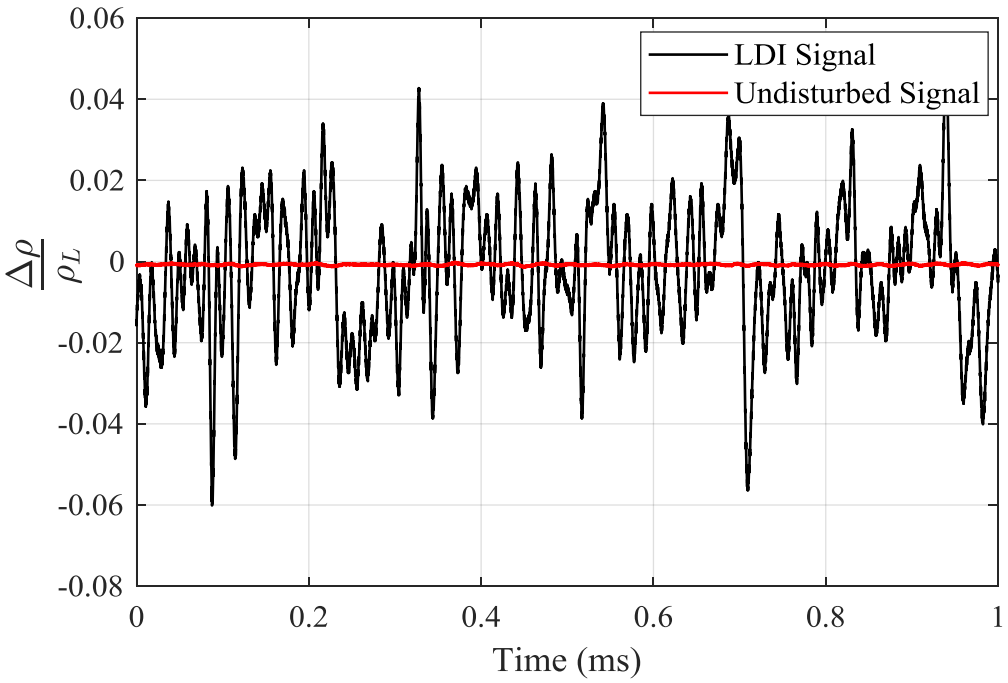

Figure 31- Time history of a respresentative data set collected with the LDI in Mach 2 Flow compared to the undisturbed LDI signal.

ratio well in excess of 20. While no indication of the forced disturbance is readily identifiable from a single time history, an ensemble average reveals more.

Figure 32 shows the results of ensemble averaging 60 records of the laser-induced disturbance in Mach 2 flow. Several features can be observed, the first at approximately 0.21 ms, the second at approximately 0.35 ms, and the third at approximately 0.7 ms. The first and third structure are similar in that they both fluctuate positively and then negatively about the mean, whereas the second structure only fluctuates positively from the mean. The fluctuation about the mean is similar to the behavior demonstrated by the LDI's response to a pressure wave in quiescent air; therefore a further investigation is warranted to determine if this is indeed the pressure wave created by the laser-induced disturbance.

A simplistic analysis of these phenomena can be performed, knowing the distance between the origin of the disturbance and the LDI, and also the delay between the laser Q-switch and the response of the LDI system. With a distance of 165 mm ± 1 mm between

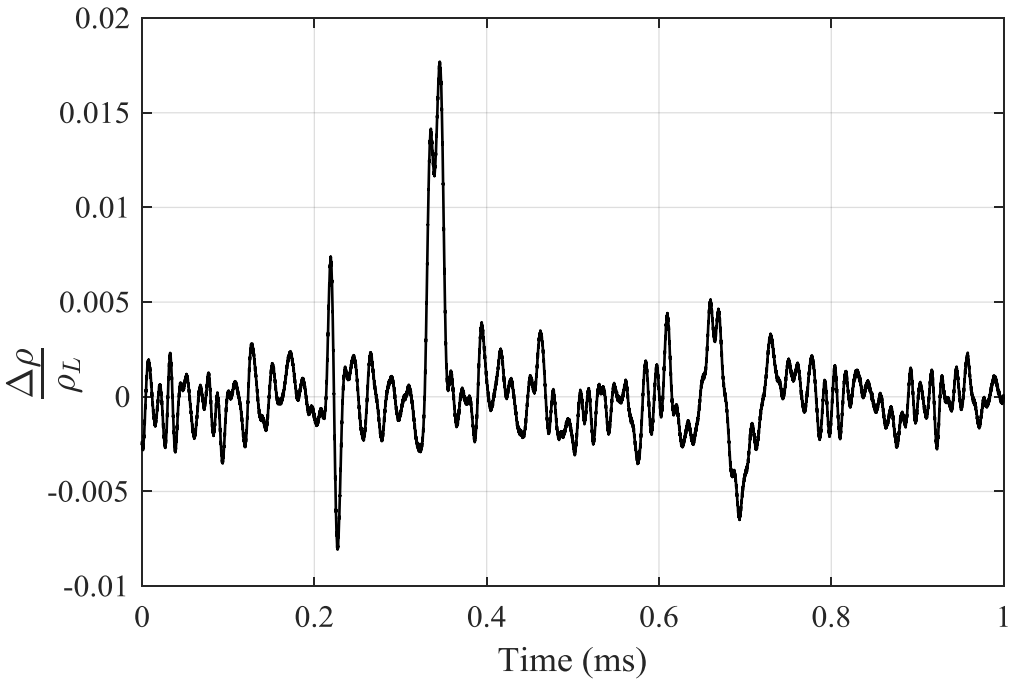

Figure 32- Ensemble-averaged time history of 60 thermal disturbances injected into Mach 2 flow, certain structures are annotated.

the LDI and the origin of the disturbance, approximate propagation speeds can be calculated. The peak of the first structure in Figure 32 occurs at 0.22 ms, which results in an approximate propagation speed of 752 m/s. The peak of the second structure occurs at 0.34 ms, and the third structure at approximately 0.66 ms. These result in approximate propagation speeds of 492 m/s and 250 m/s respectively. Based on the conditions of the tunnel, the speed of sound in the tunnel during operation can be calculated to be approximately 255 m/s. When the Mach number of the three velocities described above is calculated, they come out to approximately 3, 2, and 1 respectively. This yields some indication of what these structures are, and how this relates to the thermal disturbance that is inserted into the flow.

In theory, the pressure wave created by a laser-induced disturbance will propagate outwards and approach a sound wave with regards to wave propagation speed. When this is done in quiescent air, this results in a wave Mach number of approximately one. However, when this disturbance is injected into a flow in motion it should theoretically behave the same way *relative to* the local flow. In this particular scenario, the disturbance is injected into a Mach 2 flow, which would imply that the leading shock would propagate with an absolute Mach number of 3, likewise, the thermal disturbance with an absolute Mach number of 2, and the trailing shock with an absolute Mach number of 1. For this reason, the structures shown in Figure 32 are consistent with the leading pressure wave, the thermal disturbance, and the trailing pressure wave respectively.

With the identity of the structures determined, some detail of the physical behavior can be described, The two pressure waves show a positive, and then negative oscillation about the mean, which likely indicates the pressure wave passing over the first beam, and then passing over the second beam, resulting in a similar, yet reversed response of the system. The thermal disturbance however, only shows a region where the response of the system is elevated above the mean. This indicates a more coherent structure, larger than the size of the beam spacing. The trailing pressure wave appears “stretched out” when compared to the leading pressure wave. This may be a result of the relative velocity of the waves as they are convected through the probe volume. The leading wave is traveling faster than the local flow, whereas the trailing wave is traveling more slowly than the local flow.

This allows local turbulent structures to interact with the wave for a longer period of time, in effect breaking the wave down, or dissipating it. In addition, the circular nature of the wave-front must be considered as the wave-front will have expanded more when compared to the leading wave. As this curved wave-front passes over the measurement volume of the LDI, it will not do so uniformly producing a more elongated response from the LDI.

This investigation of the thermal disturbance with the LDI has demonstrated that the LDI is capable of rendering observations about the thermal disturbance. The overall objective is to use the LDI to determine information about the spatial frequencies and internal structures of the disturbance. In this sense, the LDI has not produced such a measurement, despite its ability to detect the disturbance. Experimental limitations and other turbulent content in the wind tunnel make such a measurement difficult for an LDI system. It is thereby recommended that such a measurement may be better suited to a focusing laser differential interferometer (FLDI). FLDI may be more capable of such a measurement since the interference between the beams is primarily the result of density gradients at the focal region of the instrument. The expanded region of the beam paths can be thought of as a spatial filter, reducing the contribution of density gradients in those regions.

In addition, it may certainly be of benefit to perform this measurement in a low speed flow, possibly subsonic, as this environment would be less noisy, and may produce a much better signal of the thermal disturbance with an LDI or an FLDI. So long as the convective speed of the flow is known with a reasonable degree of accuracy, temporal frequencies measured by the LDI can be converted to spatial frequencies, indicating the nature of the internal structure of the disturbance.

CHAPTER SIX
SCHLIEREN PERTURBATION ANALYSIS

Laser-induced plasmas produce intense temperature and pressure gradients that result in local turbulent structures, which will continue to evolve in time after the thermal plasma, has returned to an unionized state. This chapter examines the characteristics of the perturbation that results from the laser-induced plasma. Time-resolved Schlieren is used to observe the evolution and an image-based analysis provides further detail of the characteristics of these disturbances.

All Schlieren images are collected at 50 kHz and are background subtracted using the equation,

$$Processed\ Image = \frac{Raw\ Image - Dark\ Image}{Background\ Image - Dark\ Image} Gain \tag{3}$$

where the raw image is the original image taken of the perturbation, and the background image is an image of the same field of view as the raw image, but with no perturbation occurring. The dark image is an image acquired when no light was collected on the photodetector of the camera. The gain is a multiplicative factor that scales the image to best fit the range of the image display. This background subtraction produces an image that minimizes the appearance of background contaminants or imperfections on the optics used to produce the Schlieren image. In addition, each image sequence is filtered in the time domain in order to minimize the amount of background noise from one image to the next. This is done by means of an 8^{th} order digital Butterworth low-pass filter applied at 20 kHz. Since the phenomena of interest happens at frequencies far below 20 kHz, the measurements of interest are unaffected by the filter, while pixel noise is dramatically reduced. A large number of Schlieren images were collected, more than 300 image sequences of 512 images each, allowing for a statistically significant data set.

6.1 Qualitative Schlieren

It is important to have a basic understanding of the general qualities of the thermal disturbance resulting from laser-induced plasmas in order to have context on the analysis of the time-resolved images. Figure 33 shows a representative image sequence collected at

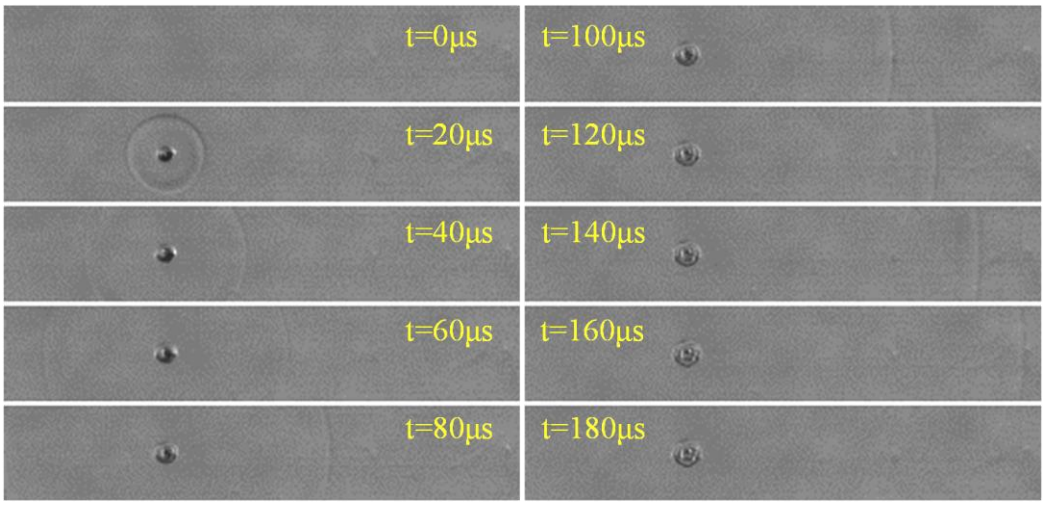

Figure 33- Schlieren image sequence of the disturbance that results from a laser-induced plasma.

50 kHz of the fluid dynamic phenomena that result from laser-induced breakdown. Two structures can be readily identified, the first is a spherical pressure wave that emanates outwards in all directions from the position of the plasma, and the second is a turbulent structure that can be seen persisting at the position of the plasma. It is important to note that the plasma itself is not present in any image; instead, what can be observed is exclusively the resultant fluid motion caused by the plasma's transient presence.

A qualitative understanding of the physics can be derived from an analysis of this image sequence. When laser-induced breakdown occurs, the plasma causes intense local heating, which results in a rapid expansion of the local fluid, creating a compression wave that emanates outward spherically. The local heating results in temperature and density gradients in the immediate vicinity of the plasma, which then expand and mix with the surrounding, cooler fluid. This results in instabilities that cause the structure to break down and evolve as it reaches thermodynamic equilibrium with the surrounding fluid. Due to the local heating, this structure is often referred to as a thermal disturbance, or "hot-spot." Figure 34 shows the evolution of the turbulent structures in a typical hotspot. From a qualitative analysis, it can be seen that a two-dimensional cross-section of the disturbance

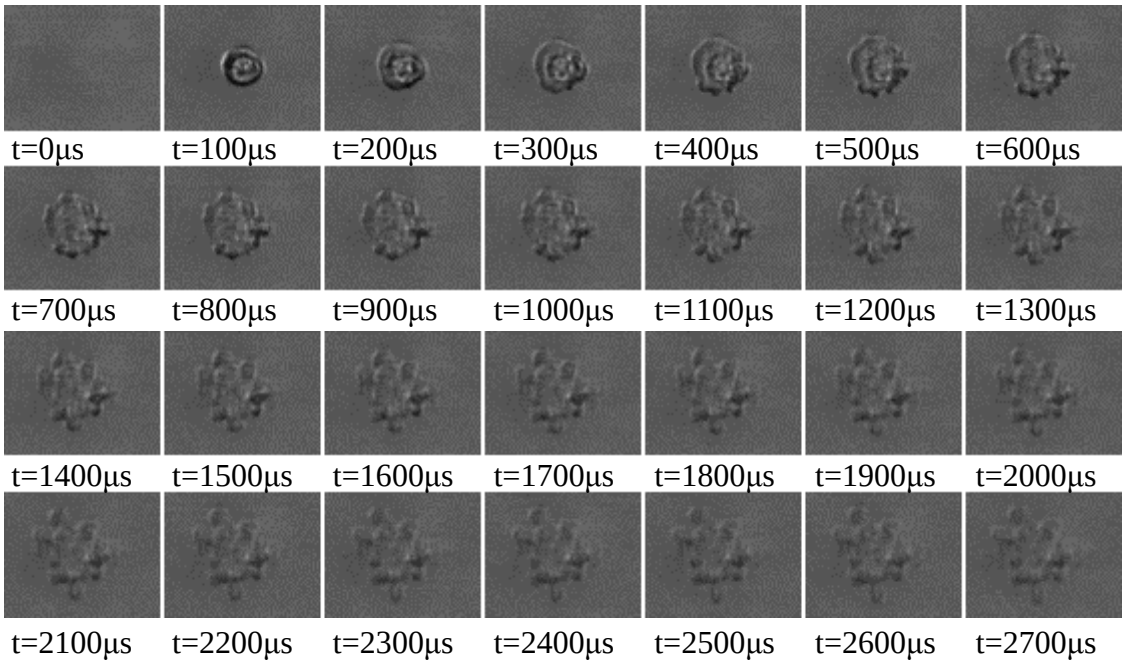

Figure 34 - Schlieren image sequence of the evolution of the turbulent structures in the thermal disturbance.

begins relatively circular in nature, and propagates uniformly for the first 200-300 μs. After 300 μs, it can be seen that the overall coherent structure begins to break down into smaller structures as the disturbance continues to expand and evolve. This qualitative analysis of the evolution of the structure provides some insight into how to further investigate the characteristics of this forced disturbance.

It can be seen that the overall thermal disturbance has some characteristic growth rate as the structure expands outwards and evolves. Turbulent structures can also be observed, and an analysis of the evolution of these structures can be performed. Furthermore, a relationship, if any, between the overall growth rate, and the evolution of the internal turbulent length scales can be examined. While a general trend is apparent, variations between sequential thermal disturbances have been observed. Figure 35 shows the variations that occur between sequential disturbances. All of these images were taken at 440 μs, 3 ms, and 10 ms after the Q-Switch of the laser, respectively. The intensity of

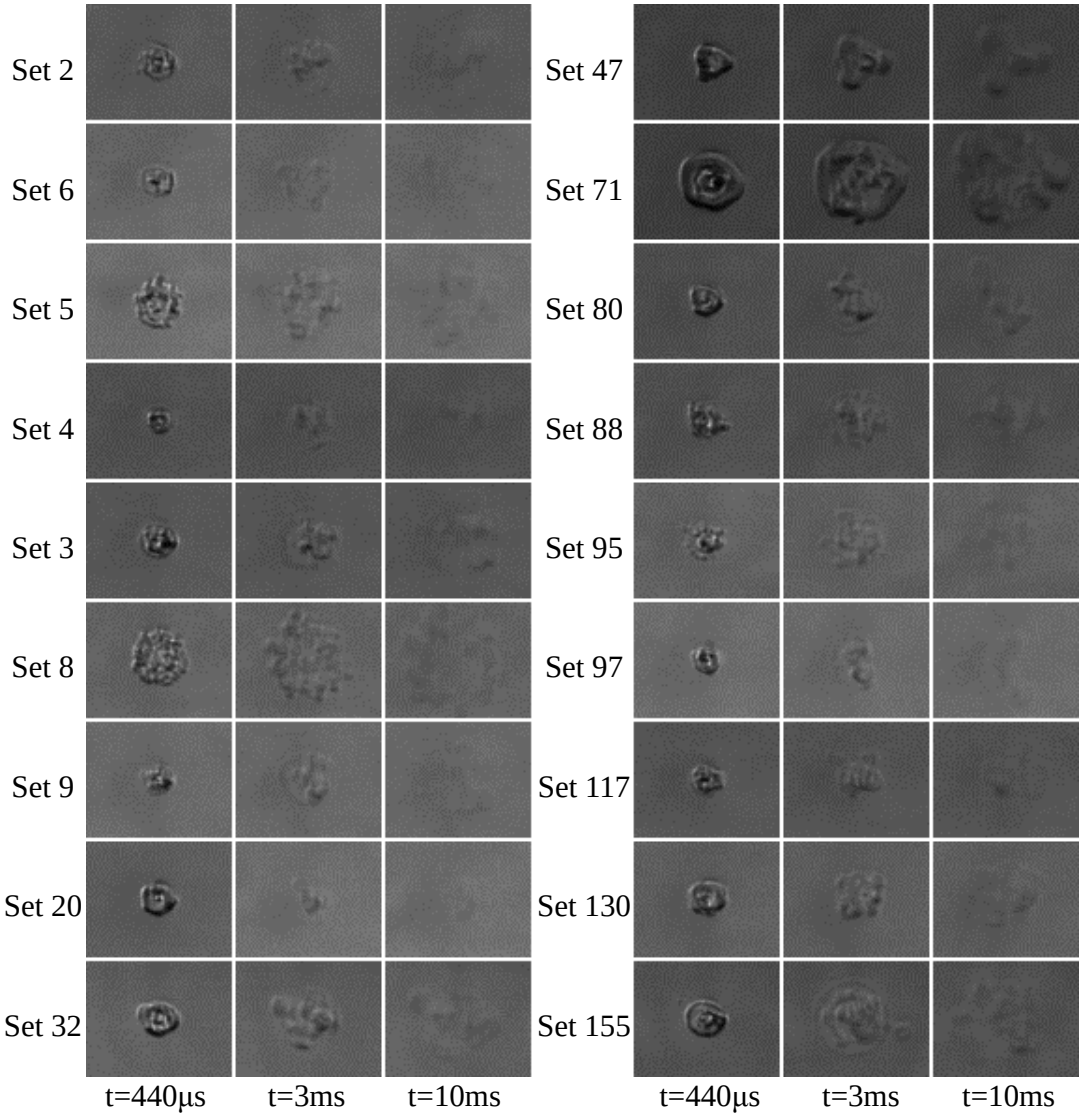

Figure 35- A comparison of a random sampling of typical disturbances at the same time delay from the laser Q-switch.

each image was scaled in order to maximize the contrast. Inherent variations in the state of the turbulence can be observed; however, there is also non-trivial variation of the size of the disturbance and the amount of turbulent content present. While much variation can be observed, Figure 36 shows an ensemble average of the disturbance where mean structures can be observed. The following two sections present a statistical analysis of the growth of the disturbance and the turbulent spatial frequencies in order to present a more comprehensive understanding of these disturbances.

6.2 Growth Rate and Large Scale Structure

In order to determine the overall size of the disturbance, it is assumed that a two-dimensional cross-section of the disturbance is in general circular in nature, though Figure 34 and Figure 35 show that the disturbance is not necessarily radially symmetric, a circular model presents a simplistic way to measure how the size of the disturbance changes in time. A MATLAB script is used to detect the edges of the disturbance, and a circle is fit to the edges of the disturbance. This process produces a robust measurement of the disturbance that can be applied to a large data set of these image sequences, even if there is significant variation in the growth rate and initial size of the thermal hotspot. Images

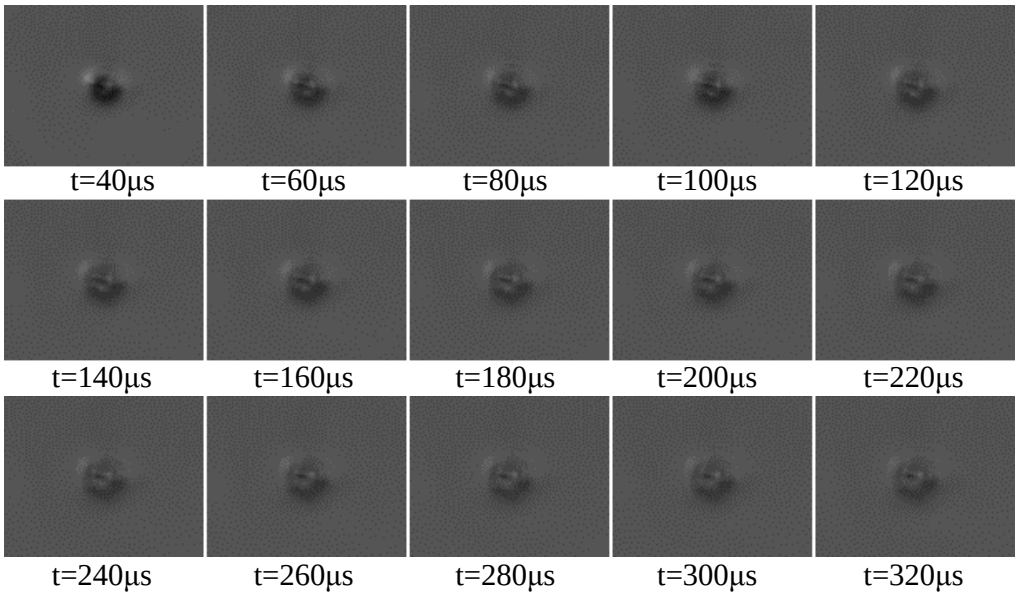

Figure 36- Ensemble average of 180 disturbances in quiescent air.

from 40 μs to 3000 μs delay from the Q-switch was found to be sufficient in order to fit a curve to the growth rate, where images after 3000 μs may have dissipated significantly, producing an ambiguous measurement of the diameter. A window of 96 x 120 pixels was found to be sufficient to resolve the size of the disturbance over this time, with a physical resolution of 5.9 pixels/mm, which provides a physical window of approximately 16 mm x 20 mm. The laser energy used to generate these disturbances is fixed at 120 mJ/pulse.

Figure 37 shows the growth rate for a typical thermal disturbance where an uncertainty of 1 pixel has been applied. A curve fit has been applied to it through a least squares regression, and a function of the form,

$$D = a * t^b \tag{4}$$

which has been found to represent the general behavior of the growth of the disturbance. D is the diameter of the disturbance in meters, t is the time in seconds, and a and b are the curve-fitting coefficients. It is of interest to note that the growth rate is highly non-linear, characterized by an initial, large expansion, after which the growth slows down, which was found to be characteristic of all data collected. In this model it is assumed that the disturbance size is 0 m at t = 0 s, which can be seen to be a reasonable assumption as the plasma dynamics that occur within the nanoseconds after the laser pulse lie outside the

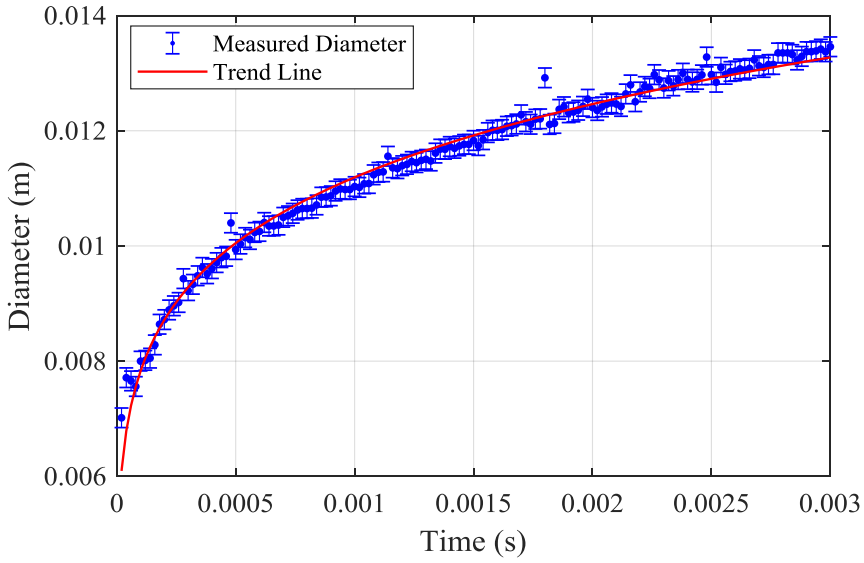

Figure 37- Growth of a typical disturbance in time.

scope of this work, but has been examined by other researchers.[27] Furthermore, a true measurement of the disturbance size at $t = 0$ s using time-resolved Schlieren would encounter experimental difficulties as the size of the disturbance would require sub micrometer camera resolution, and the pressure wave may still obscure the structure of the thermal disturbance. This one case is representative of the general trend of the size of these disturbances as a function of time; however, the actual values of the curve-fitting parameters *a* and *b* vary for different disturbances. In order to develop a statistical model, 300 individual thermal disturbances were imaged and their measured size was fitted using Eq (4).

Table 3 shows a selection of related curve-fitting parameters, including the goodness-of-fit estimate and the root-mean-square-error (RMSE). All curve fits considered have an r^2 value greater than 0.8, where a large majority have a value greater than 0.95. While r^2 is a quantitative indicator of goodness-of-fit, the root-mean-square-error may be a more appropriate measurement of the curve-fitting process. This shows that the diameter measurements in general are a reasonable estimate of the physical size of the disturbance.

Figure 38 and Figure 39 show the distributions of the values of curve-fitting parameters *a* and *b*. A kernel-smoothing estimate with 100 kernels has been used to generate a smooth probability density function of the probability densities, while the actual densities have been shown with bars. Parameter *a* has a mean value of 0.0271 and a standard deviation of 0.0125. Parameter *a* is clearly skewed right, with a skewness value of 1.04 and a kurtosis value of 4.21. This indicates a heavy tail behavior to the right of the mean, which can clearly be seen. Because the standard deviation is 46% of the mean value, and the distribution is highly skewed, a Gaussian distribution is not a reasonable fit for parameter *a*. This also indicates that some physical phenomena drives the thermal disturbance to be larger under the right conditions. By visual inspection, parameter *b* appears to be more Gaussian. The mean value of *b* is calculated to be 0.171 with a standard deviation of 0.0511. The skewness of *b* is calculated to be 0.214, indicating a slight bias to the right of the mean. The kurtosis of *b* is calculated to be 2.86, indicating light tail behavior. In general, parameter *b* can be modelled as a Gaussian distribution

Table 3- Curve-fitting values for select disturbances.

Sequence #	***a***	***b***	**r^2**	**RMSE**	**Size (mm) at 3 ms**
3	0.0327	0.155	0.987	0.000176	13.3
9	0.0513	0.198	0.971	0.000384	16.3
35	0.0254	0.142	0.972	0.000200	11.0
40	0.0330	0.188	0.975	0.000233	11.1
46	0.0292	0.219	0.855	0.000482	8.2
53	0.0278	0.191	0.905	0.000380	9.2
62	0.0737	0.2733	0.9765	0.000373	15.1
66	0.0234	0.1662	0.992	0.000093	8.9
77	0.0564	0.2146	0.969	0.000415	16.2
83	0.0324	0.1605	0.947	0.000344	12.7
89	0.0329	0.1681	0.929	0.000323	12.4
100	0.0346	0.222	0.967	0.000220	9.5
104	0.0272	0.141	0.944	0.000304	12.0
111	0.0325	0.1717	0.880	0.000556	12.0
124	0.0178	0.133	0.967	0.000132	8.2
137	0.0267	0.200	0.928	0.000310	8.4
157	0.0247	0.166	0.943	0.000275	9.4
164	0.0337	0.172	0.997	0.000075	12.4
175	0.0533	0.259	0.941	0.000476	11.8
182	0.0270	0.159	0.984	0.000156	10.7
194	0.0150	0.0975	0.896	0.000228	8.5
210	0.0392	0.176	0.960	0.000358	14.2
222	0.251	0.161	0.975	0.000187	9.8
235	0.0491	0.272	0.948	0.000389	10.1
241	0.012	0.131	0.913	0.000166	5.6
250	0.0129	0.125	0.946	0.000130	6.2
262	0.0257	0.176	0.968	0.000211	9.3
270	0.0269	0.195	0.977	0.000177	8.7
276	0.0155	0.138	0.870	0.000376	7.4
294	0.0253	0.177	0.942	0.000281	9.1
300	0.0460	0.211	0.987	0.000223	13.5

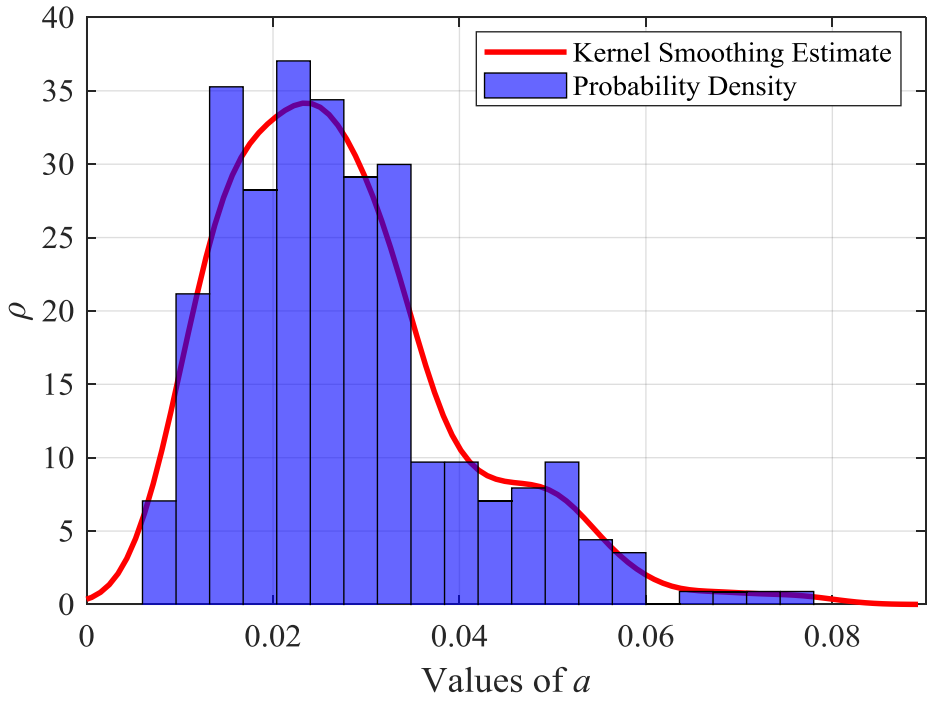

Figure 38- Kernel-smoothing estimate of the probability density of parameter *a*.

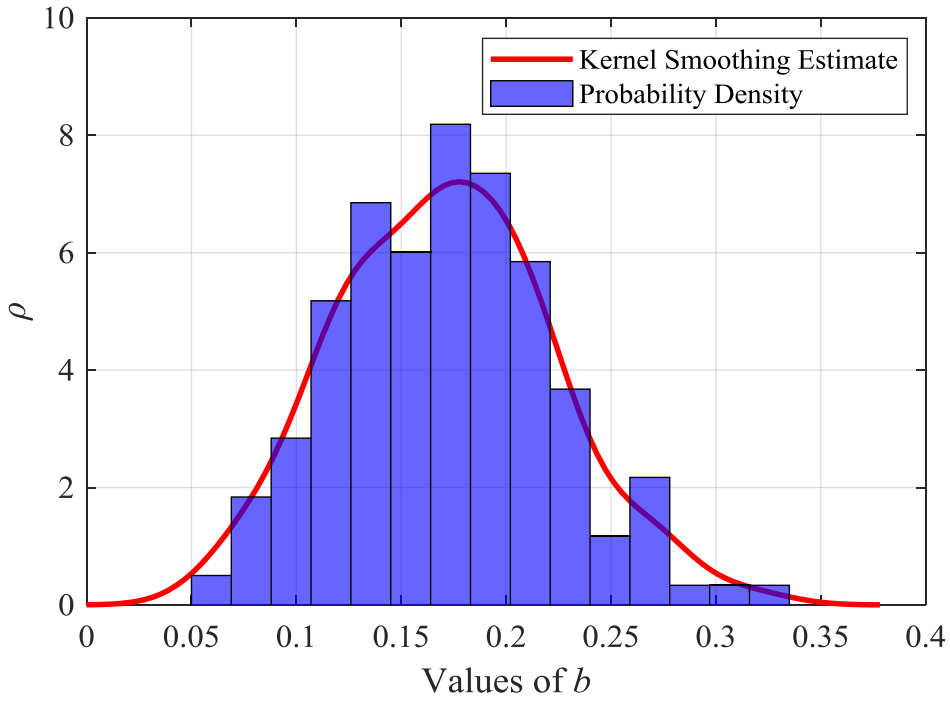

Figure 39- Kernel-smoothing estimate of the probability density of parameter *b*.

based on the statistics presented here. In order to validate that 300 data sets were sufficient to have statistical significance, a residual analysis is performed with the equation,

$$R_i = \left| \frac{\overline{x_i} - \overline{x_{i-1}}}{\overline{x_n}} \right| \tag{5}$$

where for a set of n values, R_i is the residual of the i^{th} in the data set, $\overline{x_i}$ is the mean of the i^{th} values, $\overline{x_{i-1}}$ is the mean of the i^{th}*-1* values, and $\overline{x_n}$ is the mean of n values. In this analysis the i^{th} entry refers to the image sequence of an individual disturbance for which the growth rate was measured. Figure 40 shows the mean residuals for parameters *a* and *b*, and demonstrates that 300 samples are sufficient to be representative of the statistics of a larger set, as the residual has converged to approximately 10^{-3}.

In order to understand how the size of the disturbance as a function of time varies from one disturbance to another, Figure 41 shows a waterfall plot of the kernel-smoothing probability density function of the sizes of the disturbance at any given instance in time. Using Eq. (3) and the curve-fitting parameters *a* and *b* determined above, a better understanding in how the statistical variation of the base parameters affects the disturbance

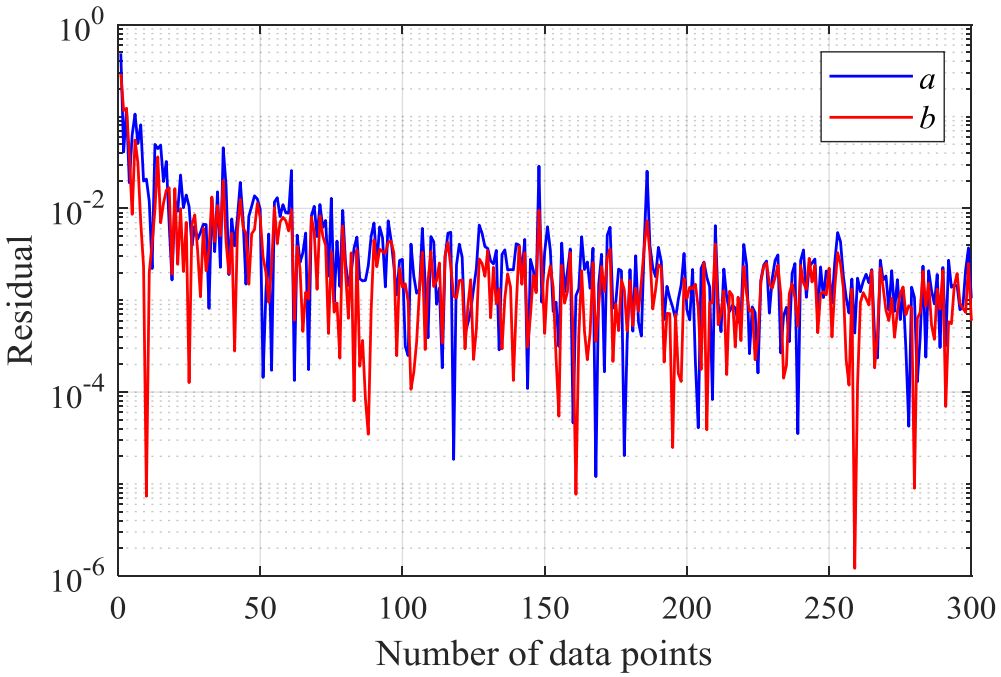

Figure 40- Residual of the curve-fitting parameters for 300 data points.

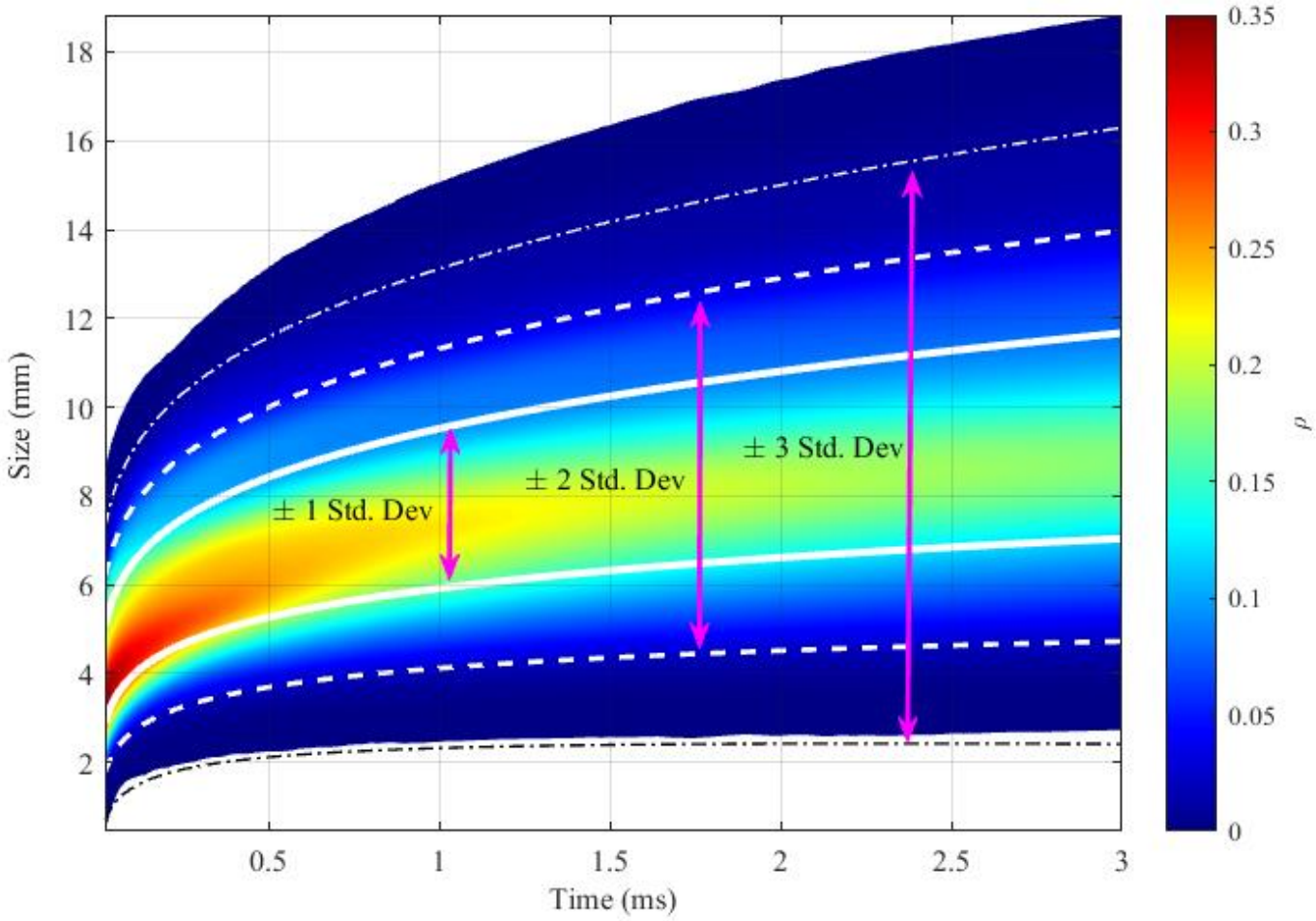

Figure 41- Distribution of the size of a thermal disturbance advancing in time.

can be determined. The mean diameter of the disturbances increase with time, along with the range of diameters observed. This broadening of the distribution of sizes as a function of time is due mostly to the variations in the *b* parameter of the function, which is influenced by the rate of growth. The *a* parameter more directly reflects the initial size of the disturbance, which is apparent when examining the shape of the distribution in Figure 38 and Figure 39.

The underlying physics of what drives this may be somewhat complex; however, a simplistic understanding of it can be derived from the heat transfer that occurs. The temperature and density gradients present in the immediate aftermath of the plasma dissipation (nanosecond timescale) can be assumed to be proportional to the amount of energy deposited from the laser in the local air. These temperature and density gradients would result in an expansion that drives the locally heated fluid outwards. This would result in an outward momentum that drives the overall diameter of the disturbance to continue to grow at a rate proportional to the original size of the disturbance when the plasma is present. This relies on the assumption that the size of the disturbance in the first image acquired in these time-resolved Schlieren image sequences are also proportional to the size of the plasma. It then follows variations in the plasma may directly result in differing gradients and likewise, varying characteristics of the evolution of the disturbance.

6.3 Internal Turbulence and Spatial Frequencies

Time-resolved Schlieren Provides a unique opportunity to examine a large field of view of flow phenomena when compared to other measurement techniques. In order to better understand the evolution of the internal structures in a forced perturbation, time-resolved Schlieren is used to examine the characteristic spatial frequencies. In order to perform this analysis, cropped Schlieren images of the forced perturbation are analyzed by examining the intensity of each individual pixel and treating it as a sensor. Spectral analysis can reveal what frequency content is present in a given thermal disturbance. Figure 42 shows the Power Spectral Density of the spatial frequencies in a single instance of the thermal disturbance compared to the background noise level, and the PSD has been normalized by the variance of the background signal. All PSD's presented in this work

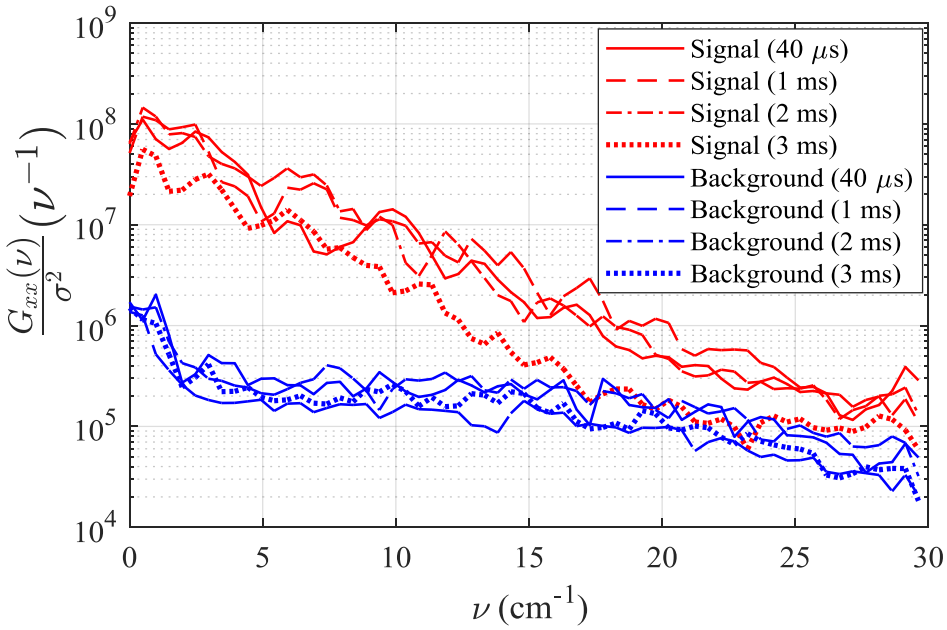

Figure 42 - Spatial spectra of the thermal disturbance at various times compared to the background noise level, normalized by the background variance.

used the Welch method of power spectral densities,[53] with a Hann window equal to the size of the image (e.g. 120 pixels) and no overlap. Using the size of each disturbance that was measured in section 6.2, only rows and columns that contained some portion of the disturbance are used for the PSD analysis, in order to maximize the sensitivity of the PSD. Several representative instances in time have been plotted to show that the PSD of the disturbance yields frequency content throughout the lifetime of the disturbance. The background noise level can be seen to be relatively constant in time, and the background spectra presented here are representative of the background levels in all instances of the thermal disturbance. The spectra associated with the thermal disturbance appear to decay at later time steps, in contrast to the time-invariant behavior in the background noise.

In order to better understand how the spatial frequencies of the disturbance vary in time, contour plots will be used in order to better demonstrate the continuity of the temporal evolution. Background levels will not be presented in order to better visualize the signal. Figure 43 shows a color map of the PSD intensities evolving in time for a typical instance of the spark, and Figure 44 shows ensemble average spectra of 300 disturbances. Several

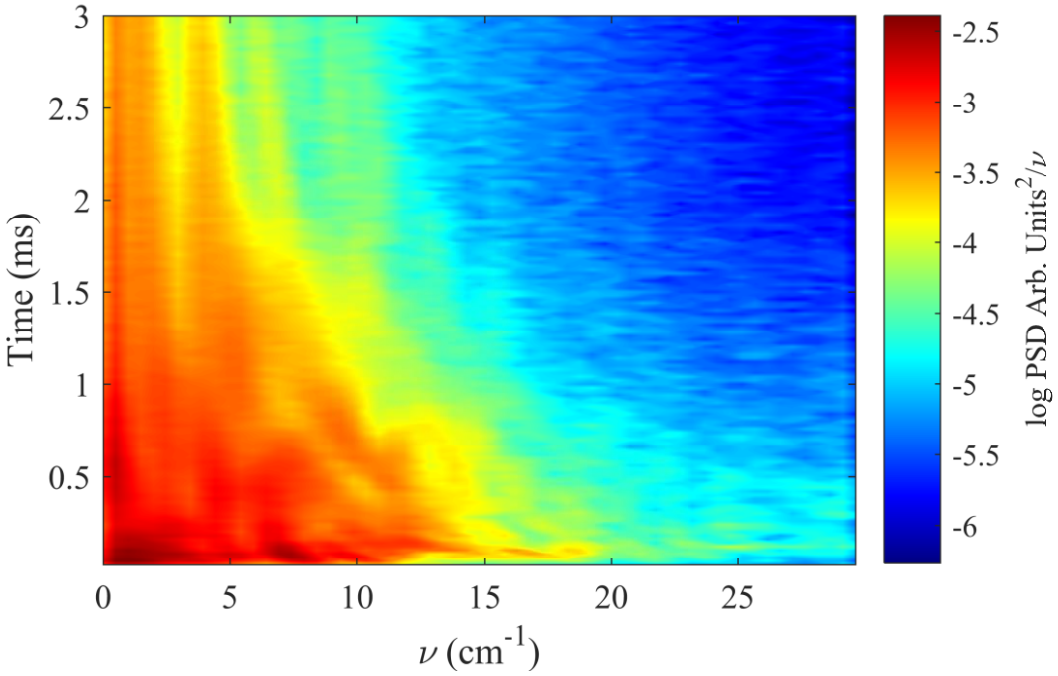

Figure 43- Colormap of the PSD of an individual thermal disturbance advancing in time.

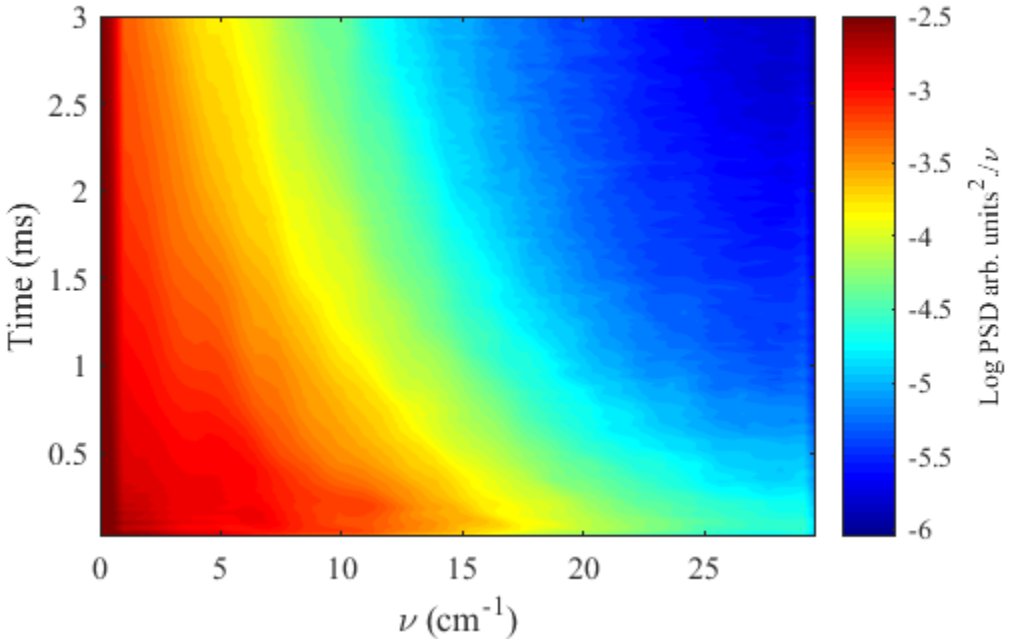

Figure 44- Spectra of the mean disturbance behavior advancing in time.

interesting characteristics can be observed from these plots. In general, the bandwidth of content present decreases towards low frequency content as time evolves. During the first ~100 μs, an evolution of higher frequency content can be observed, preceding the general bandwidth narrowing trend. This seems to indicate that instabilities in the temperature and density gradients form in the first ~100 μs, causing a breakdown of the overall coherent structure into smaller, turbulent structures, associated with higher frequency content. This process is then followed by dissipation of the newly formed turbulent structures, which continues to occur for several milliseconds before the disturbance dissipates altogether.

In a general sense, the plasma that creates this disturbance can be thought of as an impulse function relative to the fluid dynamic time scale. This impulse will heat the local gas and cause it to expand. This process creates an outward momentum, and as the locally heated packet of fluid expands outwards, instabilities form and break the structure down into turbulence. After the formation of this turbulence, dissipation will take over as the dominant mechanism. Since the plasma will have dissipated on the nanosecond timescale, no driving force persists, leaving the fluid structures to tend towards an equilibrium state. As the size of these turbulent structures grow, the spatial frequency content associated with them will decrease.

Since such variation was present in the disturbances, analysis of the spatial frequencies of the disturbance may benefit from an analysis of a non-dimensionalized spectra. Using the size of the disturbances measured in section 6.2, the spatial frequencies can be normalized by the size of the disturbance at any given instant in time to determine what, if any, relationship exists between the overall disturbance size, and the internal turbulence. Figure 45 shows a comparison between three individual spectra in both dimensional and non-dimensional form. The frequency is expressed as a non-dimensional frequency in terms of the number of oscillations per diameter (shown on the right). Several interesting characteristics can be observed through these comparisons. Within the first 250 μs, peaks can be observed shifting into the higher frequency range in the non-dimensional cases. The bandwidth of content then becomes more constant in time, while decaying in intensity. While some bandwidth narrowing can still be observed, the general trend is that the bandwidth of content becomes invariant in time.

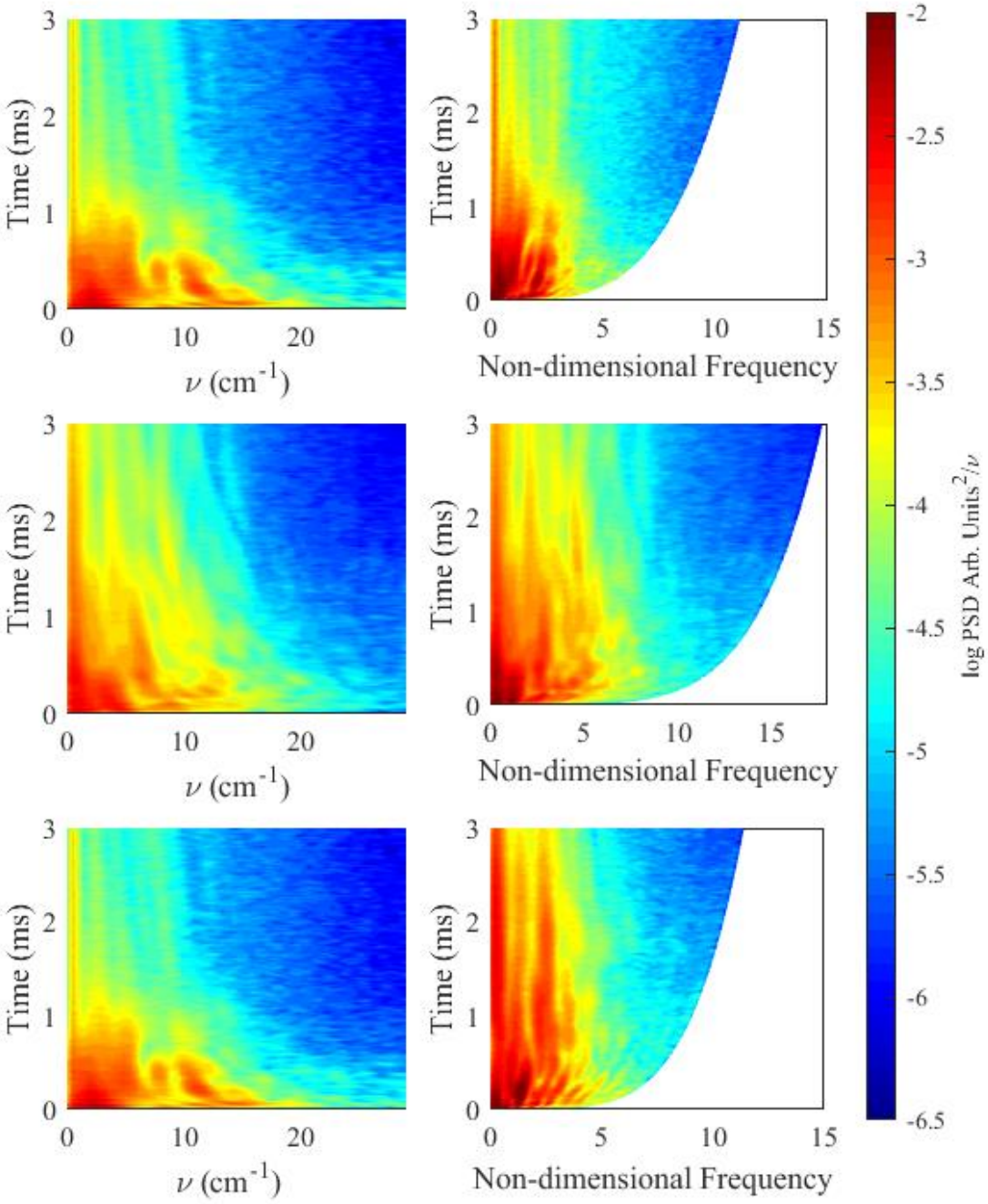

Figure 45- A comparison of several spectra in dimensional and non-dimensional form, normalized by the instantaneous disturbance diameter.

When examining the spectra expressed in dimensional frequency, the bandwidth of content can be seen to narrow as previously discussed. In a physical sense, this demonstrates that the evolution of turbulent scales typically occurs within the first millisecond, after which, the turbulent length scales then become proportional to the diameter of the disturbance at that instant in time. While some variation in this behavior can be observed, the general trend shows that dissipation becomes the dominant mechanism as time progresses, and the turbulent structures simply expand and tend towards equilibrium.

In order to determine if the relationship between the diameter of the disturbance and the turbulent length scale is characteristic of all data collected, the mean spectra will be examined and normalized by the mean diameter of the disturbance at that instant in time. Figure 44 shows the mean spectra of all disturbances as a function of time. This shows the same general trend as Figure 43, and Figure 45, that frequency content in the disturbance decays in magnitude and bandwidth as time progresses. This is highly indicative that dissipation is the dominant mechanism on the millisecond time scale.

6.4 Evolution of a Thermal Disturbance in Supersonic Flow

Quiescent air provides a still environment in which to characterize the natural evolution of a laser-induced perturbation; however, laser-induced perturbations are often used in fluids in motion. As such, a characterization of the behaviors associated with laser-induced disturbances in Mach 2 flow will be presented in order to better understand how the evolution of the disturbance progresses in a convection flow field. Figure 46 shows a time resolved Schlieren image sequence taken in the Mach 2 tunnel. All Schlieren footage captured in the Mach 2 tunnel was collected at 50 kHz, and the laser-induced disturbance was generated at the same physical location as in the quiescent air analysis in order to facilitate comparisons.

Measurements made by the LDI were found to be capable of responding to the pressure wave and the thermal disturbance in Mach 2 flow, and a comparison to the Schlieren images will provide some validation. Knowing the physical resolution of the image, the convective speeds of the pressure wave and the disturbance can be measured

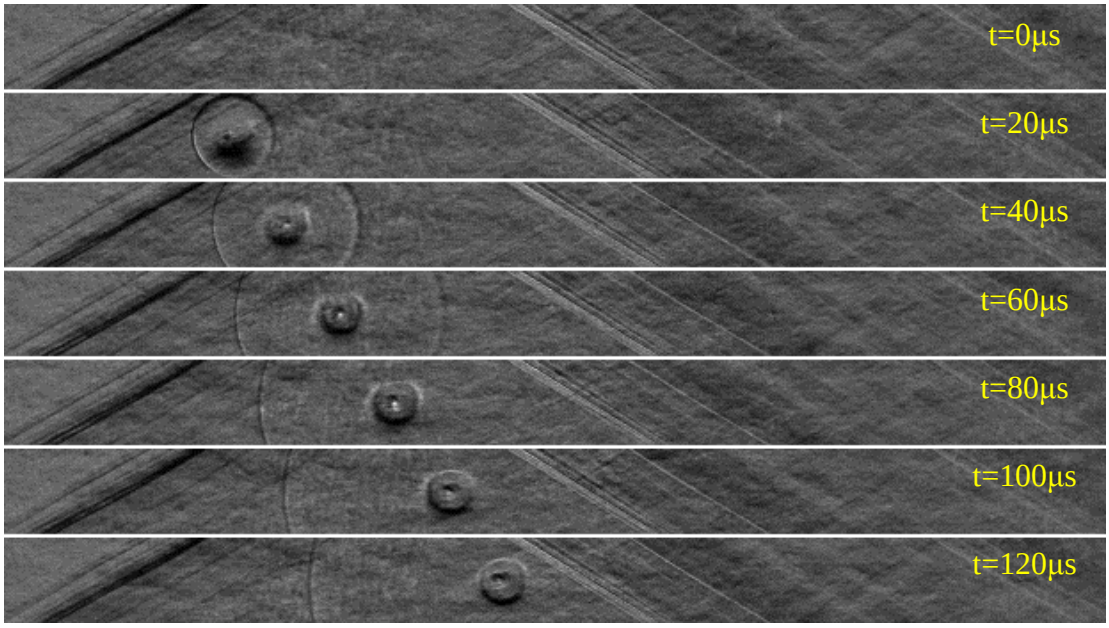

Figure 46- Schlieren time sequence of the thermal disturbance propagating in a Mach 2 flow.

and compared to the LDI measurements discussed previously. The leading pressure wave can be measured to propagate at approximately 766 m/s ± 30 m/s, where the uncertainty in velocity is determined by a 2 pixel uncertainty in the measurement. The thermal disturbance can be measured to propagate at approximately 510 m/s ± 30 m/s, and the trailing pressure wave can be observed to propagate at approximately 260 m/s ± 30 m/s. Based on tunnel operating conditions, the speed of sound can be calculated to be 255.7 m/s, from which, Mach numbers can be determined for these propagating structures. Since the pressure wave will theoretically propagate throughout the flow at a Mach number of 1 *relative to* the local flow, that will result in motion of the trailing pressure wave at an absolute Mach number of 1, the leading pressure wave at an absolute Mach number of 3, and the thermal disturbance at an absolute Mach number of 2. This results in a theoretical velocity of 255.7 m/s, 511.4 m/s and 767.1 m/s for the trailing pressure wave, thermal disturbance and leading pressure wave respectively. This agrees with the measurements made by the LDI system in Figure 32.

Using a simple MATLAB script, the disturbance can be examined in a Lagrangian frame of reference, which will aid comparison between the quiescent air case and the Mach 2 case. Figure 47 shows an individual instance of the disturbance. The disturbance can only be observed for the first 320 μs as it will propagate out of the field of view after this time has elapsed. This image sequence is fairly representative of all footage acquired in Mach 2 flow. Two concentric structures can be observed for approximately the first 200 μs. In a three-dimensional sense, this is indicative of the disturbance's toroidal nature, which has been discussed by previous literature.[25,26] Figure 48 shows an ensemble average of 180 image sequences of the thermal disturbance injected into Mach 2 flow, where this toroidal shape is the mean behavior of the disturbance. It is also interesting to note that the mean disturbance diameter is larger than the quiescent air case when compared to Figure 36. This may be attributed to the lower density, temperature, and pressure environment into which the disturbance is introduced, which would result in a more rapid expansion, and hence a larger diameter, which will be discussed in detail later.

Figure 49 shows variations between various disturbances, all collected at 40μs, 140 μs, and 280 μs respectively. When compared to Figure 35, it can be seen that there is less variation in diameter from one disturbance to the next, and that the concentric structures appear to be present in most disturbances. This may be due to the lower density environment, as well as experimental factors that may have limited the consistency of the plasma creation in the quiescent air case.

The key difference that can be observed between the Mach 2 case and the quiescent air case is the broad shift in the diameter of the disturbance. While more variation occurs in the quiescent air case, it is very like that experimental considerations played some role in the variations that were observed. One of the characteristics that can be observed to be common between the Mach 2 case and the quiescent air case is the presence of a void in the center of the disturbance. This feature is related to three-dimensional effects, in which the disturbance evolves in a toroidal shape, rather than a uniform sphere. In addition, both cases show a mean growth as time evolves and the evolution of turbulent content.

A limited statistical analysis of the disturbance growth rate is presented, as the turbulent nature of the flow present in the image is prohibitive to the type of algorithmic

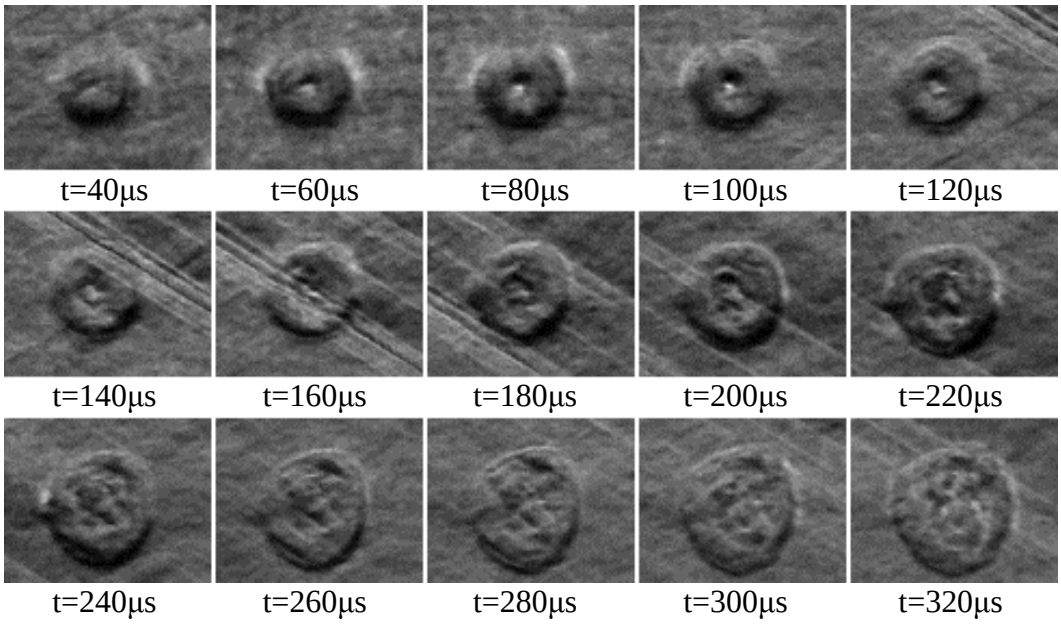

Figure 47- Schlieren time sequence of a Lagrangian reference from of the disturbance in Mach 2 flow.

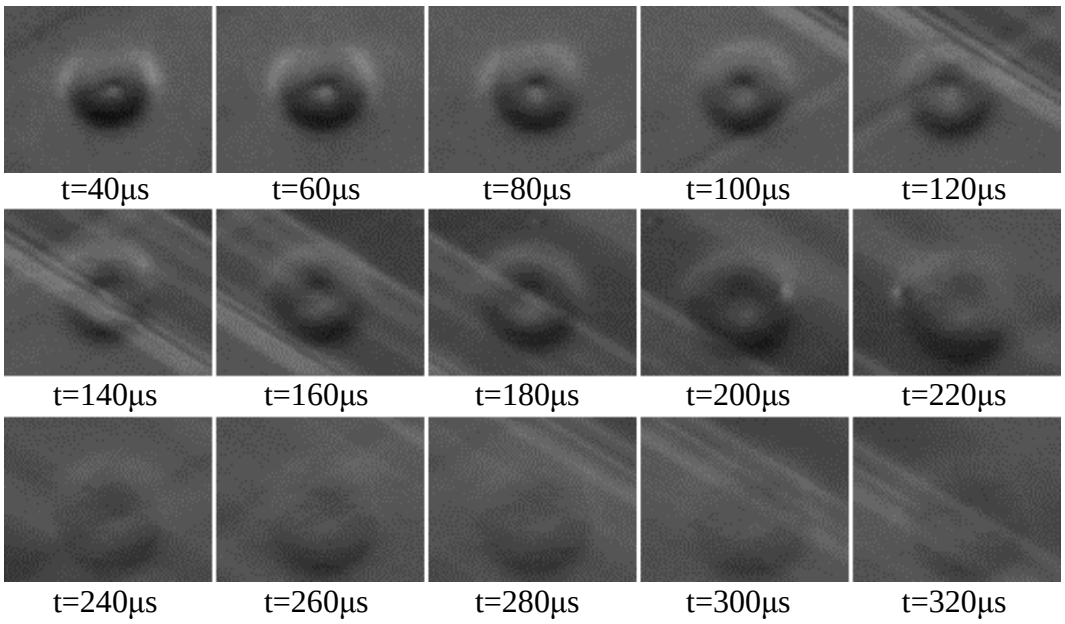

Figure 48- Lagrangian view ensemble average of 180 instances of the thermal disturbance in Mach 2 flow.

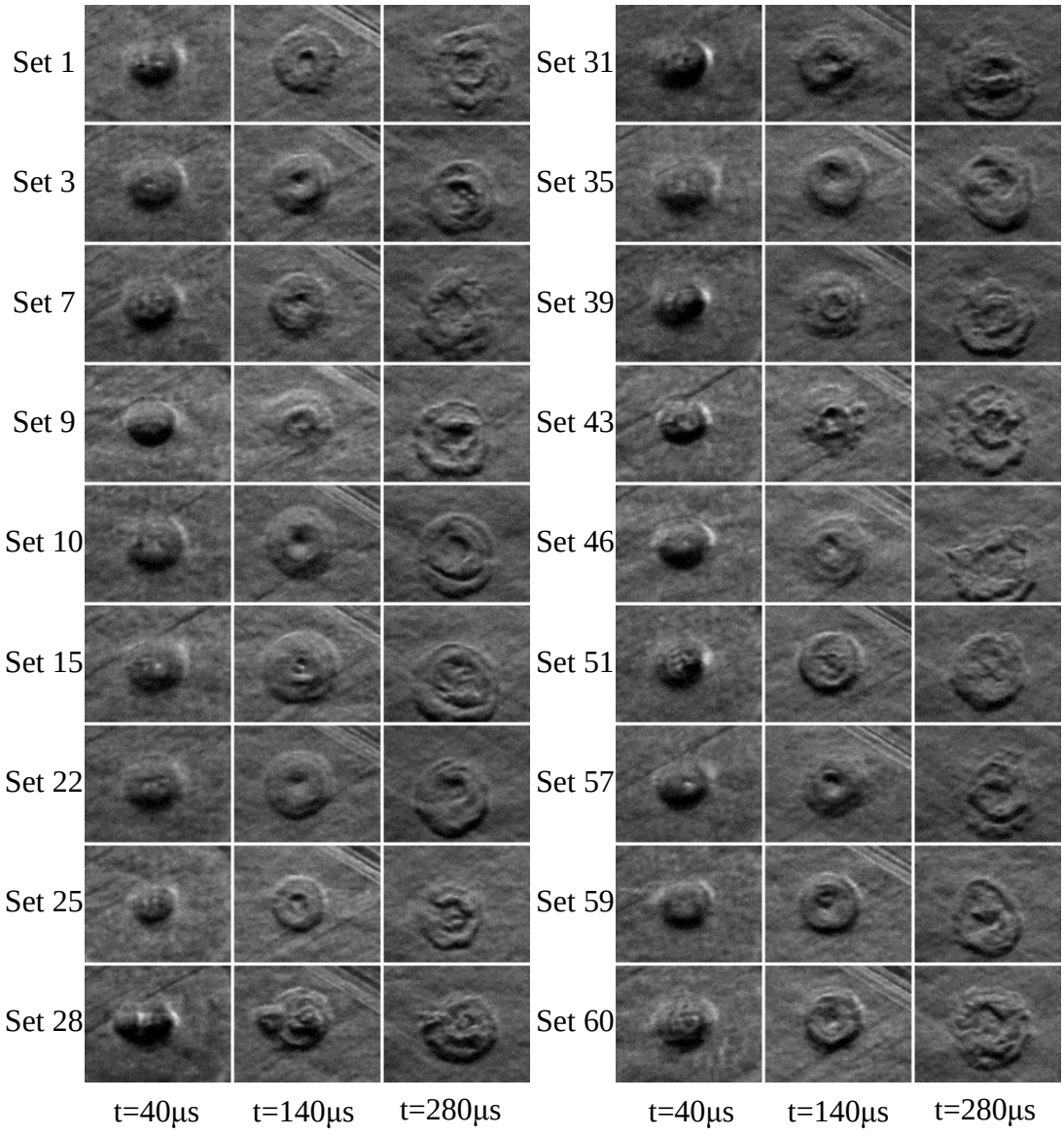

Figure 49- A random selection of disturbances all imaged at the same time.

analysis used in the quiescent air case. Weak shockwaves present in the image interfere with the detection of the disturbance edge. A background subtraction of these shockwaves is also difficult as the waves shiver, and may move slightly, limiting the application of such a technique. As such, a frame-by-frame analysis is performed instead. A typical disturbance growth rate and trend line of the form of Eq (4) is presented in Figure 50 (where a ±2 pixel uncertainty is assumed.) A limited time history of the disturbance growth is shown due to the finite time that the disturbance is present in the field of view in a Mach 2 flow. Despite this limited history, a similar trend in the growth of the disturbance can be observed when compared to the growth rate in quiescent air shown in Figure 37.

When a frame-by-frame analysis is performed on 50 disturbances in Mach 2 flow, a general trend can be observed. The curve-fitting parameter *a* has a mean of 0.0465 and a standard deviation of 0.0174. The skewness is calculated to be 0.897, indicating a slight bias to the right of the mean, and the kurtosis is calculated to be 3.53, indicating a slight

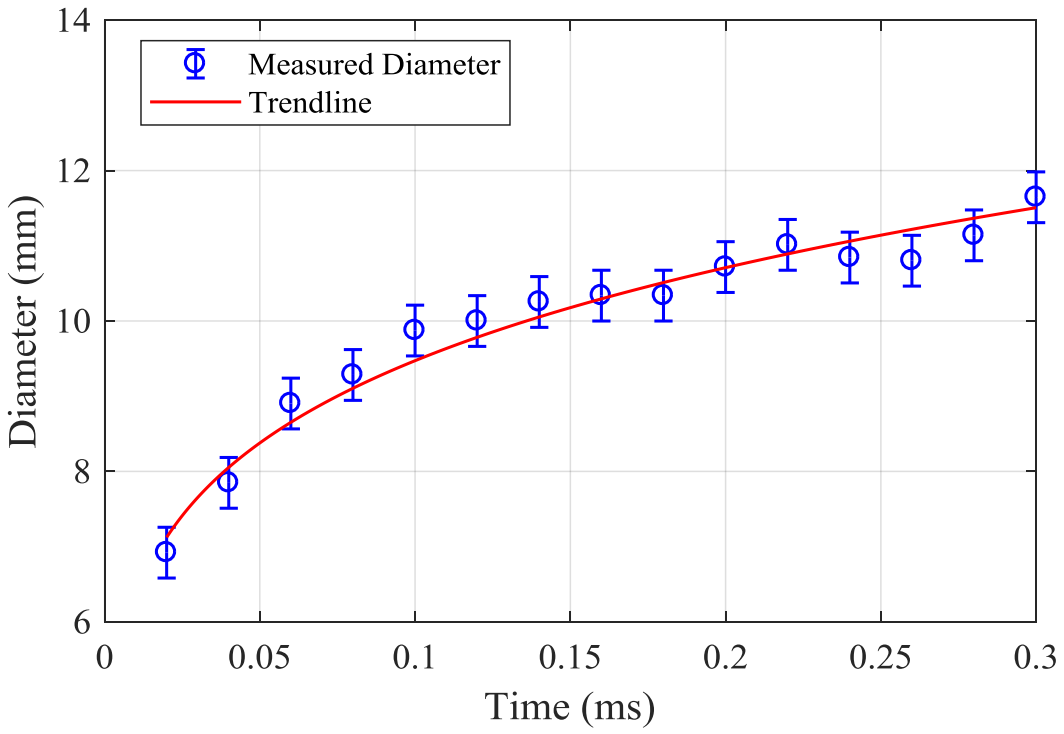

Figure 50- Representative growth rate of the disturbance in Mach 2 flow.

tail-favoring behavior. Curve-fitting parameter *b* has a mean value of 0.167 and a standard deviation of 0.0387. The skewness and kurtosis are calculated to be 0.289 and 2.24, respectively, indicating a mean favoring behavior with a slight bias to the right of the mean. Figure 51 shows a comparison of the probability density function of the curve-fitting parameters when the disturbance is generated in quiescent air and Mach 2 flow. The general shape of the distributions in quiescent air and Mach 2 flow is similar, though *a* can be seen to have a larger standard deviation in the Mach 2 case. It is also interesting to note that the mean of *a* is significantly larger in a Mach 2 flow when compared to quiescent air, being 71% larger for Mach 2 flow than quiescent air. The percent increase of the mean of curve-fitting parameter *b* for the quiescent air case and Mach 2 case is only 2.33%. This shows that the rate of growth is relatively unaffected by the density of the local environment into which it is introduced; however, the scale of the disturbance largely depends on the local conditions.

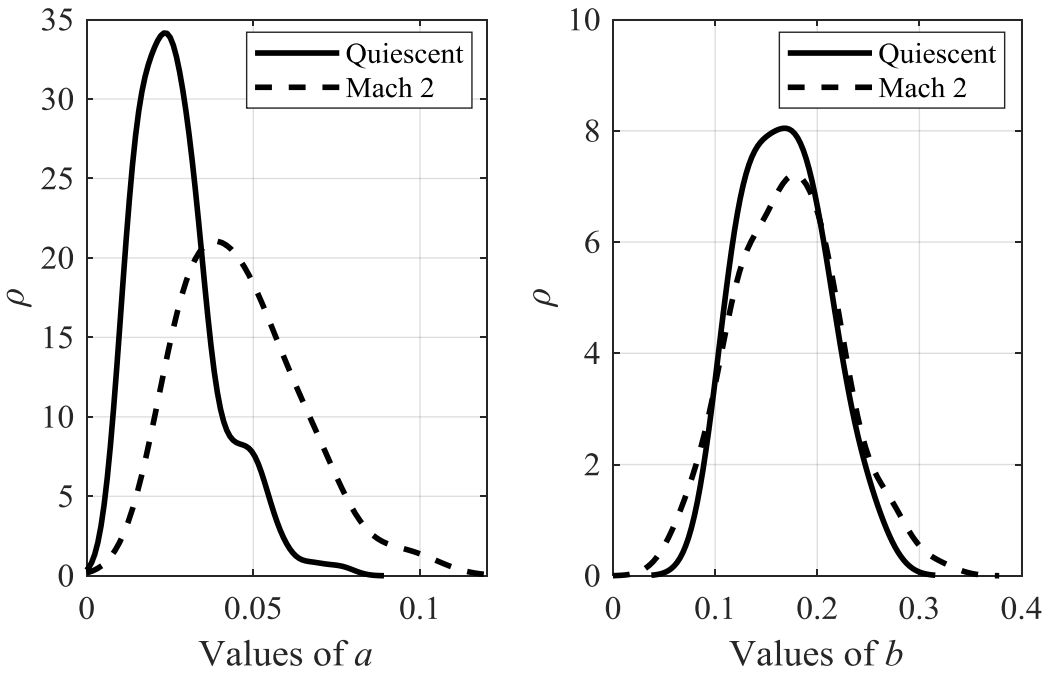

Figure 51- a comparison of the probability densities of the curve-fitting parameters in quiescent air and Mach 2 flow.

Figure 52 shows the probability densities of the disturbance diameter over its observable lifetime in Mach 2 flow. Here it is shown that there is clearly a positive shift in the mean diameter of the disturbance when compared to the quiescent air case. This is likely tied to the *a* curve-fitting parameter, which influences the scale of disturbance. The rate of growth of the disturbance seems to remain relatively unaffected. In order to better understand the similarities of the turbulent structures present in the Mach 2 and quiescent air cases, Figure 53 shows the spectra of the thermal disturbance in a Lagrangian frame of reference in Mach 2 flow. Due to the convection of the disturbance, a shorter time history is presented as the image propagates out of the field of view, limiting the extent of the analysis that can be performed as a function of time. One particular feature of interest occurs between 0.1 ms and 0.15 ms, where the bandwidth of the spectra expands. This feature is not physical, but rather associated with the weak shocks present in the field of view at those times, shown in Figure 47. Beyond this, the spectra presented do not

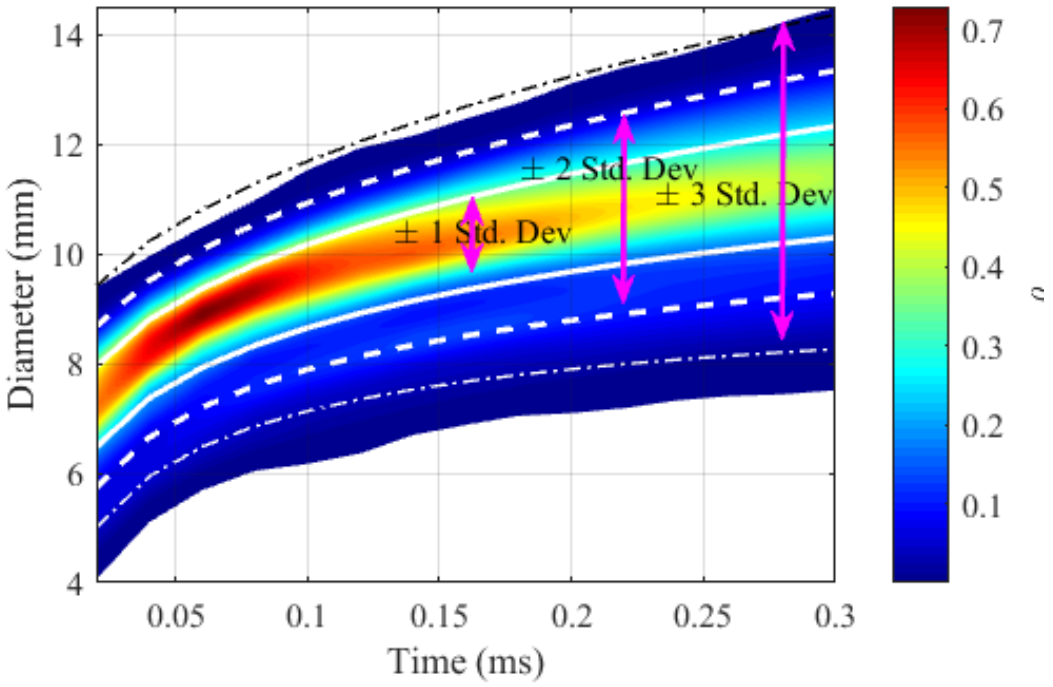

Figure 52-Probability densities of the diameter of the disturbance in Mach 2 flow.

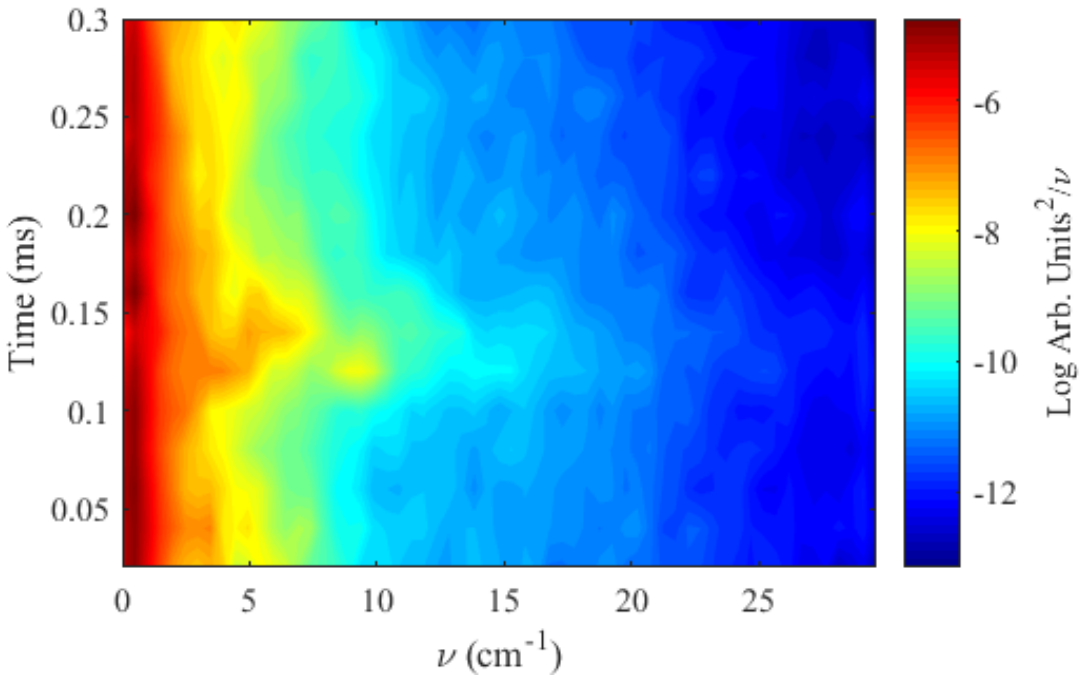

Figure 53- Spectra of the spatial frequencies of the disturbance in a Lagrangian frame of reference.

demonstrate the features, such as bandwidth narrowing, and the evolution of turbulence shown in previous spectra. This is likely due to the limited time history that can be examined, and the presence of other turbulent structures in the flow unassociated with the thermal disturbance that may affect the PSD analysis non-trivially. Some level of bandwidth narrowing can be seen; however, a sufficient time history cannot be observed to determine the evolution of the disturbance on a millisecond scale, limiting the definitive conclusions that can be drawn from this data.

CHAPTER SEVEN
CONCLUSIONS

This work provides an analysis of the capabilities of two optical techniques, laser differential interferometry (LDI) and time-resolved Schlieren, and their ability to make measurements of laser-induced disturbances, and freestream disturbance levels in a Mach supersonic flow. In the pursuit of doing so, the LDI is calibrated in a benchtop setting to give proper context to the measurements in supersonic flow.

7.1 Laser Differential Interferometry

The LDI was calibrated on a free jet at varying diameters and stagnation pressures, and was found to be able to measure dynamic content out to approximately 120 kHz. For a 4.3-mm diameter jet at a stagnation pressure of 170 kPa, turbulent content can be observed out to 110-kHz, and frequency content is found to roll off with radial and axial distance. For a 4.3-mm diameter jet at 136-kPa stagnation pressure, frequency content can be observed out to approximately 60 kHz, where the same trend of frequency roll off is observed in the radial and axial directions. For a 12.7-mm diameter jet at 103-kPa stagnation pressure, frequency content can be observed out to approximately 30 kHz; and once more, the same trend of frequency roll off is observed in the radial and axial directions.

The jet profiles that are obtained at varying stagnation pressures, jet diameters, and axial locations are observed to be highly self-similar. The spreading rate of the jets are measured to be approximately 0.097, which agrees with other measurements of free jet spreading rates reported in the literature,[51,52] and the spreading rates measured were found to be independent of Reynolds number. This calibration provides confidence in the ability of the LDI presented in this work for unique applications as it is capable of credible measurements of a canonical experiment, that has been repeated often in the literature.

The LDI is then used to observe the pressure wave that results from a laser-induced disturbance, and its response is compared to that of a high-speed pressure transducer's response. The LDI is found to properly respond to the pressure wave, and compares favorably with the results reported by other researchers. The LDI is then used to measure

the acoustic radiation that results from the injection of a laser-induced disturbance into a turbulent Mach 2 boundary layer. The LDI did not provide data that could detect any phenomena that could clearly be identified as acoustic radiation. This is in part attributed to the configuration of the LDI used, which resulted in a low amplitude signal, and hence a low signal-to-noise ratio. In addition, the path-integrated nature of the instrument may have contributed to the obfuscation of the measurement.

LDI is then used to make measurements of the thermal disturbance resulting from a laser-induced disturbance in a Mach 2 flow. The configuration used allowed for the observation of the thermal disturbance in a mean sense. Ensemble averaging allows a clear analysis of the disturbance, though instantaneous measurements revealed little of interest.

7.2 Schlieren

Schlieren was used to make quantitative measurements of a laser-induced disturbance in quiescent air. In a three dimensional sense the disturbance is toroidal, although when observing along the laser-axis a two-dimensional, circular cross-section is observed. The thermal disturbance is typically found to endure for 10 ms, after which, the disturbance may be too diffuse to be observed. The majority of fluid dynamic phenomena of interest occur within the first 3 ms of the disturbance's lifetime, after which, diffusion continues until the disturbance reaches thermodynamic equilibrium with the surrounding fluid. The overall diameter of the disturbance is found to grow in a highly non-linear fashion, where the diameter of the disturbance can be modelled as $D = a * t^b$. For a dataset of 300 individual occurrences of the thermal disturbance, the mean growth rate in quiescent air is found to be $D = 0.0271 * t^{0.171}$, though non-trivial variation in these curve-fitting parameters is observed. This variation may have been due to experimental factors as well as variations in the local fluid conditions and variations in the laser power.

The internal spatial frequencies of the disturbance can be observed to evolve in time. Typically, the disturbance remains circular in nature for the first 100 μs, after which instabilities in the structure break down into turbulence. Turbulent structures can evolve for the next 300 μs - 400 μs of the disturbance's lifetime, afterwards diffusion becomes the dominant mechanism, and already existing structures continue to expand outwards.

Internal spatial frequencies can be observed to range from 7 - 15 cm^{-1} in the first 500 μs of the disturbance's lifetime, but tend to decay below 5 cm^{-1} in the ms timescale. This bandwidth, narrowing as a function of time, is likely the result of the dominance of diffusion later in the disturbance lifetime. When these spatial frequencies are normalized by the instantaneous diameter of the disturbance, the spatial frequencies tend towards time invariance, and the majority of spatial frequency happens at a non-dimensional frequency of less than 5.

An understanding of the physics that drive these observations can be determined through consideration of the plasma formation and the resultant, intense heating of the local gas. After the plasma dissipates, a large temperature and density gradient exists at the position of the now-cooled plasma. This results in a transfer of momentum that pushes the fluid structures outwards. Instabilities form, and break down into turbulence; however, in the absence of a continuous driving force, the evolution of turbulent structures can be thought of as a transient event. Following formation, the residual momentum drives the existing structures outwards at a continually decreasing rate. This results in the power-law like behavior in the growth rate of the disturbance.

Similar conclusions can be drawn when the laser-induced disturbance is injected into a Mach 2 flow; however, due to the relative motion of the flow field and the limited field of view, a time history beyond approximately 320 μs cannot be presented. A two-dimensional cross-section of the disturbance is observed to be relatively uniform and circular for the first 100 μs of its lifetime, after which the evolution of turbulent structures can be observed. The disturbance is still observed to grow in a non-linear fashion, according to the equation, $D = 0.0465 * t^{0.167}$.

Here, the mean value of curve-fitting parameter a is 71% larger than the quiescent air case, resulting in a positive shift of the mean diameter of the disturbance. This is likely due to the lower pressure and density environment in which the disturbance is present. This allows for an expansion to a larger size in the same amount of time as the quiescent case. Less variation in the disturbance growth rate and size are observed from one disturbance to the next, which may be in part due to experimental factors or the low density environment. Overall, studying a laser-induced disturbance in quiescent air is in general

representative of the time dependent dynamics of the internal turbulence found in a disturbance present in Mach 2 flow. Spatially, it should be noted that the disturbance will be larger in a lower density environment.

7.3 Suggestions for Future Work

Throughout the course of this work, several opportunities for improvement were identified. This section details potential ways to improve the currently existing work, and provide a more holistic understanding of thermal disturbances.

A properly configured LDI system was found to be able to make measurements of the thermal disturbance, and the pressure wave created by a laser-induced disturbance; however, observing the thermal disturbance with the LDI required the disturbance to convect over the stationary LDI measurement volume at some known convective speed. The decision was made in this work to observe the disturbance in a Mach 2 flow since the facility had readily available optical access and its convective speed was known. Turbulence in the Mach 2 flow obfuscated instantaneous measurements of the thermal disturbance with the LDI, and a more consistent measurement may be obtained through repeating this experiment in a low-speed environment where the turbulent structures interfere with the measurement to a lesser degree.

Additionally, LDI is a path-integrated technique, averaging content along the entire length of its beam pair. Focusing laser differential interferometry (FLDI) is a similar instrument system that limits this path-integrated effect, essentially spatially filtering dynamic content in regions of lesser interest. The application of this technique may be highly valuable to this work, as the disturbance takes up a relatively small volume compared to the test cell used in this work.

Some variation in the Schlieren images of the laser-induced disturbance raise questions regarding amount of energy that the laser was depositing into the local fluid from pulse to pulse. While the mean laser energy was measured before every test, instantaneous measurements of the laser energy were not taken during the experiment. Future efforts may make use of some measurement of the laser intensity, before and after the laser-induced disturbance to verify that amount of energy actually deposited into the plasma. Developing

a relationship between the energy deposited into the plasma and the growth behavior of the disturbance would be of great interest to understand the variations in the fluid dynamics that were observed.

The Schlieren setup that was used in this work has mirrors far larger than are necessary to study the laser-induced disturbance in quiescent air. Smaller mirrors would provide better resolution with the same camera, as well as an improved light sensitivity. Such an application may benefit the study of these disturbances in quiescent air.

REFERENCES

[1]Stainback, P. C., Wagner, R. D., Owen, F. K., and Horstmann, C. C., “Experimental Studies of Hypersonic Boundary-Layer Transition and Effects of Wind Tunnel Disturbances." TN D-7453, March 1973, NASA.

[2]Kovasznay, L. S. G. "Turbulence in Supersonic Flow." Journal of the Aeronautical Sciences Vol. 20, No. 10, 1953, pp. 657-674.

[3]Pate, S. R. "Dominance of Radiated Aerodynamic Noise on Boundary-Layer Transition in Supersonic-Hypersonic Wind Tunnels. Theory and Application." Arnold Engineering Development Center ARNOLD AFB TN, 1978.

[4]Morkovin, M. V., "On transition experiments at moderate supersonic speeds." Journal of the Aeronautical Sciences Vol. 24, No. 7, 1957 pp. 480-486.

[5]Schneider, S. P. "Effects of high-speed tunnel noise on laminar-turbulent transition," Journal of Spacecraft and Rockets Vol. 38, No. 3, 2001, pp. 323-333.

[6]Donaldson, J., and Coulter, S. "A review of free-stream flow fluctuation and steady-state flow quality measurements in the AEDC/VKF supersonic tunnel A and hypersonic tunnel B," 6th AIAA, International Aerospace Planes and Hypersonics Technologies Conference, Chattanooga, TN. 1995.

[7]Hofferth, J., Saric, W., Kuehl, J., Perez, E., Kocian, T., and Reed, H. "Boundary-layer instability and transition on a flared cone in a Mach 6 quiet wind tunnel," International Journal of Engineering Systems Modelling and Simulation Vol. 5, No. 1-3, 2013, pp. 109-124.

[8]Juliano, T. J., Schneider, S. P., Aradag, S., and Knight, D. "Quiet-flow Ludwieg tube for hypersonic transition research." AIAA Journal Vol. 46, No. 7, 2008, pp. 1757.

[9]Schneider, S. P. "Development of hypersonic quiet tunnels," Journal of Spacecraft and Rockets Vol. 45, No. 4, 2008, pp. 641-664.

[10]Pate, S. R. "Effects of wind tunnel disturbances on boundary-layer transition with emphasis on radiated noise: A review." ARO INC ARNOLD AFS TN, 1980.

[11]Duan, L., and Choudhari, M. M., "Numerical study of pressure fluctuations due to a mach 6 turbulent boundary layer." 51st AIAA Aerospace Sciences Meeting, Grapevine, TX, January 7-10 2013.

[12]Duan, L., Choudhari, M. M., and Wu, M., "Numerical study of acoustic radiation due to a supersonic turbulent boundary layer." Journal of Fluid Mechanics Vol. 746, 2014, pp. 165-192.

[13]Parziale, N. J., Shepherd, J. E., and Hornung, H. G. "Differential Interferometric Measurement of Instability in a Hypervelocity Boundary Layer." AIAA Journal Vol. 51, No. 3, 2012, pp. 750-754.

[14]Fulghum, M. R. "Turbulence measurements in high-speed wind tunnels using focusing laser differential interferometry." The Pennsylvania State University, 2014.

[15]Parziale, N. J., Shepherd J. E., and Hornung, H. G., "Reflected shock tunnel noise measurement by focused differential interferometry." 42nd AIAA Fluid Dynamics Conference and Exhibit, New Orleans, LA, June 25-28 2012.

[16]Chou, A., "Characterization of laser-generated perturbations and instability measurements on a flared cone." Purdue University, 2010.

[17]Harris, A. J., Kreth, P. A., Combs, C. S., & Schmisseur, J. D. “Laser Differential Interferometry and Schlieren as an Approach to Characterizing Freestream Disturbance Levels.” 2018 AIAA Aerospace Sciences Meeting, Kissimmee, FL, Jan 8-12, 2018.

[18]Philips, O. M., “On the Generation of Sound by Supersonic Turbulent Shear Layers.” Journal of Fluid Mechanics, Vol. 9, No. 1, 1960, pp. 1-28.

[19]Laufer J., “Aerodynamic Noise in Supersonic Wind Tunnels,” JPL Progress Report No. 20-378, February 1959.

[20]Jet Propulsion Research Summary No. 36-6, Vol. II, January 1961.

[21]Laufer, J. "Some statistical properties of the pressure field radiated by a turbulent boundary layer," Physics of Fluids Vol. 7, No. 8, 1964, pp. 1191-1197.

[22]Pate, S. R. and Schueler, C. J., “Radiated Aerodynamic Noise Effects on Boundary-Layer Transition in Supersonic and Hypersonic Wind Tunnels,” AIAA Journal, Vol. 7, No. 3, March 1969, pp.450-457.

[23]Kistler, A., and Chen, W. "The fluctuating pressure field in a supersonic turbulent boundary layer," Journal of Fluid Mechanics Vol. 16, No. 1, 1963, pp. 41-64.

[24]Williams, J. F., and Maidanik, G. "The Mach wave field radiated by supersonic turbulent shear flows," Journal of Fluid Mechanics Vol. 21, No. 4, 1965, pp. 641-657.

[25]Bak, M. S., Wermer, L., and Im, S. K., "Schlieren imaging investigation of successive laser-induced breakdowns in atmospheric-pressure air," Journal of Physics D: Applied Physics, Vol. 48, 2015.

[26]Padhi, U. P., Singh, A. P., and Joarder, R. (2018). "Numerical Simulation of Laser-Induced Spark by Single and Double Pulse in Quiescent Air," 2018 AIAA Aerospace Sciences Meeting, Kissimmee, FL, Jan 8-12, 2018.

[27]Shneider, M., Zhang, Z., and Miles, R. "Plasma induced by Resonance Enhanced Multi-Photon Ionization (REMPI) in Inert Gas," Journal of Applied Physics, Vol. 102, 2007.

[28]Salyer, T. R., Randall, L. A., Collicott, S. H., and Schneider, S. P., "Use of laser differential interferometry to study receptivity on a hemispherical nose at Mach 4," 36th AIAA Aerospace Sciences Meeting and Exhibit, Reno, NV, 1998.

[29]Salyer, T. R., Collicott, S. H., and Schneider, S. P., "Feedback stabilized laser differential interferometry for supersonic blunt body receptivity experiments," 38th Aerospace Sciences Meeting and Exhibit, Aerospace Sciences Meeting, Reno, NV, 2000.

[30]Huang, Y., & Zhong, X., "Numerical study of laser-spot effects on boundary-layer receptivity for blunt compression-cones in Mach-6 freestream," 40th Fluid Dynamics Conference and Exhibit, Fluid Dynamics, Chicago, IL, June 28 – July 1 2010.

[31]Im, S., Wermer, L., Baccarella, D., Liu, Q., McGann, B., and Do, H., "Ramp Separation Response to Laser-Induced Breakdown Disturbed Boundary Layer at Mach 4.5," 54th AIAA Aerospace Sciences Meeting, San Diego, CA, January 4-8 2016.

[32]Schmisseur, J. D., Collicott, S. H., and Schneider, S. P., "Laser-generated localized freestream perturbations in supersonic and hypersonic flows," AIAA journal Vol. 38, No. 4, 2000. pp. 666-671.

[33]Chou, A., and Schneider, S. P., "Measurements of resonance in a forward-facing cavity at Mach six," Journal of Spacecraft and Rockets, Vol. 52, No. 5, 2015, pp 1486-1494.

[34]Hahn, D. W., and Omenetto, N., "Laser-induced breakdown spectroscopy (LIBS), part I: review of basic diagnostics and plasma–particle interactions: still-challenging issues

within the analytical plasma community," Applied spectroscopy Vol. 64, No. 12, 2010, pp. 335-366.

[35]Hahn, D. W., and Omenetto, N., "Laser-induced breakdown spectroscopy (LIBS), part II: review of instrumental and methodological approaches to material analysis and applications to different fields," Applied spectroscopy Vol. 66, No. 4, 2012, pp. 347-419.

[36]Miziolek, A. W., Vincenzo, P., and Israel S., "Laser induced breakdown spectroscopy," Cambridge University Press, 2006.

[37]Glumac, N., Elliott, G., and Boguszko, M., "Temporal and spatial evolution of a laser spark in air," AIAA journal, Vol. 43, No. 9, 2005, pp. 1984-1998.

[38]Phuoc, T. X., "Laser spark ignition: experimental determination of laser-induced breakdown thresholds of combustion gases," Optics Communications, Vol. 175, No. 4-6 2000, pp. 419-423.

[39]Kianvashrad, N., Knight, D., Wilkinson, S. P., Chou, A., Horne, R. A., Herring, G. C., Beeler, G. B., and Jangda, M., "Effect of Off-Body Laser Discharge on Drag Reduction of Hemisphere Cylinder in Supersonic Flow," 2018 AIAA Aerospace Sciences Meeting, Kissimmee, FL, Jan 8-12, 2018.

[40]Singh, B., Rajendran, L. K., Bane, S. P., and Vlachos, P. "Characterization of Fluid Motion Induced by Nanosecond Spark Plasmas: Using Particle Image Velocimetry and Background Oriented Schlieren," 2018 AIAA Aerospace Sciences Meeting, Kissimmee, FL, Jan 8-12, 2018.

[41]Yang, L., E. Erdem, H. Zare-Behtash, and K. Kontis. "Single pulse laser energy deposition in quiescent air and hypersonic flows," 18th AIAA/3AF International Space Planes and Hypersonic Systems and Technologies Conference, Tours, France, September 24-28, 2012.

[42]Ramnath, K., and Candler, G. V., "Numerical studies of laser-induced energy deposition for supersonic flow control," AIAA journal Vol. 42, No. 11, 2004, pp. 2266-2275.

[43]Settles, G. S., "Schlieren and shadowgraph techniques: visualizing phenomena in transparent media," Springer Science & Business Media, 2012.

[44]Combs, C. S., Lash, E. L., and Schmisseur, J. D., “Investigation of a Cylinder-Induced Transitional Shock Wave-Boundary Layer Interaction using Laser Diagnostics,” 32nd AIAA Aerodynamic Measurement Technology and Ground Testing Conference, 2016, Washington D.C., June 13-17, 2016

[45]Smeets, G., “Laser interferometer for high sensitivity measurements on transient phase objects,” IEEE transactions on Aerospace and Electronic Systems, Vol. 2, 1972, pp. 186-190.

[46]Smeets, G., “Flow Diagnostics by Laser Interferometry,” IEEE Transactions on Aerospace and Electronic Systems, Vol. AES-13, No. 2, 1977, pp. 82–90.

[47]Smeets, G., and George, A., “Laser-differential interferometer applications in gas dynamics," INSTITUT FRANCO-ALLEMAND DE RECHERCHES SAINT-LOUIS (FRANCE), 1996.

[48]Kocher, B. D., Combs, C. S., Kreth, P. A., and Schmisseur, J. D., “Investigation of the Effects of Ablation-Induced Roughness on Supersonic Flows,” 47th AIAA Fluid Dynamics Conference, Denver, CO, June 5-9, 2017.

[49]Ceruzzi, A., & Cadou, C. P., “Turbulent Air Jet Investigation using Focused Laser Differential Interferometry,” 53rd AIAA/SAE/ASEE Joint Propulsion Conference, Atlanta, GA, June 10-12, 2017.

[50]Pope, S. B., “Turbulent flows,” Cambridge University Press, 2000.

[51]Panchapakesan, N. R., and Lumley, J. L., “Turbulence measurements in axisymmetric jets of air and helium. Part 1. Air jet,” Journal of Fluid Mechanics, Vol. 246, 1993 pp. 197-223.

[52]Hussein, H. J., Capp, S. P., & George, W. K., (1994). “Velocity measurements in a high-Reynolds-number, momentum-conserving, axisymmetric, turbulent jet,” Journal of Fluid Mechanics, Vol. 258, 1994, pp. 31-75.

[53]Welch, P., “The use of fast Fourier transform for the estimation of power spectra: a method based on time averaging over short, modified periodograms,” IEEE Transactions on audio and electroacoustics Vol. 15, No. 2, 1967, pp. 70-73.

VITA

Adam Harris was born in Salt Lake City, Utah in 1992 to Alan and Verleen Harris. He moved to Clarksville, Tennessee in 2000, where he graduated from West Creek High School in 2011. Adam attended the University of Tennessee from 2011-2015 where he studied mechanical engineering while doing several internships and co-ops. After graduating from the University of Tennessee, Adam accepted a graduate research assistantship at the University of Tennessee Space Institute, where he studied under Dr. John D. Schmisseur until 2018. Adam has accepted a position with QuantiTech at Arnold Engineering Development Complex as a Test Analyst in the supersonic wind tunnels.